UNIVERSITÀ DEGLI STUDI DI GENOVA
SCUOLA DI SCIENZE MATEMATICHE, FISICHE E NATURALI
DIPARTIMENTO DI MATEMATICA

DOCTORAL THESIS
MATHEMATICS AND APPLICATIONS

Estimation and interpretation of the cross-power spectrum to quantify brain connectivity from electrophysiological data

---

Candidate:
Elisabetta Vallarino

Supervisors:
Prof. Alberto Sorrentino
Dr. Sara Sommariva

Year 2022

Abstract

Magneto- and electro- encephalography (MEEG) are two neuroimaging tools capable of non invasively recording the magnetic field outside the head and the scalp potential produced by the electric currents that flow inside the brain. Their strong point is the extremely high temporal resolution which makes them suitable for the study of functional connectivity, i.e. the quantification of the statistical dependencies among the time courses that describe brain activity. Functional connectivity is usually estimated from MEEG data with a two-step process: (i) first an estimate of the time courses associated with brain activity is computed by means of a regularisation method; (ii) then, source space functional connectivity is computed from the estimated time courses. The most widely used regularisation method to face this problem is Tikhonov regularisation, also known as Minimum Norm Estimate (MNE), which requires the setting of a regularisation parameter. Such a parameter will be used throughout the process and will influence the final connectivity estimate. In the core part of this thesis we will show that the regularisation parameter providing the best estimate of brain activity does not provide the best possible connectivity estimate. Indeed, a smaller parameter should be set for the latter intent. This result will be supported by both analytical and numerical proofs.

Our results highlight that the classic two-step approach plus Tikhonov regularisation presents two intrinsic drawbacks: (i) the propagation of the errors during the process, and (ii) a connectivity estimate which is over spread in space, due to Tikhonov regularisation. In this thesis we will present a one-step approach combined with the ℓ_1 regularisation, where source space functional connectivity is directly estimated from that at sensor space, without a prior estimation of source time courses. The proposed pipeline overcomes the problems of the classic approach and outperforms it, indeed, the one-step approach reduces the propagation of the errors and the ℓ_1 regularisation promotes sparsity on the connectivity estimate.

Finally, we will present *transfreq*, a Python package for the automated computation of the theta-to-alpha transition frequency. A correct estimation of such a quantity is of utmost importance for the reliability of connectivity studies in both healthy subjects and patients.

Contents

Introduction

In many real-world situations, from finance to seismology, from astrophysics to neuroscience, we are interested in quantifying the interactions between the variables and processes that characterise a specific phenomenon, as it evolves over time. It is often the case that the phenomenon of interest is not directly observable, and we can only infer information on it by indirect observations. In such contexts mathematics comes in our help, indeed, it provides powerful tools for the analysis of the phenomenon of interest. In this framework, stochastic processes and inverse problems theories are probably the ones most worth mentioning. The former allows us to model the phenomenon we are considering and offers many tools to quantify the interactions between the processes that form it. The latter is essential when dealing with indirect observation of the phenomenon, as it provides methods to estimate the variables that characterise it from its indirect observations.

Let us consider a phenomenon characterised by the simultaneous activity of N distinct and interacting processes. From a mathematical viewpoint, at any time t, the phenomenon can be modelled with a multivariate stochastic process of dimension N, $\{\mathbf{X}(t)\}_{t\in\mathbb{R}} = \{(X_1(t),\dots,X_N(t))^\top\}_{t\in\mathbb{R}}$, where $X_j(t)$, $j = 1\dots,N$, are the N distinct processes. Our aim is to quantify the interactions between all possible pairs $(X_j(t), X_k(t))$. However, the stochastic process $\{\mathbf{X}(t)\}_{t\in\mathbb{R}}$ is not directly observable, only indirect observations are available, which are modelled with a second multivariate stochastic process, $\{\mathbf{Y}(t)\}_{t\in\mathbb{R}} = \{(Y_1(t),\dots,Y_M(t))^\top\}_{t\in\mathbb{R}}$, where $Y_j(t)$, $j = 1\dots,M$, are M different observations of the phenomenon at a given time t. The observable and unobservable processes are related by a mathematical model. In this thesis we will deal with linear relationships, that is $\mathbf{Y}(t) = \mathbf{G}\mathbf{X}(t)$, where $\mathbf{G}$ is the linear model that links the two processes. In applications, the observable process is typically a measured quantity, thus we introduce a third multivariate stochastic processes, $\{\mathbf{N}(t)\}_{t\in\mathbb{R}} = \{(N_1(t),\dots,N_M(t))^\top\}_{t\in\mathbb{R}}$, which models the measurement noise. Therefore, the final equation that relates all the processes is $\mathbf{Y}(t) = \mathbf{G}\mathbf{X}(t) + \mathbf{N}(t)$. Inverse problems theory will allow us to estimate $\mathbf{X}(t)$ from $\mathbf{Y}(t)$, while stochastic processes theory will pro-

vide us with many metrics to quantify the interactions between all possible pairs $(X_j(t), X_k(t))$.

The practical application we will focus on in this thesis is that of brain connectivity. Indeed, studying and analysing the interactions among different brain regions is of utmost importance in both patients and healthy subjects (De Pasquale et al., 2010; Stam, 2010). Specifically, here we will focus on functional connectivity, which aims at quantifying the statistical dependencies among the activity in different brain areas (He et al., 2019). In the last decades many methods for estimating brain activity (Baillet et al., 2001; Pascarella and Sorrentino, 2011) and connectivity (Pereda et al., 2005; Jirsa and McIntosh, 2007; Bastos and Schoffelen, 2016; Sakkalis, 2011), have been proposed. The starting point for all these methods is the recording of brain activity. Different modalities are available: functional Magnetic Resonance Imaging (fMRI) (Huettel et al., 2004), Positron Emission Tomography (PET) (Bailey et al., 2005), Magnetoencephalography (MEG) (Hämäläinen et al., 1993) and Electroencephalography (EEG) (Niedermeyer and da Silva, 2005). In particular, this thesis will focus on Magneto- and Electroencephalography (MEEG), which record the magnetic field outside the head and the scalp potential, respectively. The two great advantages of these techniques are that (i) they are completely non invasive and (ii) they reach really high temporal resolution, of the order of milliseconds. We will see that the above mentioned linear equation, $\mathbf{Y}(t) = \mathbf{G}\mathbf{X}(t) + \mathbf{N}(t)$, properly describes the MEEG recordings as function of the underlying brain activity. Indeed, the stochastic processes $\{\mathbf{X}(t)\}_{t=0}^{T-1}$, $\{\mathbf{Y}(t)\}_{t=0}^{T-1}$, $\{\mathbf{N}(t)\}_{t=0}^{T-1}$ will model the activity of N distinct sources within the brain, the measurements of the magnetic field, or scalp potential, in correspondence of the M sensors of the instrument we are using, and the measurement noise, respectively.

Brain functional connectivity can be studied either at sensor space level, that means estimating the statistical dependencies among the time courses, $\{\mathbf{Y}(t)\}_{t=0}^{T-1}$, associated with the M sensors of the instrument we are using, or at source space level, that means estimating the statistical dependencies among the time courses that describe neural activity, $\{\mathbf{X}(t)\}_{t=0}^{T-1}$. The latter approach has the advantages of reducing the impact of volume conduction and providing results that can be more easily interpreted in the framework of neuroscientific models (Lai et al., 2018; Schoffelen and Gross, 2009; Barzegaran and Knyazeva, 2017; Van de Steen et al., 2019). Source space functional connectivity is usually estimated in a two-step process (Schoffelen and Gross, 2019b): (i) first the time courses that describe brain activity are estimated by solving the MEEG inverse problem; (ii) then functional connectivity is computed from the estimated time courses. The MEEG inverse

problem is ill-posed (Hadamard, 1902), therefore to achieve step (i) regularisation techniques are required, which rely on the choice of one or more regularisation parameters. Of course, different parameters provide different brain activity estimations and subsequently also different connectivity estimations. It would seem natural that the parameters providing the best estimate of neural activity also provide the best estimate of functional connectivity. In this thesis we will show that this is not the case.

Motivated by some empirical results (Hincapié et al., 2016), the main topic of this thesis is precisely that of investigating how to properly set the regularisation parameters when estimating functional connectivity from MEEG data with a two-step approach. Specifically, we will answer the following question: do the regularisation parameters providing the best possible estimate of neural activity also provide the best possible estimate of source space functional connectivity? Indeed, in Chapter 4 we show the analysis and results published in (Vallarino et al., 2020). Trough analytical computations, we proved that the answer to the question depends on the regularisation method used to solve the inverse problem. When using Tikhonov regularisation (Tikhonov, 1943), better known as Minimum Norm Estimate (MNE) (Hämäläinen and Ilmoniemi, 1994b) in the neuroscientific community, the parameter providing the best estimate of functional connectivity is always smaller than a half the one providing the best possible neural activity estimate. Such results are confirmed in (Vallarino et al., 2021b), as shown in Chapter 5, by numerical results obtained in a simulation framework that led us to relax some of the strong hypothesis that were needed in (Vallarino et al., 2021b); however the results are also supported by an analytical analysis of the problem. Finally, in Chapter 6, we present some preliminary and fully numerical results, obtained by simulating more complex and realistic synthetic data. This latter work is being carrying on in collaboration with professor Karim Jerbi of the University of Montreal, Canada.

The choice of focusing on the two-step approach plus Tikhonov regularisation relies on the fact that it is the most widely used pipeline for connectivity estimation, however it presents two intrinsic drawbacks: (i) the unavoidable errors that are committed during the first step inevitably propagate to connectivity estimation; (ii) Tikhonov regularisation has the great advantage of providing a closed formula to compute the solution, however it promotes smoothness on it, which is not desirable in the MEEG context as typically only few focal brain areas are active at any time. These issues may be overcome on the one hand by exploiting the ℓ_1 regularisation, which has precisely the peculiarity of promoting sparsity on the solution, on the other hand by defining a one-step approach for the estimation of brain functional

connectivity, that let us to directly estimate source space functional connectivity from that at sensor space. This will precisely be the key focus of Chapter 7, in which we will present some preliminary results obtained in collaboration with a master student of the University of Trento. Specifically, we will show the potentials of combining the two above mentioned modalities, i.e a one-step approach based on ℓ_1 regularisation, with respect to the classic two-step approach.

An optimal estimation of brain functional connectivity is of interest to understand brain functioning in both healthy subjects and patients. In recent years, many studies proved that the connectivity patterns of patients affected by neurodegenerative diseases change during the progression of the disease (Musaeus et al., 2019; Babiloni et al., 2017; Núñez et al., 2019; Duan et al., 2020). Such results can be exploited for the early diagnosis of the disease, indeed changes in connectivity patterns may appear at very early stages of the disease, years before the manifestation of the symptoms. As we will see in Chapter 3, many connectivity metrics are defined in the frequency domain. The choice of using frequency domain connectivity metrics is widely used as different frequencies are associated with different brain states. Conventionally, five frequency bands are defined, namely delta, theta, alpha, beta, gamma, ranging from low frequencies, around 1 Hz, to high frequencies, around 45 Hz. As an example the alpha band is preponderant during wakeful relaxation with closed eyes (Foster et al., 2017); in healthy subjects it comprises frequencies between 8 and 12 Hz, however in neurodegenerative patients it may manifest a shift toward left. It follows that an imprecise identification of the frequency bands may compromise the results of the connectivity studies. In particular, a delicate phase is the identification of the transition frequency from theta to alpha band, as their powers express opposite pathophysiological meaning. The standard method to compute the transition frequency is that proposed by Klimesch and colleagues in (Klimesch, 1999) and it requires two MEEG data, one acquired when the subject is resting and the other presenting a desynchronisation in the alpha band. However, this method presents two main drawbacks: (i) it needs the acquisition of two data sets; and (ii) the alpha desynchronisation must be significant enough to allow a correct identification of the transition frequency. In Chapter 8, we present the results reported in (Vallarino et al., 2021a). Specifically we present *transfreq*, a novel method for the identification of the transition frequency. The proposed method only requires one resting state data therefore it is applicable in a wider range of cases. *Tranfreq* is implemented in an open source Python package available at https://elisabettavallarino.github.io/transfreq/. The tools is easy to use therefore it can be of practical use during the analysis of MEEG recordings.

Summarising, in Chapters 1 and 2 we provide a mathematical background that

will allow a full comprehensions of the topics covered in the thesis. Specifically, we first give some basic notion on the stochastic processes theory and then on the inverse problems theory. Chapter 3 is dedicated to the description of brain functioning and provides relevant information on brain functional connectivity and the metrics for its estimation. In Chapters 4, 5 and 6 we present the results regarding the two-step estimation of brain functional connectivity. Specifically we first describe the results presented in (Vallarino et al., 2020) and (Vallarino et al., 2021b), then we will present some further preliminary results. Chapter 7 is dedicated to the one-step estimation of brain functional connectivity. Finally, in Chapter 8 the python package *transfreq* is presented, as reported in (Vallarino et al., 2021a).

Chapter 1

Mathematical background 1: Stationary stochastic processes

Stochastic processes theory has countless applications especially when dealing with time-dependent observations, which is the case of this thesis. Indeed, we will see that brain activity, sensor level recordings, and measurement noise can be interpreted as realisations of multivariate stochastic processes. Along this chapter, we will see that stochastic processes theory allows us to compute quantities such as the correlation and the covariance functions that in turn lead to the computation of the spectral density function. Spectral analysis is one of the most widely used tools for the analysis of the spectral content of a MEEG recordings. Indeed, communication between different brain areas is regulated by the synchronisation of their activity at specific temporal frequencies (Fries, 2005, 2015). For this reason, particular emphasis will be given to the estimation of the spectral density function in the case of finite, discrete an noisy realisation of a stochastic process. Indeed, in experimental context we deal with discrete realisations of stochastic processes, therefore the quantities introduced in the first part of this chapter can only be estimated. In particular, for the spectral density function estimation, two methods will be illustrated, namely the Whelch's method (Welch, 1967) and the multitapers method (Thomson, 1982). Finally, among the stochastic processes, we will highlight the multivariate autoregressive (MVAR) stochastic processes, as they are a valid and widely used tool to model brain activity (Anzolin and Astolfi, 2018; Haufe and Ewald, 2019; Liuzzi et al., 2019; Sommariva et al., 2019). Indeed, as we will see, they are easy to treat and are effective when one need to simulate interactions among different areas of the brain.

This chapter is organised as follow. In Section 1.1 some basic notion and properties will be introduced. Section 1.2 is dedicated to the spectral analysis, while

in Section 1.3 finite and discrete stochastic processes will be introduced. Finally, Section 1.4 focuses on the MVAR processes.

1.1 Basic notions and properties

Definition 1.1. Let $\mathcal{I}$ be a set and $(\mathcal{I}, \mathcal{M})$ a measurable space, a random variable on the probability space $(\Omega, \mathcal{F}, \mathbb{P})$ is a $(\mathcal{F}, \mathcal{M})$-measurable application $\mathrm{X} : \Omega \longrightarrow \mathcal{I}$.

Definition 1.2. A stochastic process, $\{X(t)\}_{t\in\mathcal{S}}$, is a time dependent family of random variables. A multivariate stochastic process of dimension N, $\{\mathbf{X}(t)\}_{t\in\mathcal{S}} = \{(X_1(t), \ldots, X_N(t))\}_{t\in\mathcal{S}}$, is a family of N stochastic processes.
Depending on $\mathcal{S}$, the process can be continuous or discrete, and infinite or finite.

In this section we will consider only continuous and infinite stochastic processes, i.e. $\mathcal{S} = \mathbb{R}$. Moreover, for simplicity, we consider real valued stochastic processes, however the theory is easily extendable to complex valued processes.

Definition 1.3. Let $\{\mathbf{X}(t)\}_{t\in\mathbb{R}}$ be a multivariate stochastic process of dimension N, at each time point, t, the mean vector is

$$\boldsymbol{\mu}(t) = \mathbb{E}[\mathbf{X}(t)] = (\mathbb{E}[X_1(t)], \ldots, \mathbb{E}[X_N(t)]) \in \mathbb{R}^N, \tag{1.1}$$

being

$$\mathbb{E}[X_j(t)] = \int_{\mathbb{R}} x\, p_{X_j(t)}(x)\, dx,$$

where $p_{X_j(t)}$ is the probability density function of $X_j(t)$.

Remark 1.4. *Note that in general $\boldsymbol{\mu}(t_1) \neq \boldsymbol{\mu}(t_2)$, with $t_1 \neq t_2$.*

1.1.1 Covariance function

Definition 1.5. Let $\{\mathbf{X}(t)\}_{t\in\mathbb{R}}$ be a multivariate stochastic process of dimension N. Given two time points, t and $t+\tau$, $t,\ \tau \in \mathbb{R}$, the covariance function returns the covariance between the variables $X_j(t)$ and $X_k(t+\tau)$, for any $j,\ k \in \{1, \ldots, N\}$, that is

$$C_{j,k}(t,\tau) = \mathbb{E}[(X_j(t) - \mu_j(t))(X_k(t) - \mu_k(t))] \tag{1.2}$$

$$= \int_{\mathbb{R}^2} (x_j - \mu_j(t))\,(x_k - \mu_k(t+\tau))\, p_{X_j(t),X_k(t+\tau)}(x_j, x_k)\, dx_j dx_k \tag{1.3}$$

being $p_{X_j(t),X_k(t+\tau)}(x_j, x_k)$ the joint probability function of $(X_j(t), X_k(t+\tau))$.

Combining all the possible pairs of processes of the multivariate process gives a family of covariance matrices

$$\mathbf{C}^{\mathbf{X}}(t, t+\tau) = \mathbb{E}[(\mathbf{X}(t) - \boldsymbol{\mu}(t))(\mathbf{X}(t+\tau) - \boldsymbol{\mu}(t+\tau))^t] \tag{1.4}$$

$$= \begin{bmatrix} C_{1,1}(t, t+\tau) & C_{1,2}(t, t+\tau) & \dots & C_{1,N}(t, t+\tau) \\ C_{2,1}(t, t+\tau) & C_{2,2}(t, t+\tau) & \dots & C_{2,N}(t, t+\tau) \\ \vdots & \vdots & \ddots & \vdots \\ C_{N,1}(t, t+\tau) & C_{N,2}(t, t+\tau) & \dots & C_{N,N}(t, t+\tau) \end{bmatrix}. \tag{1.5}$$

The definition of covariance function allows us to introduce the concepts of strongly and weakly stationary processes.

Definition 1.6. A multivariate stochastic process $\{\mathbf{X}(t)\}_{t\in\mathbb{R}}$ is said strongly stationary if for any $t_1, ..., t_n$, $\{1, \dots, n\} \subseteq \mathbb{N}$, and for any $\tau \in \mathbb{R}$ the joint probability functions of $(\mathbf{X}(t_1), ..., \mathbf{X}(t_n))$ and $(\mathbf{X}(t_1+\tau), ..., \mathbf{X}(t_n+\tau))$ are equal.

Definition 1.7. A multivariate stochastic process $\{\mathbf{X}(t)\}_{t\in\mathbb{R}}$ is said weakly stationary if

i. the second order moment of $\{\mathbf{X}(t)\}_{t\in\mathbb{R}}$ is finite for any t, that is

$$\mathbb{E}[(\mathbf{X}(t) - \boldsymbol{\mu}(t))(\mathbf{X}(t) - \boldsymbol{\mu}(t))^t] < \infty \qquad \forall\, t \in \mathbb{R};$$

ii. the mean vector does not depend on time, that is

$$\boldsymbol{\mu}(t) = \boldsymbol{\mu} \qquad \forall\, t \in \mathbb{R};$$

iii. the covariance function depends on time delay, but not on time, that is

$$\mathbf{C}^{\mathbf{X}}(t_1, t_1+\tau) = \mathbf{C}^{\mathbf{X}}(t_2, t_2+\tau) \qquad \forall\, t_1, t_2, \tau \in \mathbb{R}.$$

From iii., for ease of notation, we can drop the dependence of the covariance function on time, i.e $\mathbf{C}^{\mathbf{X}}(\tau) = \mathbf{C}^{\mathbf{X}}(t_1, t_1+\tau)$.

From now on we will be dealing with weakly stationary stochastic processes and, for ease of notation, we will refer to them simply as stationary stochastic processes.

1.1.2 Correlation function

The correlation function quantifies the linear dependency between two variables as a function of time delay. This quantity is of interest because it can be used, for instance, to detect causal relations between the variables.

Definition 1.8. Let $\{\mathbf{X}(t)\}_{t\in\mathbb{R}}$ be a stationary stochastic process, for any $j,\ k \in \{1,\dots,N\}$ the correlation function is defined by

$$R_{j,k}(\tau) = \mathbb{E}[X_j(t)X_k(t+\tau)]. \tag{1.6}$$

Specifically, if $j = k$ we refer to it as autocorrelation, otherwise as cross-correlation. Being $p_{X_j(t),X_k(t+\tau)}(x_j, x_k)$ the joint probability function of $(X_j(t), X_k(t+\tau))$, (1.6) reads

$$R_{j,k}(\tau) = \int_{\mathbb{R}^2} x_j x_k p_{X_j(t),X_k(t+\tau)}(x_j, x_k)\, dx_j dx_k. \tag{1.7}$$

The family of correlation matrices is

$$\mathbf{R}^{\mathbf{X}}(\tau) = \mathbb{E}[\mathbf{X}(t)\mathbf{X}(t+\tau)^t] \tag{1.8}$$

$$= \begin{bmatrix} R_{1,1}(\tau) & R_{1,2}(\tau) & \dots & R_{1,N}(\tau) \\ R_{2,1}(\tau) & R_{2,2}(\tau) & \dots & R_{2,N}(\tau) \\ \vdots & \vdots & \ddots & \vdots \\ R_{N,1}(\tau) & R_{N,2}(\tau) & \dots & R_{N,N}(\tau) \end{bmatrix}. \tag{1.9}$$

Observation 1.9. *Being $\boldsymbol{\mu} = (\mu_1,\dots,\mu_N)$ the mean vector of a stationary process, for any $j,\ k \in \{1,\dots,N\}$, the following hold*

i. $C_{k,j}(\tau) = R_{k,j}(\tau) - \mu_k\mu_j$,

ii. $R_{k,j}(\tau) = R_{j,k}(-\tau)$.

Note that for zero-mean stochastic processes covariance and correlation functions are equal.

1.2 Cross-spectral density function

The spectral density function can be defined via correlation function, via Fourier transform and via filtering-squaring-averaging operations. In this section the first two methods will be described. For the last method we refer the reader to (Bendat and Piersol, 2011).

1.2.1 Spectral density function via correlation

Definition 1.10. Let $\{\mathbf{X}(t)\}_{t\in\mathbb{R}}$ be a stochastic process of dimension N such that

$$\int_{\mathbb{R}} |R_{j,k}(\tau)| d\tau < +\infty \qquad \forall j,k \in \{1,\dots,N\}. \tag{1.10}$$

The cross-spectral density function is a one parameter family of $N \times N$ matrices, $\mathbf{S}(f)$ whose (j,k)-th element is defined as

$$S_{j,k}(f) = \int_{\mathbb{R}} R_{j,k}(\tau) e^{-2\pi i \tau f} d\tau. \tag{1.11}$$

Note that equation (1.11) is nothing but the Fourier transform of the correlation function.

Property 1.11. *For real valued stochastic processes, the cross–spectral density matrices are symmetric over frequency and Hermitian, that is*

$$S_{j,k}(-f) = S^*_{j,k}(f) = S_{k,j}(f), \qquad \forall j,k \in \{1,\dots,N\} \tag{1.12}$$

Proof. The first equality comes from

$$\begin{aligned} S_{j,k}(-f) &= \int_{\mathbb{R}} R_{j,k}(\tau) e^{2\pi i \tau f} d\tau \\ &= \int_{\mathbb{R}} R_{j,k}(\tau) \overline{e^{-2\pi i \tau f}} d\tau \\ &= \overline{\int_{\mathbb{R}} R_{j,k}(\tau) e^{-2\pi i \tau f} d\tau} = S^*_{j,k}(f). \end{aligned}$$

On the other hand

$$\begin{aligned} S_{j,k}(-f) &= \int_{\mathbb{R}} R_{j,k}(\tau) e^{2\pi i \tau f} d\tau \\ &= \int_{\mathbb{R}} R_{j,k}(-u) e^{-2\pi i u f} (-du) \\ &= \int_{\mathbb{R}} R_{k,j}(u) e^{-2\pi i u f} du = S_{k,j}(f), \end{aligned}$$

Where the last equality comes from Observation 1.9. □

From Property 1.12 it follows that $S_{j,j}(f)$ is a even, real valued function.

1.2.2 Spectral density function via Fourier transform

Definition 1.12. Let $\{\mathbf{X}(t)\}_{t\in\mathbb{R}}$ be a stochastic process of dimension N, the cross-spectral density function is a one parameter family of $N \times N$ matrices whose (j,k)-th element is defined as

$$S_{j,k}(f) = \lim_{T\to+\infty} S_{j,k}(f,T), \tag{1.13}$$

being

$$S_{j,k}(f,T) = \frac{1}{T}\mathbb{E}[\hat{X}_j(f)\hat{X}_k(f)^*], \tag{1.14}$$

where $\hat{X}_j(f)$ is the Fourier transform of $X_j(t)$ over the interval $[0, T]$, defined as

$$\hat{X}_j(f) = \int_0^T X_j(t) e^{-2\pi i f t} dt.$$

Proposition 1.13. *The definitions 1.10 and 1.12 are equivalent.*

Proof. Consider $S_{j,k}(f, T)$ as defined in definition 1.12. It holds

$$\begin{aligned}\frac{1}{T}\hat{X}_j(f)\hat{X}_k(f)^* &= \frac{1}{T}\int_0^T X_j(\alpha) e^{-2\pi i f \alpha}\, d\alpha \int_0^T X_k(\beta) e^{2\pi i f \beta}\, d\beta \\ &= \frac{1}{T}\int_0^T \int_0^T X_j(\alpha) X_k(\beta) e^{2\pi i f(\beta-\alpha)}\, d\alpha d\beta.\end{aligned}$$

We now implement the variable change $\tau = \beta - \alpha$ (Figure 1.1), thus we have

$$\begin{aligned}\frac{1}{T}\hat{X}_j(f)\hat{X}_k(f)^* = &\int_{-T}^0 \Big(\frac{1}{T}\int_{-\tau}^T X_j(\alpha) X_k(\alpha+\tau) d\alpha\Big) e^{-2\pi i f \tau} d\tau + \\ &+ \int_0^T \Big(\frac{1}{T}\int_0^{T-\tau} X_j(\alpha) X_k(\alpha+\tau) d\alpha\Big) e^{-2\pi i f \tau} d\tau.\end{aligned}$$

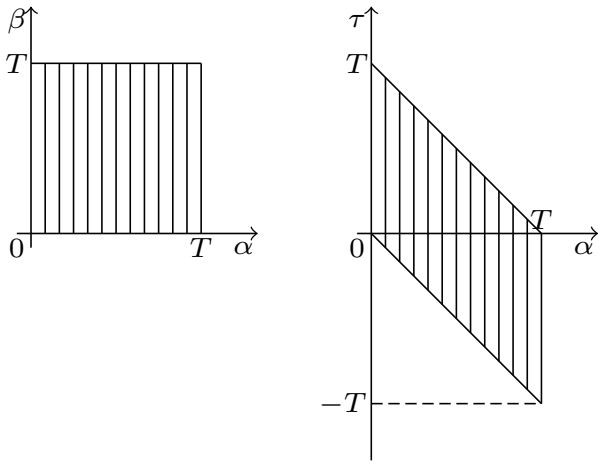

Figure 1.1: Graphical sketch of the variable change.

Applying the expectation on both sides, we get

$$\begin{aligned}
S_{j,k}(f,T) &= \int_{-T}^{0} \Big(\frac{1}{T}\int_{-\tau}^{T}\Big[\iint_{\mathbb{R}^2} x_j x_k p_{X_j(\alpha),X_k(\alpha+\tau)}(x_j,x_k)dx_j dx_k\Big]d\alpha\Big)e^{-2\pi i f\tau}d\tau + \\
&\quad + \int_{0}^{T} \Big(\frac{1}{T}\int_{0}^{T-\tau}\Big[\iint_{\mathbb{R}^2} x_j x_k p_{X_j(\alpha),X_k(\alpha+\tau)}(x_j,x_k)dx_j dx_k\Big]d\alpha\Big)e^{-2\pi i f\tau}d\tau \\
&= \int_{-T}^{0} \Big(\frac{1}{T}\int_{-\tau}^{T} R_{j,k}(\tau)d\alpha\Big)e^{-2\pi i f\tau}d\tau + \int_{0}^{T}\Big(\frac{1}{T}\int_{0}^{T-\tau} R_{j,k}(\tau)d\alpha\Big)e^{-2\pi i f\tau}d\tau \\
&= \int_{-T}^{0} \frac{T+\tau}{T} R_{j,k}(\tau)e^{-2\pi i f\tau}d\tau + \int_{0}^{T}\frac{T-\tau}{T} R_{j,k}(\tau)e^{-2\pi i f\tau}d\tau \\
&= \int_{-T}^{T} \frac{T-|\tau|}{T} R_{j,k}(\tau)e^{-2\pi i f\tau}d\tau.
\end{aligned}$$

Finally, applying the limit for $T \to \infty$, we get, by dominated convergence,

$$\begin{aligned}
\lim_{T\to\infty} \mathbb{E}[S_{j,k}(f,T)] &= \lim_{T\to\infty}\int_{-T}^{T}\frac{T-|\tau|}{T}R_{j,k}(\tau)e^{-2\pi i f\tau}d\tau \\
&= \int_{-\infty}^{+\infty} R_{j,k}(\tau)e^{-2\pi i f\tau}d\tau.
\end{aligned}$$

□

1.3 Finite and discrete realisations of stochastic processes

So far we have been dealing with infinite and continuous stochastic processes, however in experimental contexts we mainly deal with finite and discrete measures of a specific event. Such measures can be interpreted either as samples over time of a continuous and infinite stochastic process or as a realisation of a finite and discrete stochastic process. For convenience we stick to the first interpretation. We indicate the set of sample measures by $\{\mathbf{x}(t)\}_{t=0}^{T-1}$, where the lower case is used to indicate that we are dealing with a specific realisation of a random variable and $t = 0, \ldots, T-1$ are the time points in which the process has been sampled. In this case we cannot apply the above definitions of mean, correlation and cross-spectral density, on the contrary we only are able to estimate them from the data. In this section we will see how to do it.

Definition 1.14. Let $\{\mathbf{x}(t)\}_{t=0}^{T-1}$ be the realisation of a stationary stochastic process of dimension N.

i. The sample mean vector is defined as

$$\bar{\boldsymbol{\mu}} = (\bar{\mu}_1, ..., \bar{\mu}_N)^t, \tag{1.15}$$

where

$$\bar{\mu}_j = \frac{1}{T}\sum_{t=0}^{T-1} x_j(t).$$

ii. the sample covariance is defined as

$$\bar{C}_{j,k}(\tau) = \frac{1}{T-2-\tau}\sum_{t=0}^{T-1-\tau}(x_j(t)-\bar{\mu}_j)(x_k(t+\tau)-\bar{\mu}_k). \tag{1.16}$$

iii. the sample correlation is defined as

$$\bar{R}_{j,k}(\tau) = \frac{1}{T-1-\tau}\sum_{t=0}^{T-1-\tau} x_j(t)x_k(t+\tau). \tag{1.17}$$

Note that the assumption of stationarity is crucial, indeed the above quantities can be reliably estimated because they do not change over time.

As for the cross-spectral density function, its estimation is more challenging. Many methods have been proposed in literature and they are divided in two main categories, the non parametric methods and the parametric ones. In the following, two non parametric methods will be described, for an exhaustive description of all the methods we refer the reader to (Stoica et al., 2005).

1.3.1 Welch's method

The first method to be described is the Whelch's method (Welch, 1967), which was introduced for the first time in 1967 as a modification of the Bartlett method (Bartlett, 1950) with the aim of diminishing the variance of the estimate. For the ease of notation let us first consider a realisation of a univariate stochastic process, $\{x(t)\}_{t=0}^{T-1}$, and then we will extend the method to the multivariate case. The Welch's method is schematised as follow:

1. $\{x(t)\}_{t=0}^{T-1}$ is divided into P overlapping segments of length L

$$\begin{aligned}
&x^1(t) = X(t) && t = 0, ..., L-1\\
&x^2(t) = X(t+D) && t = 0, ..., L-1\\
&\vdots\\
&x^M(t) = x(t+(M-1)D) && t = 0, ..., L-1,
\end{aligned}$$

being D the overlap length and $(P-1)D + L = T$;

2. each segment is then multiplied by a window function, $w(t)$, to obtain the sequence $\{x^{(p)}(t)w(t)\}_{p=0}^{P}$, $t = 0, \ldots, T-1$;

3. then the discrete Fourier transform of each term of the sequence is computed

$$\hat{x}^{(p)}(n) = \sum_{t=0}^{L-1} x^{(p)}(t)w(t)e^{\frac{-2\pi i}{L}tn}, \qquad n = 0, ..., L-1; \tag{1.18}$$

4. subsequently, the modified periodogram, $I^{(p)}$, are computed

$$I^{(p)}(f_n) = \frac{1}{W}|\hat{X}^{(p)}(n)|^2, \qquad p = 1, ..., P, \tag{1.19}$$

being

$$W = \sum_{t=0}^{L-1} w(t)^2$$

and

$$f_n = \frac{n}{L}, \qquad n = 0, ..., \frac{L}{2};$$

5. finally, the estimate of the power spectrum is given by

$$\tilde{S}^X(f_n) = \frac{1}{P}\sum_{p=1}^{P} I^{(p)}(f_n). \tag{1.20}$$

In case of a realisation of a multivariate stochastic process, step 1. to 3. are applied to each component then the one parameter family of modified periodogram matrices is computed, being its (j,k)-th element

$$I_{k,j}^{m}(f_n) = \frac{1}{W}\,\hat{x}_k^m(n)\hat{x}_j^m(n)^*, \qquad m = 1, ..., M. \tag{1.21}$$

Finally, the (j,k)-th element of the estimate of the one parameter family of cross-spectral density matrices is

$$\tilde{S}_{k,j}(f_n) = \frac{1}{P}\sum_{p=1}^{P} I_{k,j}^{(p)}(f_n). \tag{1.22}$$

With respect to Bartlett's method, Welch's method introduces the overlap between consecutive segments, such choice increases the number of periodograms to be averaged, and thus it reduces the variance of the estimate. The use of a window function, $w(t)$, is also a novelty and it is introduced to mitigate the spectral leakage (Jwo et al., 2021). Many different types of window function can be defined; Figure

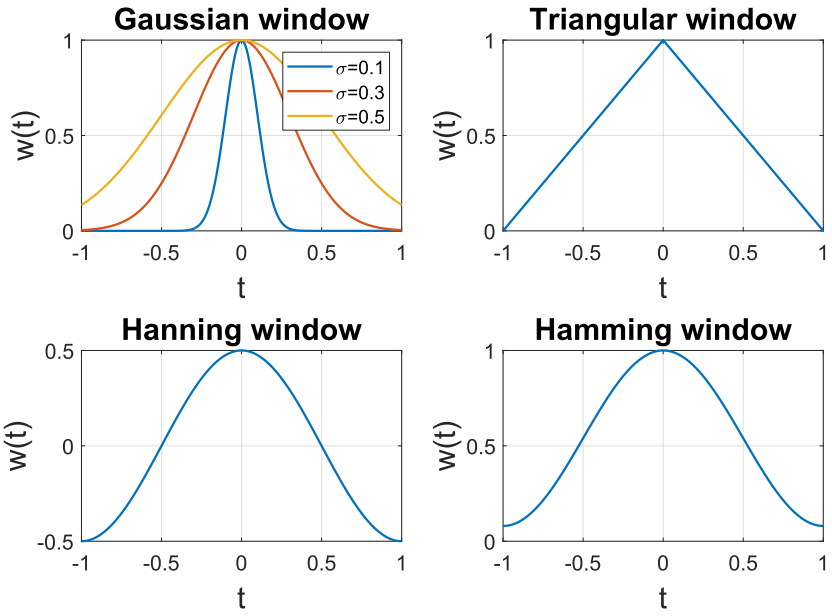

Figure 1.2: Representation of the window functions. The three types of Gaussian functions differ for the value of the standard deviation, σ.

1.2 shows some of the most common ones.

1.3.2 Multitapers method

The multitapers method (Thomson, 1982) was introduced for the first time in 1982 by Thomson. Like Whelch's method, multitapers method involves a windowing process of the data, however it has the advantages that the windows are not arbitrary and the frequency resolution is higher. The major difference from Welch's method is that the data is not divided into segments and then multiplied by a single window function, but rather the whole data is multiplied by a set of window functions (tapers), the discrete prolate shperoidal sequnces, or Slepian sequences, in honour of their inventor.
Let $\{\mathbf{x}(t)\}_{t=0}^{T-1}$ be the observations of a multivariate stationary stochastic process of dimension N, the multitapers method can be schematised as follow (Thomson, 2007):

1. first, a time-bandwidth product $C_0 = TW$ is set;

2. then, the tapers, $w^{(p)}(t)$, are computed. For a specific choice of C_0 there are $P = \lfloor 2C_0 \rfloor$ tapers;

3. subsequently, the Fourier transform of the windowed data is computed

$$\hat{\mathbf{x}}^{(p)}(n) = \frac{1}{T} d^{(p)}(n) \sum_{t=0}^{T-1} w^{(p)}(t)\mathbf{x}(t) e^{\frac{-2\pi i}{T} tn}, \tag{1.23}$$

   where $d^{(p)}(n)$ are proper weights;

4. then, the cross-spectrum of each individual taper is computed, being its (j,k)-th element

$$\tilde{S}_{j,k}^{(p)}(n) = \hat{x}_j^{(p)}(n)\hat{x}_k^{(p)}(n)^*; \tag{1.24}$$

5. finally, the multitaper estimate of the cross-power spectrum is the one parameter family of matrices whose (j,k)-th element is

$$\tilde{S}_{j,k}(n) = \frac{1}{P} \sum_{p=1}^{P} \tilde{S}_{j,k}^{(p)}(n). \tag{1.25}$$

For details on how to compute the tapers, set the weights and define C_0 see (Thomson, 1982).

1.4 MVAR processes

Multivariate autoregressive (MVAR) processes are a particular type of stochastic processes. Their linearity makes it easy to deal with them and therefore they are widely used to model real world (North, 2003). In this section a brief introduction to the MVAR precesses will be given as they will be used in Chapter 5 to model brain activity. For further details see (Lütkepohl, 2005).

Definition 1.15. An MVAR process of order P is a discrete multivariate stochastic process $\{\mathbf{X}(t)\}_{t\in\mathbb{Z}}$ if

$$\mathbf{X}(t) = \boldsymbol{\nu} + \sum_{p=1}^{P} \mathbf{A}(p)\mathbf{X}(t-p) + \boldsymbol{\varepsilon}(t) \qquad \forall t, \tag{1.26}$$

where $\mathbf{A}(p)$ are fixed coefficient matrices, and $\boldsymbol{\epsilon}(t) \in \mathbb{R}^N$ is a white Gaussian noise process with covariance matrix Σ. Moreover, the MVAR model described by equation (1.26) is said to be stable if

$$\det\left(\mathbf{I}_N - \sum_{p=1}^{P} \mathbf{A}(p) z^p\right) \neq 0 \qquad \forall\, z \in \mathbb{C}\ s.t.\ |z| \leq 1, \tag{1.27}$$

where $\mathbf{I}_N$ is the identity matrix of size N.

Remark 1.16. *From equation (1.26) it can be easily seen that the process $\mathbf{X}(t)$ is uniquely determined by the process $\boldsymbol{\varepsilon}(t)$ and by the first P time points, $\mathbf{X}(0)$, ..., $\mathbf{X}(P-1)$. Indeed, consider for example an MVAR model of order 1 (a similar proof holds for the general case $P > 1$ and can be found in (Lütkepohl, 2005)); then for each time point t*

$$\begin{aligned}\mathbf{X}(t) &= \mathbf{A}(1)\mathbf{X}(t-1) + \boldsymbol{\varepsilon}(t) \\ &= \mathbf{A}(1)^2\mathbf{X}(t-2) + \mathbf{A}(1)\boldsymbol{\varepsilon}(t-1) + \boldsymbol{\varepsilon}(t) \\ &= \mathbf{A}(1)^t\mathbf{X}(0) + \sum_{k=0}^{t-1} \mathbf{A}(1)^k\boldsymbol{\varepsilon}(t-k)\ .\end{aligned}$$

Such a model satisfies the stability condition defined in equation (1.27) if all the eigenvalues of the coefficient matrix $\mathbf{A}(1)$ have modulus less then one, condition that guarantees the sequence of exponential matrices $\left\{\mathbf{A}(1)^k\right\}_k$ to be absolutely summable.

The coefficient matrices define uniquely the cross-spectral density of the process. Indeed, the following proposition holds, where for simplicity we consider a zero-mean MVAR process (i.e $\boldsymbol{\mu} = 0$)

Proposition 1.17. *Let $\{\mathbf{X}(t)\}_{t\in\mathbb{Z}}$ be a zero-mean MVAR process of order P, then the one parameter family of cross-power spectral matrices is*

$$\mathbf{S}(f) = \mathbf{H}(f)\Sigma\mathbf{H}(f)^*, \tag{1.28}$$

where $\mathbf{H}$ is transfer function defined as

$$\mathbf{H}(f) = (I_N - \mathbf{A}(f))^{-1}, \tag{1.29}$$

being $\mathbf{A}(f)$ the Fourier transform of the coefficient matrices

$$\mathbf{A}(f) = \sum_{t=1}^{p} \mathbf{A}(t)e^{-2\pi i f t}. \tag{1.30}$$

According to equation (1.26), if a process $\mathbf{X}(t)$ follows an MVAR model, then at each time point the value of $\mathbf{X}(t)$ can be derived as a weighted sum of the values of the process at the previous P time points, $\mathbf{X}(t-1)$, ..., $\mathbf{X}(t-P)$, plus a random perturbation $\boldsymbol{\varepsilon}(t)$. In particular, the (i,j)-th elements of the coefficient matrices, $a_{ij}(1)$, ..., $a_{ij}(P)$, describe how the value of the i-th component of the process depends on the past of the j-th component. The next chapter is dedicated to an overview of brain functional connectivity, however we anticipate that when dealing with MVAR processes different connectivity patterns, with various levels

of complexity, can be obtained by tuning the off-diagonal values of the coefficient matrices. Due to their flexibility and simplicity, MVAR models have been used by various authors in the framework of MEEG functional connectivity estimation as a benchmark for testing and comparing different connectivity metrics (Anzolin et al., 2019; Chella et al., 2019; Haufe et al., 2013; Haufe and Ewald, 2019; Liuzzi et al., 2019; Sommariva et al., 2019; Nolte et al., 2008). Other models have been proposed to simulate different connectivity patterns, such as coherent sinusoidal time series (Hincapié et al., 2016), neural mass models (Wendling et al., 2002; Astolfi et al., 2007) or Kuramoto models (Acebrón et al., 2005; Cabral et al., 2014). However a comprehensive comparison of all possible generative models is beyond the scope of this thesis.

Chapter 2

Mathematical background 2: Inverse problems theory

In this chapter some notions about the inverse problems theory will be given. This branch of mathematics arises from the need to identify and quantify events that cannot be directly measured and whose information is only available through indirect measurements. This is the case of MEEG which measures the magnetic field outside the head and the scalp potentials produced by the neural currents that flow inside the brain and that characterise brain activity. Once the mathematical model that links the event of interest with its indirect observations is defined, by solving the so called inverse problem associated with such a model, we obtain an estimate of the event. If the inverse problem is well-posed, solving it is straightforward, however in experimental contexts, it is often the case that the inverse problem is ill-posed. Thus, estimating the event of interest might be challenging thus specific techniques are required. Regularisation methods are widely used to solve inverse problems, and they seek for a solution that, at the same time, fits well the data and have some desired properties such as smoothness or sparsity.

This chapter is organised as follow. In Section 2.1 inverse problems will be defined. Then, in Section 2.2 the concept of generalised inverse will be defined. Finally, Section 2.3 is dedicated to the regularisation methods.

2.1 Definition

Let $\mathbf{T} : X \to Y$ be a linear continuous operator between the Hilbert spaces X and Y, with bounded range, $R(\mathbf{T})$. Let us consider the following equation

$$\mathbf{Tx} = \mathbf{y}, \tag{2.1}$$

being $\mathbf{x} \in X$ and $\mathbf{y} \in Y$. Solving the inverse problem associated with equation (2.1) means estimating $\mathbf{x}$ given the data $\mathbf{y}$ and the operator $\mathbf{T}$. If $\mathbf{T}$ is invertible the problem is easily solvable, however in many applications it is not. In our case, for instance, we will see that $\mathbf{T}$ is not squared and thus is not invertible, however this is just one of the reasons why the problem is not easily solvable. Indeed, in many real world problems we deal with ill-posed problems.

Definition 2.1. A problem of the form (2.1) is said to be well-posed in the sense of Hadamard (Hadamard, 1902) if the solution

i. exists,

ii. is unique,

iii. changes continuously with the initial conditions.

If one of the above conditions is not satisfied the problem is said to be ill-posed.

Observation 2.2. *1. i. is equivalent to the surjectivity of* $\mathbf{T}$*;*

2. *ii. is equivalent to the injectivity of* $\mathbf{T}$*;*

3. *iii. means that to small variations of the data correspond small variations of the solution;*

4. *if* $\mathbf{T}$ *is invertible conditions i. and ii. are guaranteed.*

2.2 Generalised inverse

Let us consider an ill-posed inverse problem of the form (2.1). Even though the conditions of well-posedness are not fulfilled we might be interested in finding a proper solution. This means, for instance, that if condition i. of Definition 2.1 is not satisfied we might seek for a solution that "almost" satisfies equation (2.1); or, if condition ii. is not satisfied, we might add additional requirements to find a unique solution. These translate in the concept of generalised solution (Engl et al., 1996).

Definition 2.3. Let $\mathbf{T} : X \to Y$ be a linear continuous operator between the Hilbert spaces X and Y with closed range, $R(\mathbf{T})$. The generalised solution of problem (2.1) is equivalently defined as:

a.

$$\mathbf{x}^\dagger \in S \text{ s.t } \|\mathbf{x}^\dagger\| \leq \|\mathbf{u}\| \; \forall \mathbf{u} \in S,$$

being

$$S = \{\mathbf{u} \in S \text{ s.t. } \|\mathbf{Tu} - \mathbf{y}\| \leq \|\mathbf{Tx} - \mathbf{y}\| \; \forall \mathbf{x} \in S\}.$$

b.

$$\mathbf{x}^\dagger = \mathbf{T}^\dagger \mathbf{y},$$

where $\mathbf{T}^\dagger$ is defined as follow. Consider an invertible linear continuous operator $\tilde{T} : X \to Y$, such that $\tilde{\mathbf{T}}_{|N(\mathbf{T})^\perp} = \mathbf{T}_{|N(\mathbf{T})^\perp}$, being $N(\cdot)$ the kernel, and $\cdot^\perp$ the orthogonal space, then $\tilde{\mathbf{T}}$ is defined as

$$\mathbf{T}^\dagger = P_{N(\mathbf{T})^\dagger} \tilde{\mathbf{T}}^{-1} : X \to Y,$$

being $P_{N(\mathbf{T})^\dagger}$ the orthogonal projection on $N(\mathbf{T})^\dagger$.

Observation 2.4. *By $\|\cdot\|$ it is meant $\|\cdot\|_X$ or $\|\cdot\|_Y$ being the argument an element of X or Y respectively, and they are the norms induced by the inner product defined in the Hilbert spaces X and Y.*

Theorem 2.5. *Le $\mathbf{T} : X \longrightarrow X$ be a linear continuous operator between the Hilbert spaces X and Y, and let $\mathbf{u} \in X$. The following are equivalent.*

i. $\mathbf{Tu} = P_{R(\mathbf{T})}\mathbf{y}$*;*

ii. $\|\mathbf{Tu} - \mathbf{y}\| \leq \|\mathbf{Tx} - \mathbf{y}\| \; \forall \mathbf{x} \in X$*;*

iii. $\mathbf{T}^*\mathbf{Tu} = \mathbf{Ty}$*, being $\mathbf{T}^*$ the adjoint operator.*

2.3 Regularisation methods

Let $\mathbf{T} : X \to Y$ be a linear continuous operator between the Hilbert spaces X and Y with non-closed range, $R(\mathbf{T})$. In this case $\mathbf{T}^\dagger$ does not lead to a good solution. Indeed, being $R(\mathbf{T})$ non-closed, $\mathbf{T}^\dagger$ is not bounded, thus there is no continuous dependence on the data. To overcome such a problem we introduce the regularisation methods which aim at approximating an ill-posed problem with a family of neighbouring well-posed problems.

Definition 2.6. Let $\mathbf{T} : X \to Y$ be a linear continuous operator between the Hilbert spaces X and Y. The family of operators $\{\mathbf{R}_\lambda\}_{\lambda>0}$, $\mathbf{R}_\lambda : Y \to X$, is said a regularisation algorithm if:

i. $\mathbf{R}_\lambda$ is linear, continuous, and bounded;

ii. $\lim_{\lambda\to 0} \mathbf{R}_\lambda \mathbf{y} = \mathbf{T}^\dagger \mathbf{y} \qquad \forall \mathbf{y} \in R(\mathbf{T}) \oplus R(\mathbf{T})^\perp$

The parameter λ is said regularisation parameter.

Let us now consider the problem

$$\mathbf{T}^*\mathbf{T}\mathbf{x} = \mathbf{T}^*\mathbf{y}, \tag{2.2}$$

which is equivalent to problem (2.1).

Definition 2.7. Let $\mathbf{T} : X \to Y$ be an operator. The spectrum of $\mathbf{T}$ is defined as

$$\sigma(\mathbf{T}) = \{\omega \in \mathbb{C} \text{ s.t. } \omega\mathbf{I} - \mathbf{T} \text{ is not invertible}\},$$

being $\mathbf{I}$ is the identity operator.

Observation 2.8. *If $X = \mathbb{R}^N$, $N \in \mathbb{N}$, then $\sigma(\mathbf{T}) = \{\omega \in \mathbb{C}$ s.t. ω is an eigenvalue of $\mathbf{T}\}$*

Definition 2.9. Let $\tilde{\mathbf{R}}_\lambda : \sigma(\mathbf{T}^*\mathbf{T}) \subseteq [0, \|\mathbf{T}\|^2] \subseteq \mathbb{R}$ be a continuous operator such that it is an approximation of the function $f(t) = t^{-1}$, $t \in (0, +\infty)$, for $\lambda \to 0$, then

$$\mathbf{x}^\dagger = \tilde{\mathbf{R}}_\lambda(\mathbf{T}^*\mathbf{T})\mathbf{T}^*\mathbf{y} \tag{2.3}$$

is said regularised solution.

Theorem 2.10. *Let $\mathbf{T} : X \to Y$ be a linear continuous operator between the Hilbert spaces X and Y and consider problem* (2.1)*. Let $\{\tilde{\mathbf{R}}_\lambda\}_{\lambda>0}$, $\tilde{\mathbf{R}}_\lambda : (0, \|\mathbf{T}\|^2] \to \mathbb{R}$, a family of real value functions. If*

i. $\tilde{\mathbf{R}}_\lambda \xrightarrow[\lambda\to 0]{} t^{-1}\ \forall t \in (0, \|\mathbf{T}\|^2]$,

ii. $t\tilde{\mathbf{R}}_\lambda(t)$ *is uniformly bounded,*

then the regularised solution converges to the generalised solution, that is

$$\mathbf{x}_\lambda = \tilde{\mathbf{R}}_\lambda(\mathbf{T}^*\mathbf{T})\mathbf{T}^*\mathbf{y} \xrightarrow[\lambda\to 0]{} \mathbf{x}^\dagger = \mathbf{T}^\dagger\mathbf{y},$$

with $\mathbf{y} \in R(\mathbf{T}^\dagger) \oplus R(\mathbf{T}^\dagger)^\perp$.

Regularisation methods provide a good approximation of the generalised solution in case of noisy free data. However they are crucial also in the presence of noise.

Suppose our data is affected by noise with intensity δ, that is

$$\|\mathbf{y} - \mathbf{y}^\delta\| \leq \delta, \tag{2.4}$$

where $\mathbf{y}$ is the noise free data. Thus the problem reads

$$\mathbf{y}^\delta = \mathbf{T}\mathbf{x} + \mathbf{n}^\delta. \tag{2.5}$$

In the case of a linear regularisation algorithm it holds

$$\|\mathbf{R}_\lambda \mathbf{y}^\delta - \mathbf{x}^\dagger\| \leq \|\mathbf{R}_\lambda \mathbf{T}\mathbf{x}^\dagger - \mathbf{x}^\dagger\| + \delta\|\mathbf{R}_\lambda\|. \tag{2.6}$$

The first term on the right hand side is the approximation error due to the use of $\mathbf{R}_\lambda$ instead of the generalised inverse and it tends to zero when λ tends to zero. The second term on the right hand side quantifies the error on the regularised solution, $\mathbf{R}_\lambda \mathbf{y}^\delta$, due to the presence of noise and it tends to infinity when λ tends to zero. This implies that for any δ it exists an optimal value of the regularisation parameter $\lambda_{opt}(\delta)$ such that the right hand side of equation (2.6) is a minimum. We can now define the following.

Definition 2.11. A regularisation algorithm $\{\mathbf{R}_\lambda\}_{\lambda>0}$ is said regular if, for $\delta \to 0$

$$\lambda_{opt}(\delta) \to 0 \quad \text{and} \quad \mathbf{R}_{\lambda_{opt}} \mathbf{y}^\delta \to \mathbf{x}^\dagger$$

In the next session we will introduce some regularisation algorithms that are of interest for the present work.

2.3.1 Truncated Singular Value Decomposition

Definition 2.12. Let $\mathbf{T} : X \to Y$ be a linear continuous compact operator between the Hilbert spaces X and Y. Then $\mathbf{T}^*\mathbf{T}$ is compact, self-adjoint and positive definite. Let $\{\sigma_n^2\}_{n=1}^\infty$ be the eigenvalues of $\mathbf{T}^*\mathbf{T}$ (that are the same of $\mathbf{T}\mathbf{T}^*$),which are positive and accumulate to zero and let $\{\mathbf{u}_n\}_{n=1}^\infty$ be the corresponding eigenfunctions. Then, the vectors

$$\mathbf{v}_n = \frac{1}{\sigma}\mathbf{T}\mathbf{u}_n \quad \in Y \tag{2.7}$$

are the eigenfunctions of $\mathbf{T}\mathbf{T}^*$. The set of triplets $\{\sigma_n, \mathbf{u}_n, \mathbf{v}_n\}_{n=1}^\infty$ is the singular system of $\mathbf{T}$ and the following hold:

$$\mathbf{T}\mathbf{v}_n = \sigma_n \mathbf{u}_n \tag{2.8}$$

$$\mathbf{T}^*\mathbf{u}_n = \sigma_n \mathbf{v}_n \tag{2.9}$$

$$\mathbf{T}\mathbf{x} = \sum_{n=1}^{\infty} \sigma_n(\mathbf{x}, \mathbf{v}_n)\mathbf{u}_n, \qquad \mathbf{x} \in X \tag{2.10}$$

$$\mathbf{T}^*\mathbf{y} = \sum_{n=1}^{\infty} \sigma_i(\mathbf{y}, \mathbf{u}_n)\mathbf{v}_n, \qquad \mathbf{y} \in Y. \tag{2.11}$$

Equations (2.10) and (2.11) are called Singular Value Decomposition (SVD) of $\mathbf{T}$ (Engl et al., 1996).

If $X = \mathbb{R}^N$ and $Y = \mathbb{R}^M$ and $\mathbf{T} \in \mathbb{R}^{M\times N}$ is a matrix, being $\mathbf{U} = (\mathbf{u}_1^\top, \ldots, \mathbf{u}_M^\top) \in \mathbb{R}^{M\times M}$, $\mathbf{\Sigma} = \text{diag}(\sigma_1, \ldots, \sigma_M) \in \mathbb{R}^{M\times N}$ and $\mathbf{V} = (\mathbf{v}_1^\top, \ldots, \mathbf{v}_N^\top) \in \mathbb{R}^{N\times N}$ the SVD of $\mathbf{T}$ can be expressed in compact form as

$$\mathbf{T} = \mathbf{U}\mathbf{\Sigma}\mathbf{V}^\top, \tag{2.12}$$

being $\cdot^\top$ the transpose operator.

Theorem 2.13. *The one-parameter family* $\{\mathbf{R}_\lambda\}_{\lambda\in\mathbb{N}^*}$ *defined by*

$$\mathbf{R}_\lambda \mathbf{y} = \sum_{n=1}^{\lambda} \frac{1}{\sigma_i}(\mathbf{y}, \mathbf{v}_i)\mathbf{u}_i \tag{2.13}$$

is a regular regularisation algorithm.

Definition 2.14. From Theorem 2.13 the truncated SVD (tSVD) solution of problem (2.5) reads

$$\mathbf{x}_\lambda = \sum_{n=1}^{\lambda} \frac{1}{\sigma_i}(\mathbf{y}^\delta, \mathbf{v}_i)\mathbf{u}_i \tag{2.14}$$

Observation 2.15. *In the matrix case the tSVD solution reads*

$$\mathbf{x}_\lambda = \sum_{i=1}^{\lambda} \frac{1}{\sigma_i}(\mathbf{u}_i^\top \mathbf{y}^\delta)\mathbf{v}_i, \tag{2.15}$$

and can also be expressed in terms of the so called filter factors (Hansen, 2005) as

$$\mathbf{x}_\lambda = \mathbf{W}_\lambda \mathbf{y}^\delta = \mathbf{V}\mathbf{\Phi}(\lambda)\mathbf{\Sigma}^\dagger \mathbf{U}^\top \mathbf{y}^\delta \tag{2.16a}$$

$$= \sum_{i=1}^{M} \varphi_i(\lambda) \frac{\mathbf{u}_i^\top \mathbf{y}^\delta}{\sigma_i}\mathbf{v}_i \quad \lambda \in \{1, \ldots, M\} \quad , \tag{2.16b}$$

where $\mathbf{\Sigma}^\dagger$ *is the pseudo-inverse of* $\mathbf{\Sigma}$*, and the filter factors,* $\mathbf{\Phi}(\lambda) = (\varphi_1(\lambda), \ldots, \varphi_M(\lambda))$*, read*

$$\varphi_i(\lambda) = \begin{cases} 1 & \textit{if} \quad i \leq \lambda \\ 0 & \textit{if} \quad i > \lambda \end{cases} \quad . \tag{2.17}$$

Clearly, the choice of the parameter λ is crucial. Many methods have been proposed to set such a parameter; we will not enter into the details, however let us say that the key point in the choice of λ is to keep all the components associated with the higher singular values (Hansen, 2005).

2.3.2 Tikhonov regularisation

Tikhonov regularisation method was introduced by Tikhonov in 1943 (Tikhonov, 1943). Tikhonov method introduces two constraints on the solution of the ill-posed problem (2.1):

$$\text{i.} \quad \|\mathbf{Tx} - \mathbf{y}\| \leq \varepsilon \tag{2.18}$$

$$\text{ii.} \quad \|\mathbf{x}\| \leq E \tag{2.19}$$

$\|\mathbf{Tx} - \mathbf{y}\|$ is the norm of residual (or fidelity term). Condition i. imposes small entropy, ε, for such a quantity, which means that we seek for a solution that fits well the data and is a good approximation of the generalised solution. $\|\mathbf{x}\|$ is the penalty term. Condition ii. imposes small energy, E, to this term, which means that we seek for a regular solution, which is a characteristic associated with noise free data.

Definition 2.16. Let $\mathbf{T} : X \to Y$ be a linear continuous operator between the Hilbert spaces X and Y and λ be a positive, real value, the Tikhonov regularised solution is the minimum of the functional

$$\begin{aligned} \Phi_\lambda : X &\longrightarrow \mathbb{R} \\ \mathbf{x} &\longmapsto \Phi_\lambda := \|\mathbf{Tx} - \mathbf{y}\|^2 + \lambda\|\mathbf{x}\|^2. \end{aligned} \tag{2.20}$$

Thus the solution reads

$$\mathbf{x}_\lambda = \arg\min_\lambda \left\{ \|\mathbf{Tx} - \mathbf{y}\|^2 + \lambda\|\mathbf{x}\|^2 \right\}. \tag{2.21}$$

The regularisation parameter λ trades off the weight given to the fidelity and penalty terms. Such a parameter has to be set a-priori; many methods have been proposed to set such a parameter, each one with its pros and cons (Engl et al., 1996).

Let us now get back to conditions (2.18) and (2.19). A schematic representation is depicted in Figure 2.1. Two cases can be described. In the first case, among all the solutions that satisfy condition (2.18) we seek for the one with minimum energy, that is $\|\mathbf{x}\| = E_{min}$. As shown in Figure 2.1(a) such a solution lies on boundary of $\|\mathbf{Tx} - \mathbf{y}\| \leq \varepsilon$, therefore the smaller ε is, the higher $\|\mathbf{x}\|$ is. In the second case, among all the solution that satisfy condition (2.19) we seek for the one with smallest discrepancy, that is $\|\mathbf{Tx} - \mathbf{y}\| = \epsilon_{min}$. As shown in Figure 2.1(b) such a solution lies on the boundary of $\|\mathbf{x}\| = E$, therefore the smaller E is, the higher $\|\mathbf{Tx} - \mathbf{y}\|$ is. It is clear that the two conditions cannot be satisfied at the same time for any value of ε and E.

Definition 2.17. We call compatibility region the set of solutions that satisfy both

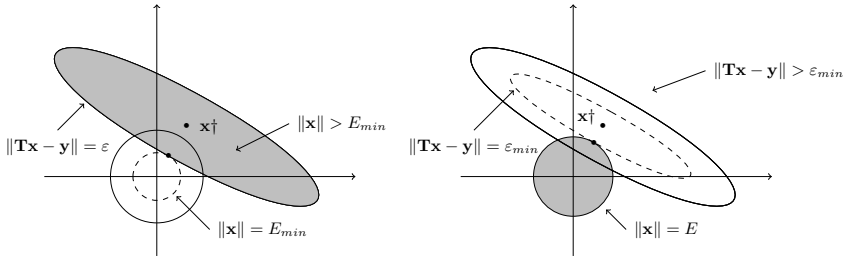

(a) (b)

Figure 2.1: Schematic representation of the constraints (2.18) and (2.19). (a) Among all the solutions that satisfy condition (2.18) the one with minimum energy lies on the boundary of $\|\mathbf{Tx}-\mathbf{y}\| \leq \varepsilon$. (b) Among all the solution that satisfy condition (2.19) the one with minimum discrepancy lies on the boundary of $\|\mathbf{x}\| = E$.

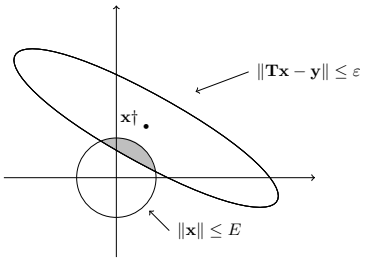

Figure 2.2: Schematic representation of the compatibility region.

conditions (2.18) and (2.19)

$$\{\mathbf{x} \in X : \|\mathbf{x}\| \leq E \text{ and } \|\mathbf{Tx}-\mathbf{y}\| \leq \varepsilon\}.$$

Figure 2.2 shows a graphic interpretation of the compatibility region.

Theorem 2.18. *For any $\mathbf{y} \in Y$ and $\lambda > 0$ the Tikhonov functional $\Phi_\lambda(x)$, has a unique minimum point $\mathbf{x}_\lambda \in \mathrm{N}(\mathbf{T})^\perp$. Such a point is the solution of the Euler equation*

$$(\mathbf{T}^*\mathbf{T} + \lambda\mathbf{I})\mathbf{x}_\lambda = \mathbf{T}^*\mathbf{y}, \tag{2.22}$$

being $\mathbf{I}$ the identity operator. In particular

$$\mathbf{x}_\lambda = (\mathbf{T}^*\mathbf{T} + \lambda\mathbf{I})^{-1}\mathbf{T}^*\mathbf{y}. \tag{2.23}$$

Theorem 2.19. *The one-parameter family $\{\mathbf{R}_\lambda\}_{\lambda>0}$ defined by*

$$\mathbf{R}_\lambda = (\mathbf{T}^*\mathbf{T} + \lambda\mathbf{I})^{-1}\mathbf{T}^* \tag{2.24}$$

is a regular regularisation algorithm.

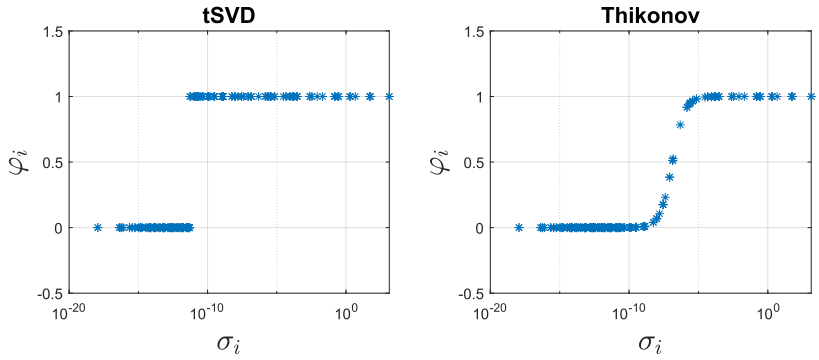

Figure 2.3: Filter factors of tSVD (left) and Tikhonov (right) regularisation methods. In this example $\mathbf{T} \in \mathbb{R}^{200\times 200}$, $\lambda_{tSVD} = 100$, $\lambda_{Tikh} = \sigma_{max}^2 \cdot 10^{-10}$.

Proposition 2.20. *Let $\{\mathbf{x}_\lambda\}_{\lambda>0}$ be the family of Tikhonov regularised solutions, $\forall \mathbf{y} \in Y$. Then*

i. $\varepsilon(\lambda) = \|\mathbf{x}_\lambda\|$ *is weakly increasing and assumes values in* $(\|\mathbf{y}^\perp\|, \|\mathbf{y}\|)$*, being* $\mathbf{y}^\perp = (I - P_{\overline{R(\mathbf{T})}})\mathbf{y}$*,*

ii. $E(\lambda) = \|\mathbf{T}\mathbf{x}_\lambda - \mathbf{y}\|$ *is weakly decreasing and assumes values in* $(0, \|T^\dagger \mathbf{y}\|)$ *if* $\mathbf{y} \in R(\mathbf{T}^\dagger) \oplus R(\mathbf{T}^\dagger)^\perp$*, or in* $(0, +\infty)$ *if* $\mathbf{y} \notin R(\mathbf{T}^\dagger) \oplus R(\mathbf{T}^\dagger)^\perp$*.*

Similarly to the tSVD case, also the Tikhonov regularised solution can be expressed by equations (2.16a) and (2.16b) in terms of the filter factors. In this case the filter factors read

$$\varphi_i(\lambda) = \frac{\sigma_i^2}{\sigma_i^2 + \lambda}. \tag{2.25}$$

Observation 2.21. *The filter factors assume values in* $(0, 1)$*. The role of* λ *is to suppress the component associated with the smallest eigenvalues. Indeed, for the highest eigenvalues* λ *is negligible with respect to* σ_i^2 *therefore the corresponding filter factor* $\varphi_i(\lambda)$ *is close to* 1*, whereas on the opposite situation, i.e. for the smallest eigenvalue, the corresponding filter factor is close to zero. Similarly to what happen in the tSVD case,* λ *is set to keep the components associated with the higher eigenvalues, however, while with tSVD the filters factor only assume values 0 or 1, with Tikhonov regularisation they increase smoothly in within the interval* $(0, 1)$*. A visual representation of such a behaviour in the matrix case is depicted in Figure 2.3.*

2.3.3 ℓ_1 regularisation

Another widely used regularisation method is the ℓ_1 regularisation method. Differently from Tikhonov method which seeks for a solution with a small ℓ_2-

norm, that is a smooth solution, ℓ_1 regularisation promotes sparsity on the solution. Sparsity is obtained by substituting the ℓ_2-norm in the penalty term in (2.20) with the ℓ_1-norm. In order to use the ℓ_1-norm we suppose X to be a Banach space (Schuster et al., 2012). The ℓ_1 regularised solution is defined as follow.

Definition 2.22. Let $\mathbf{T} : X \to Y$ be a linear continuous operator between the Banach space X and the Hilbert space Y and λ be a positive Let λ be a positive real value, the ℓ_1 regularised solution is the minimum of the functional

$$\begin{aligned} \Phi_\lambda : \mathbb{R}^N &\longrightarrow \mathbb{R} \\ \mathbf{x} &\longmapsto \Phi_\lambda \coloneqq \|\mathbf{T}\mathbf{x} - \mathbf{y}\|_2^2 + \lambda \|\mathbf{x}\|_1, \end{aligned} \tag{2.26}$$

where we stress that $\|\cdot\|_2$ is the ℓ_2-norm in the Hilbert space Y, and $\|\cdot\|_1$ is the ℓ_1-norm in the Banach space X. Thus

$$\mathbf{x}_\lambda = \arg\min_\lambda \left\{ \|\mathbf{T}\mathbf{x} - \mathbf{y}\|_2^2 + \lambda \|\mathbf{x}\|_1 \right\}. \tag{2.27}$$

In this case, an explicit computation of the solution is not possible and iterative methods have to be used. Such methods are typically defined for the discretised version of problem (2.1), which is always the case in experimental contexts, where $X = \mathbb{R}^N$, $Y = \mathbb{R}^M$, and $\mathbf{T} \in \mathbb{R}^{M \times N}$. Here we will focus on the Fast Iterative Shrinkage-Thresholding Algorithm (FISTA) (Beck and Teboulle, 2009), which is an improved version of the Shrinkage-Thresholding Algorithm (ISTA) (Daubechies et al., 2004). The next section is precisely dedicated to the definition of FISTA, however to get to the definition we first need to describe the Proximal Gradient Method (Combettes and Pesquet, 2011), together with its fast version, and ISTA.

As a further remark before introducing FISTA, we stress that, as mentioned above, ℓ_1 regularisation promotes sparsity on the solution, whereas Tikhonov regularisation promotes smoothness. The difference between the two methods is illustrated in Figure 2.4 in a bi-dimensional case. In the ℓ_1 case, among all the solutions with a given ℓ_1-norm, the one with smallest entropy lies on the corner of $\|\mathbf{x}\|_1 = E$, that is a solution with null x_1 component. Depending on the properties that are desirable for the solution one may choose to use Tikhonov regularisation or ℓ_1 regularisation, however there are some intrinsic properties that are worth mentioning as they may influence the choice. Tikhonov regularisation has the great advantage of having a closed form solution, easy to compute, however for its computation the matrix $\mathbf{T}\mathbf{T}^* + \lambda \mathbf{I}_M$ needs to be inverted. Such operation might not be computationally feasible for high dimensional problems. This difficulty can be overcome with the ℓ_1 regularisation method, however using an iterative method

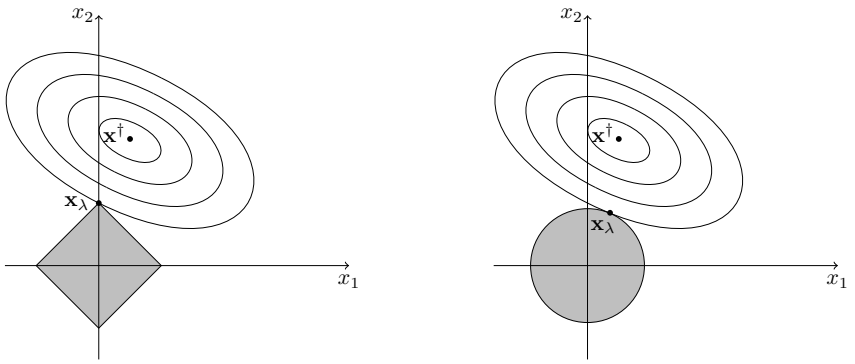

Figure 2.4: Schematic representation of the difference between ℓ_1 (a) and Tikhonov (b) regularisation methods. While ℓ_1 promotes sparsity, Tikhonov promotes smoothness.

can be time consuming and needs to set parameters such as the tolerance and the maximum number of iteration which add subjectivity to the method.

Fast Iterative Shrinkage-Thresholding Algorithm (FISTA)

Let us first introduce a general general version of problem (2.26), i.e.

$$\begin{aligned} \Phi : \mathbb{R}^N &\longrightarrow \mathbb{R} \\ \mathbf{x} &\longmapsto \Phi \coloneqq f(x) + g(x), \end{aligned} \tag{2.28}$$

with $g : \mathbb{R}^N \to \mathbb{R}$ a non-smooth continuous convex function and $f : \mathbb{R}^N \to \mathbb{R}$ a continuously differentiable convex function. Problem (2.26) is a particular case of the latter one, when $f(\mathbf{x}) = \|\mathbf{T}\mathbf{x} - \mathbf{y}\|_2^2$ and $g(\mathbf{x}) = \lambda\|\mathbf{x}\|_1$. The optimisation model we are now considering reads

$$\arg\min_{\mathbf{x}}\{\Phi(\mathbf{x})\}. \tag{2.29}$$

Being Φ non-smooth the gradient algorithm cannot be applied to (2.29), however we recall how it works as it will be useful to explain the next contents. Let us consider the continuously differentiable convex function f, to which we can apply the gradient method to find its minimum

$$\arg\min_{\mathbf{x}}\{f(\mathbf{x})\}. \tag{2.30}$$

The gradient method (Lemaréchal, 2012) generates a sequence $\{\mathbf{x}_k\}$, where, ah each iteration, $\mathbf{x}_k$ moves into the direction of the steepest descend. Given a suitable

starting point $\mathbf{x}_0$ and stepsize $t_k > 0$, a generic point of the sequence is given by

$$\mathbf{x}_k = \mathbf{x}_{k-1} - t_k \nabla f(\mathbf{x}_{k-1}). \tag{2.31}$$

Let us now consider a quadratic approximation of f, that is

$$q_t(\mathbf{x}, \mathbf{w}) \coloneqq f(\mathbf{w}) + \langle \mathbf{x} - \mathbf{w}, \nabla f(\mathbf{w}) \rangle + \frac{1}{2t} \|\mathbf{x} - \mathbf{w}\|^2. \tag{2.32}$$

The first two terms of (2.32) are the linearised form of f at a given point $\mathbf{w}$, while the third term quantifies the error in approximating $f(\mathbf{w})$ with the quadratic form. Now, by observing that it holds

$$\|\mathbf{x} - \mathbf{w}\|^2 = \|\mathbf{x} - \mathbf{w} + t\nabla f(\mathbf{w})\|^2 - t^2 \|\nabla f(\mathbf{w})\|^2 - 2t\langle \mathbf{x} - \mathbf{w}, \nabla f(\mathbf{w}) \rangle, \tag{2.33}$$

the quadratic form reads

$$q_t(\mathbf{x}, \mathbf{w}) = f(\mathbf{w}) + \frac{1}{2t} \|\mathbf{x} - \mathbf{w} + t\nabla f(\mathbf{w})\|^2 - \frac{t}{2} \|\nabla f(\mathbf{w})\|^2 . \tag{2.34}$$

It is well known (Polyak, 1987) that the gradient iteration (2.31) can be equivalently written as

$$\mathbf{x}_k = \arg\min_{\mathbf{x}} \{q_{t_k}(\mathbf{x}, \mathbf{x}_{k-1})\} \tag{2.35}$$

$$= \arg\min_{\mathbf{x}} \left\{ f(\mathbf{x}_{k-1}) + \frac{1}{2t_k} \|\mathbf{x} - \mathbf{x}_{k-1} + t\nabla f(\mathbf{x}_{k-1})\|^2 - \frac{t_k}{2} \|\nabla f(\mathbf{x}_{k-1})\|^2 \right\}, \tag{2.36}$$

which becomes

$$\mathbf{x}_k = \arg\min_{\mathbf{x}} \left\{ \frac{1}{2t_k} \|\mathbf{x} - (\mathbf{x}_{k-1} - t\nabla f(\mathbf{x}_{k-1}))\|^2 \right\}, \tag{2.37}$$

after ignoring the constant terms.

Let us now get back to problem (2.29). By applying the same iterative idea of (2.37) to (2.29) we get the following iterative scheme

$$\mathbf{x}_k = \arg\min_{\mathbf{x}} \left\{ \frac{1}{2t_k} \|\mathbf{x} - (\mathbf{x}_{k-1} - t\nabla f(\mathbf{x}_{k-1}))\|^2 + g(\mathbf{x}) \right\}. \tag{2.38}$$

This scheme can be rewritten in terms of the proximal operator, which is defined as follow.

Definition 2.23. For any $t > 0$ and for any convex function $g : \mathbb{R}^N \to \mathbb{R}$ the

proximal operator associated with g is defined as

$$\text{prox}_t^g(\mathbf{w}) \coloneqq \arg\min_{\mathbf{x}} \left\{ g(\mathbf{x}) + \frac{1}{2t}\|\mathbf{x}-\mathbf{w}\|^2 \right\}, \tag{2.39}$$

with $\mathbf{x},\ \mathbf{w} \in \mathbb{R}^N$

By exploiting the proximal operator equation (2.38) reads

$$\mathbf{x}_k = \text{prox}_{t_k}^g(\mathbf{x}_{k-1} - t_k \nabla f(\mathbf{x}_{k-1})). \tag{2.40}$$

Let us now further assume thet f is a continuously differentiable convex function with Lipschitz continuous gradient with constant $L > 0$, i.e. for any $\mathbf{x}$, $\mathbf{w}$ $\in \mathbb{R}^N$ it holds

$$\|\nabla f(\mathbf{x}) - \nabla f(\mathbf{w})\| \leq L \|\mathbf{x}-\mathbf{w}\|. \tag{2.41}$$

The Lipschitz constant, L, can be used to define the stepsize, t_k. This is the case of the Proximal Gradient Method with constant stepsize rule. Such a method is defined by the following steps

Input: L, a Lipschitz constant of ∇f

Step 0. Take $\mathbf{x}_0 \in \mathbb{R}^N$, and set $t_k = \frac{1}{L}$;

Step k. (with $k \geq 1$) compute

$$\mathbf{x}_k = \text{prox}_{\frac{1}{L}}^g \left(\mathbf{x}_{k-1} - \frac{1}{L}\nabla f(\mathbf{x}_{k-1}) \right). \tag{2.42}$$

The convergence rate of the function values $\Phi(\mathbf{x}_k)$ is provided by the following theorem.

Theorem 2.24. *Let $\Phi : \mathbb{R}^N \to \mathbb{R}$ be defined as $\Phi(\mathbf{x}) = f(\mathbf{x}) + g(\mathbf{x})$, with $g : \mathbb{R}^N \to \mathbb{R}$ a continuous convex function and $g : \mathbb{R}^N \to \mathbb{R}$ a continuously differentiable convex function with Lipschitz continuous gradient with constant $L > 0$. For any $k \geq 1$ and for any minimiser $\mathbf{x}_* \in \mathbb{R}^N$ of $\Phi(\mathbf{x})$ it holds*

$$\Phi(\mathbf{x}_k) - \Phi(\mathbf{x}_*) \leq \frac{L\|\mathbf{x}_0 - \mathbf{x}_*\|^2}{2k}, \tag{2.43}$$

being $\mathbf{x}_k$ defined by equation (2.42) *and $\mathbf{x}_0 \in \mathbb{R}^N$ a suitable starting point.*

From this theorem we can state that the order of convergence of the Proximal Gradient Method is $O(\frac{1}{k})$. Such a convergence rate is improved by its fast version, i.e. the Fast Proximal Gradient Method. The Fast Proximal Gradient Method maintains the same structure of the Proximal Gradient Method, however it introduces an

auxiliary point, $\mathbf{w}_k$, at which the proximal operator is computed and that is defined by a linear combination of $\mathbf{x}_{k-1}$ and $\mathbf{x}_{k-2}$. The new algorithm is defined by the following steps.

Input: L, a Lipschitz constant of ∇f

Step 0. Take $\mathbf{x}_0 \in \mathbb{R}^N$, and set $\mathbf{w}_1 = \mathbf{x}_0$ and $t_1 = 1$

Step k.(with $k \geq 1$) Compute

$$\mathbf{x}_k = \text{prox}^g_{\frac{1}{L}}\left(\mathbf{w}_k - \frac{1}{L}\nabla f(\mathbf{w}_k)\right); \tag{2.44}$$

$$t_{k+1} = \frac{1}{2} + \frac{1}{2}\sqrt{1 + 4t_k^2}; \tag{2.45}$$

$$\mathbf{w}_{k+1} = \mathbf{x}_k + \frac{t_k - 1}{t_{k+1}}(\mathbf{x}_k - \mathbf{x}_{k-1}) \tag{2.46}$$

In this case the order of the convergence rate is $O(\frac{1}{k^2})$, indeed, the following theorem holds.

Theorem 2.25. *Let $\Phi : \mathbb{R}^N \to \mathbb{R}$ be defined as $\Phi(\mathbf{x}) = f(\mathbf{x}) + g(\mathbf{x})$, with $g : \mathbb{R}^N \to \mathbb{R}$ a continuous convex function and $g : \mathbb{R}^N \to \mathbb{R}$ a continuously differentiable convex function with Lipschitz continuous gradient with constant $L > 0$. For any $k \geq 1$ and for any minimiser $\mathbf{x}_* \in \mathbb{R}^N$ of $\Phi(\mathbf{x})$ it holds*

$$\Phi(\mathbf{x}_k) - \Phi(\mathbf{x}_*) \leq \frac{L\|\mathbf{x}_0 - \mathbf{x}_*\|^2}{(k+1)^2}, \tag{2.47}$$

being $\mathbf{x}_k$ defined by equation (2.44) *and $\mathbf{x}_0 \in \mathbb{R}^N$ a suitable starting point.*

Let us now get back to problem (2.26), which can be seen as a particular case of problem (2.28), being $f(\mathbf{x}) = \|\mathbf{T}\mathbf{x} - \mathbf{y}\|_2^2$ and $g(\mathbf{x}) = \lambda\|\mathbf{x}\|_1$. In this case, $f(\mathbf{x})$ is a continuously differentiable convex function with gradient

$$\nabla f(\mathbf{x}) = 2\mathbf{T}^\top(\mathbf{T}\mathbf{x} - \mathbf{y}), \tag{2.48}$$

and it is Lipschitz continuous with smallest constant $L = 2\sigma_{max}(\mathbf{T}^\top\mathbf{T})$, where $\sigma_{max}(\mathbf{T}^\top\mathbf{T})$ is the maximum eigenvalue of $\mathbf{T}^\top\mathbf{T}$; while $g(\mathbf{x})$ is a continuous convex non-smooth function. The proximal operator associatoed to g can be analitically computed and it coincides with the the shrinkage operator.

Definition 2.26. Given $\alpha > 0$, the shrinkage operator is defined as

$$\mathcal{T}_\alpha(\mathbf{x})_i = (|x_i| - \alpha)_+ \text{sgn}(x_i) \tag{2.49}$$

$$= \begin{cases} x_i - \alpha & \text{if } x_i \geq \alpha \\ x_i + \alpha & \text{if } x_i \leq -\alpha \\ 0 & \text{otherwise} \end{cases}. \tag{2.50}$$

Theorem 2.27. *Given $g : \mathbb{R}^N \to \mathbb{R}$ defined as $g(\mathbf{x}) \coloneqq \lambda\|\mathbf{x}\|_1$, with $\lambda > 0$, the proximal operator associated with g with $t > 0$ coincides with the shrinkage operator of threshold $\alpha = \lambda t$, i.e.*

$$prox_t^g(\mathbf{x}) = \mathcal{T}_{\lambda t}(\mathbf{x}). \tag{2.51}$$

We can now define ISTA as the Proximal Gradient Method applied to problem (2.26) by using the shrinkage operator and the Lipschitz constant $L = \sigma_{max}(\mathbf{T}^\top\mathbf{T})$. ISTA iterative scheme results in:

Input: $L = \sigma_{max}(\mathbf{T}^\top\mathbf{T})$

Step 0. Take $\mathbf{x}_0 \in \mathbb{R}^N$

Step k. (with $k \geq 1$) compute

$$\mathbf{x}_k = \mathcal{T}_{\frac{\lambda}{L}}\left(\mathbf{x}_{k-1} - \frac{2}{L}\mathbf{T}^\top(\mathbf{T}\mathbf{x}_{k-1} - \mathbf{y})\right). \tag{2.52}$$

Similarly, we can define FISTA as the Fast Proximal Gradient method applied to problem (2.26) by using the shrinkage operator and the Lipschitz constant $L = \sigma_{max}(\mathbf{T}^\top\mathbf{T})$. FISTA iterative scheme results in:

Input: $L = \sigma_{max}(\mathbf{T}^\top\mathbf{T})$

Step 0. Take $\mathbf{x}_0 \in \mathbb{R}^N$, and set $\mathbf{w}_1 = \mathbf{x}_0$ and $t_1 = 1$

Step k. (with $k \geq 1$) Compute

$$\mathbf{x}_k = \mathcal{T}_{\frac{\lambda}{L}}\left(\mathbf{w}_k - \frac{2}{L}\mathbf{T}^\top(\mathbf{T}\mathbf{x}_{k-1} - \mathbf{y})\right); \tag{2.53}$$

$$t_{k+1} = \frac{1}{2} + \frac{1}{2}\sqrt{1 + 4t_k^2}; \tag{2.54}$$

$$\mathbf{w}_{k+1} = \mathbf{x}_k + \frac{t_k - 1}{t_{k+1}}(\mathbf{x}_k - \mathbf{x}_{k-1}) \tag{2.55}$$

Chapter 3

Brain functional connectivity from MEEG data

While the study of the brain as a set of specialised units capable of specific functions remains of utmost importance, in the last decades the study of brain connectivity has gained more and more attention (Horwitz, 2003). Indeed, understanding how different brain regions communicate and cooperate may reveal important information about brain functioning in both healthy subjects and patients (De Pasquale et al., 2010; Stam, 2010). The underlying principles are that of segregation and integration of information, which refer to the presence of highly specialised and interconnected regions in the brain that are able to communicate between each other. The exchange of information between different brain regions relies on the electrical currents that flows along the axons of the neurons. Such an exchange of information is extremely rapid, therefore disposing of devices capable of capturing the rapid and tiny changes of the electrical currents is crucial. In this sense, magneto- and electro-encephalograpy (MEEG) are giving a great contribute. Indeed, they record, on a millisecond scale, the magnetic field outside the head and the scalp potential, respectively, produced by the neural currents that flow inside the brain. The general term connectivity refers to different concepts, however in this chapter we will focus on functional connectivity, which refers to the statistical dependencies between different brain areas. To this end many statistical metrics can be defined, which quantify the interactions between the time series of interest. Such metrics can be directly applied to the time series associated with each of the MEEG sensors or can be applied to the time series that model the activity at source space level. The latter approach has the advantages of providing more accurate and interpretable results, however, it requires solving the MEEG inverse problem in order to estimate the neural activity. From a mathematical viewpoint, the manipulation of Maxwell's equations leads us to a linear equation that links the

neural currents that flow inside the brain to the magnetic field and the scalp potential recorded by the MEEG sensors. Solving the MEEG inverse problem means estimating the time series that generated the MEEG recordings. Such a problem is ill-posed as the solution is not unique and there is no continuous dependence on the data, thus a technique needs to be identified to reach a satisfying estimate. Afterwards, from the estimated neural activity, functional connectivity can be estimated by using the desired connectivity metric.

This chapter is organised as follow. In Section 3.1 some basic notions of brain functioning will be given. Sections 3.2 and 3.3 are dedicated to the MEEG forward and inverse problems, respectively, while in Section 3.4 some details about the MEEG devices will be given. Finally, in Section 3.5, the concept of brain connectivity will be introduced, together with some common connectivity metrics and the standard pipeline for their estimation.

3.1 Basic aspects of brain functioning

The nervous system is a complex structure that allows the control of functions that enable humans to regulate their internal environment and to react to, or have interactions with, the external environment. The nervous system is divided into two main parts: the central nervous system, consisting of the spinal cord and the encephalon, and the peripheral nervous system, consisting of the sensory and motor pathways. The structure of interest for MEEG is the encephalon, which is the organ completely contained in the skull. In adults the encephalon weighs approximately 1 400 grams and is essential for controlling and managing both the physiological activities of the body and processes such as conscious activity, interactions with the outside world, memory, thinking and emotions.

The encephalon is divided into brain, brainstem and cerebellum. The brain in turn consists of diencephalon and telencephalon, the first being positioned in the core of the brain, the second being external. The telencephalon constitutes 80% of the volume of the entire central nervous system and is divided into two cerebral hemispheres (right and left). The hemispheres are connected through the corpus callosum, which ensure communication and cooperation between the two helves. The hemispheres are enveloped by the cerebral cortex, a thin layer of grey matter characterised by countless folds and intended for information processing.

The cortex of each of the two hemispheres is divided into four lobes (frontal, parietal, occipital, temporal), see Figure 3.1 for their position. Each of these is responsible for a particular function. As an example, Figure 3.2 shows the motor and somatosensory cortices, which are located in the precentral gyrus (the final part

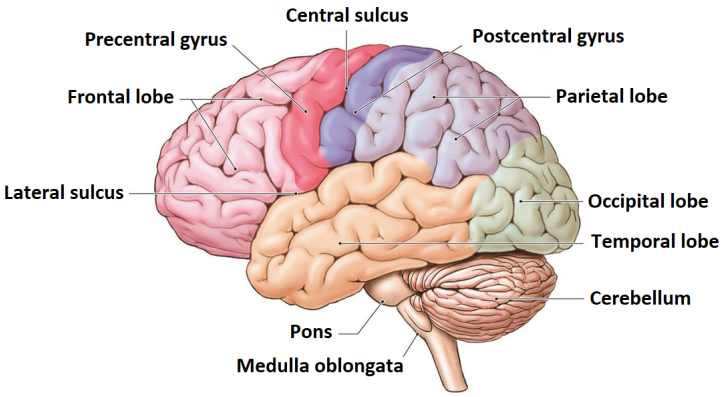

Figure 3.1: Lobes of the brain (Bear et al., 2020). The external part of the brain, i.e. the cortex, is divided into four lobes (frontal, parietal, occipital, temporal). A ridge is termed gyrus and a groove is termed sulcus. The lobes are further divided into smaller areas based on their cellular composition and function, sensory and motor areas are two examples.

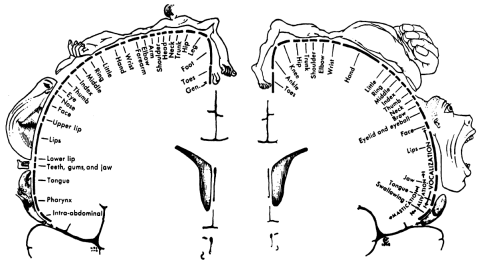

Figure 3.2: Visual representation of the somatosensory and motor cortices and their functionalities (Schott, 1993). The first is related to the impulses related to touch, while the second is related to the control of voluntary movements.

of the frontal lobe) and the postcentral gyrus (the initial part of the parietal lobe) respectively. The motor cortex is involved in the planning, control, and execution of voluntary body movements, while the somatosensory cortex is responsible for receiving stimuli related to taste, touch, pain and temperature.

The fundamental units of the nervous system are the neurons, cells that transmit nerve impulses. They consist of: a cell body, which contains the nucleus and most of the metabolic devices of the cell; dendrites, short, filamentous cytoplasmic extensions that, together with the cell body, receive stimuli from other cells; and an axon, a long extension capable of rapidly conducting an electrochemical signal (Figure 3.3). Neurons are specialised in receiving signals from the internal and external environment and transmitting the received information to other neurons or structures in the body (Curtis et al., 1981).

Nerve conduction, i.e. the transmission of information between neurons, is associated with electrical phenomena. In fact, there is a difference in electrical po-

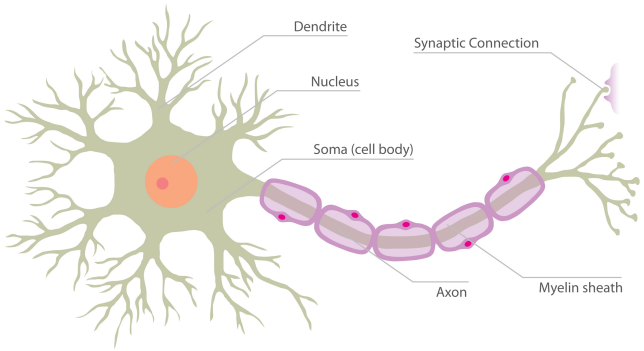

Figure 3.3: The neuron and its components (Fountas et al., 2011). The neuron is the cellular unit that forms brain tissue. It has the role of receiving, elaborating and transmitting nervous impulses: the dendrites receive the impulses from other cells, the nucleus elaborates the stimulus and sends the response along the axons towards the axons terminals, which transmit it to other cells.

tential between the outside and inside of the axon, with the inside of the membrane positively charged with respect to the outside. If the axon is stimulated there is a very brief reversal of polarity. This reversal of polarity is called nerve impulse and is precisely associated with the exchange of information between neurons. The electric currents that flow along the axons are the focus of MEEG, indeed it is well know that electric currents generate an electric and a magnetic field, and such fields are the target of MEEG studies, as we will see in the next sections.

3.2 The MEEG forward problem

The MEEG forward problem aims at computing the magnetic field outside the head and the scalp potential given the electric currents that flow inside the brain. The starting point for the computation of these two quantities is the quasi-static approximation of Maxwell's equations, under the assumption that the magnetic permeability of brain tissue is that of the vacuum, i.e.

$$\nabla \cdot \mathbf{E}(\mathbf{r}, t) = \frac{\rho(\mathbf{r},t)}{\varepsilon_0}, \tag{3.1}$$

$$\nabla \times \mathbf{E}(\mathbf{r}, t) = 0 \tag{3.2}$$

$$\nabla \cdot \mathbf{B}(\mathbf{r}, t) = 0 \tag{3.3}$$

$$\nabla \times \mathbf{B}(\mathbf{r}, t) = \mu_0 \mathbf{J}(\mathbf{r}, t); \tag{3.4}$$

where $\mathbf{E}(\mathbf{r}, t)$ and $\mathbf{J}(\mathbf{r}, t)$ are the electric field and electric current, respectively, at location $\mathbf{r}$ and time t, ρ is the charge density, μ_0 is the vacuum magnetic permeability and ε_0 is the vacuum electric permittivity (Malmivuo et al., 1995).
From equation (3.2) we note that, under the quasi-static approximation, the electric

field is irrotational and thus, according to the Poincarè Lemma, it can be expressed in terms of the electric scalar potential V, i.e.

$$\mathbf{E}(\mathbf{r},t) = -\nabla V(\mathbf{r},t). \tag{3.5}$$

The electric current generated by brain activity is the sum of two contributions, the primary current, $\mathbf{J}^p$, which is directly related to brain activity, and the volume current, $\mathbf{J}^v$, which is due to the non-null conductivity of the brain, i.e. $\mathbf{J}^v(\mathbf{r},t) = \sigma(\mathbf{r})\mathbf{E}(\mathbf{r},t)$. Thus, the total current reads as

$$\mathbf{J}(\mathbf{r},t) = \mathbf{J}^p(\mathbf{r},t) + \sigma(\mathbf{r})\mathbf{E}(\mathbf{r},t) \tag{3.6}$$

$$= \mathbf{J}^p(\mathbf{r},t) - \sigma(\mathbf{r})\nabla V(\mathbf{r},t). \tag{3.7}$$

Now, computing the divergence of equation (3.4) and recalling that the divergence of a curl is zero, we obtain

$$0 = \nabla \cdot \mathbf{J}(\mathbf{r},t) = \nabla \cdot \mathbf{J}^p(\mathbf{r},t) - \nabla \cdot (\sigma(\mathbf{r})\nabla V(\mathbf{r},t)) \tag{3.8}$$

In parallel, from equations (3.3) and (3.4) it follows the Biot-Savart equation (Hämäläinen et al., 1993)

$$\mathbf{B}(\mathbf{r},t) = \frac{\mu_0}{4\pi}\int_\Omega \frac{\mathbf{J}(\mathbf{r}',t)\times\mathbf{R}}{R^3}\mathrm{d}\mathbf{r}', \tag{3.9}$$

which, by exploiting (3.7), turns into

$$\mathbf{B}(\mathbf{r},t) = \frac{\mu_0}{4\pi}\int_\Omega \frac{(\mathbf{J}^p(\mathbf{r}',t) - \sigma(\mathbf{r}')\nabla' V(\mathbf{r}',t))\times\mathbf{R}}{R^3}\mathrm{d}\mathbf{r}', \tag{3.10}$$

where Ω is the head volume, $\mathbf{R} = \mathbf{r} - \mathbf{r}'$ and $R = |\mathbf{R}|$.

We now have all the ingredients to solve the MEEG forward problems: assuming that we know $\mathbf{J}^p(\mathbf{r},t)$, first, we obtain V by solving equation (3.8) and then we compute $\mathbf{B}$ and $\mathbf{E}$ by solving equations (3.10) and (3.5).

This problem is typically faced assuming that the head is a piecewise homogeneous conductor, i.e. it is made of isotropic contiguous regions $\{\Omega_i\}_{i=1,\dots,J}$ of conductivity $\{\sigma_i\}_{i=1,\dots,J}$, e.g. scalp, skull, cerebrospinal fluid, grey matter and white region. Under this assumption it can be shown (Hämäläinen et al., 1993) that

$$\mathbf{B}(\mathbf{r},t) = \mathbf{B}_0(\mathbf{r},t) + \frac{\mu_0}{4\pi}\sum_{i,j}(\sigma_i - \sigma_j)\int_{\partial\Omega_{i,j}} V(\mathbf{r}',t)\frac{\mathbf{R}}{R^3}\times\mathbf{n}_{i,j}(\mathbf{r}')\mathrm{d}s', \tag{3.11}$$

and

$$(\sigma_i + \sigma_j)V(\mathbf{r},t) = 2\sigma_0 V_0(\mathbf{r},t) - \frac{1}{2\pi}\sum_{i,j}(\sigma_i - \sigma_j)\int_{\partial\Omega_{i,j}} V(\mathbf{r},t)\frac{\mathbf{R}}{R^3}\times \mathbf{n}_{i,j}(\mathbf{r}')\mathrm{d}s', \tag{3.12}$$

where $\partial\Omega_{i,j}$ is the contact surface between regions Ω_i and Ω_j, $\mathbf{n}_{i,j}(\mathbf{r}')$ is the unit vector normal to the surface $\partial\Omega_{i,j}$ at $\mathbf{r}'$ from region i to region j, and

$$\mathbf{B}_0(\mathbf{r},t) = \frac{\mu_0}{4\pi}\int_\Omega \mathbf{J}^p(\mathbf{r}',t)\times\frac{\mathbf{R}}{R^3}\mathrm{d}v'. \tag{3.13}$$

$$V_0(\mathbf{r},t) = \frac{1}{4\pi\sigma_0}\int_\Omega \mathbf{J}^p(\mathbf{r}',t)\times\frac{\mathbf{R}}{R^3}\mathrm{d}v'. \tag{3.14}$$

The forward problem can be solved as follow.

i. First, we compute V_0 from equation (3.14) and we find V by solving equation (3.12);

ii. Then, we compute $\mathbf{B}_0$ from equation (3.13) and, exploiting V, we compute $\mathbf{B}$ by solving equation (3.11).

The analytical resolution of these equations is doable only for very simple head geometries, e.g when the head is modelled as a set of nested concentric homogeneous spherical shells representing the different tissues. In the other cases numerical techniques are needed.

Finally, we observe that both the scalp potential V and magnetic field $\mathbf{B}$ depend linearly on the primary current $\mathbf{J}^p$.

3.2.1 The distributed source model and the discretisation of the forward problem

Experimental contexts require the discretisation of the forward problem. This involves a discretisation of both the volume occupied by the brain and the volume outside the head.

As for the first one, here we focus on the so called distributed source model. The brain volume is uniformly divided in N small parcels. If N is sufficiently big and thus each parcel has a sufficient small area, the activity in each brain parcel is approximated by a point-like source, henceforth denoted as dipole. The contribution of all the dipoles describes the current $\mathbf{J}^p$. From a mathematical point of view each dipole is an applied vector whose strength and direction represent the intensity and orientation of the primary current in the corresponding brain area.

According to this model the primary current reads

$$\mathbf{J}^p(\mathbf{r},t) = \sum_{k=1}^{N} \mathbf{q}_k(t)\delta(\mathbf{r}-\mathbf{r}_k). \tag{3.15}$$

As for the volume outside the head, it is natural to discretise it in correspondence of the sensors of the instrument we are using. Let us denote the measured magnetic field or scalp potential as $\mathbf{y}(t) = (y_1(t), \ldots, y_M(t))$, being M the number of sensors of the instrument. Now, recalling from the previous section, that both the magnetic field, $\mathbf{B}$, and the scalp potential, V, depend linearly on the primary current $\mathbf{J}^p$, it holds

$$\mathbf{y}(t) = \sum_{k=1}^{N} G(\mathbf{r}_k(t))\mathbf{q}_k(t) + \mathbf{n}(t), \tag{3.16}$$

where $G(\mathbf{r}_k) \in R^{M\times 3}$ are the leadfield matrices and $\mathbf{n}(t)$ is the measurement noise. The l-th column of $G(\mathbf{r}_k)$ contains the measurement at sensor level when a unit current dipole is placed at location $\mathbf{r}_k$ and oriented along the l-th orthogonal direction. Here we assume the orientation of the dipoles to be normal to the brain surface (Lin et al., 2006). In this case the the electric current intensities are scalars (we refer to them as $\{q_k\}_{k=1,\ldots,N}$) and the leadfield matrices are column vectors (we refer to them as $\{G_k\}_{k=1,\ldots,N}$). Let us now define

$$\mathbf{x}(t) := (q_1(t), \ldots, q_N(t)) \tag{3.17}$$

and

$$\mathbf{G} := [G_1, \ldots, G_N] \in R^{M\times N}, \tag{3.18}$$

henceforth we will refer to $\mathbf{G}$ as to the leadfield matrix. Finally, reassembling equations (3.17) and (3.18) in to equation (3.16), we get

$$\mathbf{y}(t) = \mathbf{G}\mathbf{x}(t) + \mathbf{n}(t). \tag{3.19}$$

3.3 The MEEG inverse problem

The MEEG inverse problem consists of estimating the neural activity given its corresponding sensor level recordings, that is, given equation (3.19), estimating $\mathbf{x}(t)$ from $\mathbf{y}(t)$. Having in mind the notion of well-posedness introduced in Section 2.1, the MEEG inverse problem is ill-posed as the solution is not unique and is highly sensitive to small changes in the noisy data. In particular, as for the non uniqueness, if we approximate the head with a sphere it is well know

that a radial dipole is magnetically silent, and that, a closed loop dipole is electrically silent (Hämäläinen et al., 1993). Therefore, solving the MEEG inverse problem is rather challenging and many method as been proposed over the years: Minimum Norm Estimation (MNE) (Hämäläinen and Ilmoniemi, 1984), Low Resolution Brain Electromagnetic Tomography (LORETA) (Pascual-Marqui et al., 1999), Backus and Gilbert method (Backus and Gilbert, 1968), Weighted Resolution Optimization (WROP) method (de Peralta Menendez et al., 1997), Beamformers (Van Veen and Buckley, 1988) and Sequential Monte Carlo Method (Sommariva and Sorrentino, 2014) are some examples. In this work the focus will be on truncated singular value decomposition (tSVD), Minimum Norm Estimate (MNE), and ℓ_1 regularisation method. These are the methods that have been introduced in Section 2.3, with the only difference that Tikhonov regularisation is known as MNE in the neuroscientific community.

3.4 MEEG devices

Measuring the tiny changes of the magnetic field produced by the neural currents requires highly sophisticated devices. Indeed, the magnetic noise level, produced e.g. by electric motors, elevators, power lines, is several order of magnitude higher than the biomagnetic signals (Hämäläinen et al., 1993). For this reason MEG devices are usually placed in magnetically shielded room. An MEG device consists in a helmet containing up to 500 low-Tc SQUID (low–temperature Superconducting QUantum Interface Device) sensors, placed to cover the whole head (Figure 3.4(a)). In order to detect the tiny changes of the magnetic field the sensors need to be maintained at cryogenic temperature by, e.g., immersing them in liquid helium. Typically, in a MEG device two types of sensors device may be found: magnetometers and gradiometers. The former measure the component of the magnetic field perpendicular to the surface of the MEG helmet and they are sensitive to fields originating from a broad distance. The latter, on the other hand, estimate the spatial derivative in two orthogonal directions perpendicular to the MEG helmet, so that their sensitivity decreases faster with distance (Garcés et al., 2017). The main drawback of using SQUID sensors is that they are placed about two centimetres away from the head surface of the subject, moreover, due to the need for liquid helium, their maintenance is very expensive. The Optically Pumped Magnetometers (OPMs) (Figure 3.4(b)) are meant to overcome such problems. Indeed, with respect to the SQUID sensors they are closer to the head surface. Moreover OPM sensors are placed on a wearable helmet, thus they are more robust to motion and they are more practical either when the subject is asked to perform a task during the recording session or when dealing with children or patients. Finally, they are

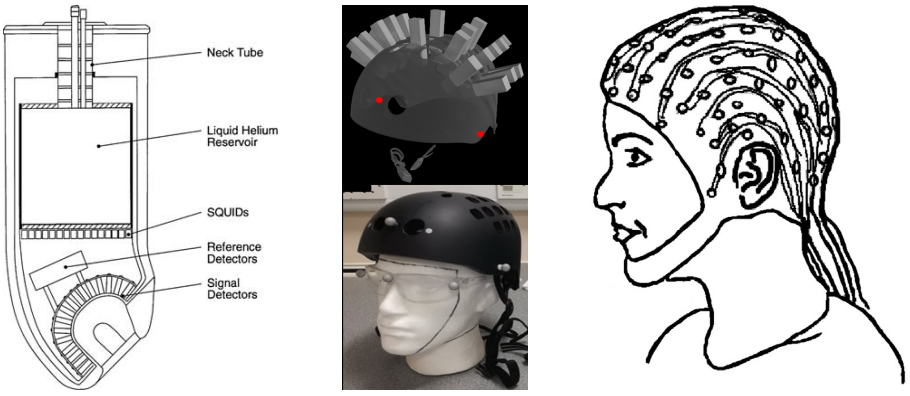

(a) (b) (c)

Figure 3.4: (a) SQUID sensor MEG device (König et al., 2007). (b) OPM sensor MEG device (Hill et al., 2019). (c) EEG device (Jestrović et al., 2014).

cheaper since they do not require to be immersed in liquid helium.

An EEG device (Figure 3.4(c)) consists of a cap covered with up to 256 electrodes that are in direct contact with the head surface. Electrodes have a simple design consisting of a metal contact surface. The most commonly used electrodes are chlorided silver discs (Ebner et al., 1999). With respect to MEG, EEG is cheaper and portable. The time resolution of MEEG and EEG are comparable, however EEG is more sensitive to the inhomogeneous conductivity of the head tissues, resulting in a lower spatial resolution.

3.5 Brain connectivity

The functional organisation of the brain is characterised by the processes of segregation and integration of information (Figure 3.5). The former refers to the fact that the brain is divided into areas dedicated to specific functions. Within these areas there is a high density of connections, while connections between different areas have a lower density. On the other hand, the process of integration refers to information exchange between areas characterised by a high density of connections (Sporns, 2013). The anatomical and functional connections between different areas of the brain are organised in such a way that the processes of segregation and integration are optimal. Conventionally, three different types of connectivity are defined (Lang et al., 2012; He et al., 2019).

- Anatomical (or structural) connectivity forms the connectome, i.e. that network consisting of all the connections between adjacent neurons and nerve

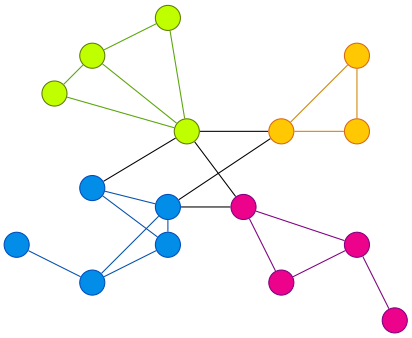

Figure 3.5: Schematic representation of the concepts of integration and segregation. The dense connections among nodes of the same colours represent the process of segregation, while the fewer connections among nodes of different colours (depicted by the black lines) represent the process of integration.

fibres. On a short time scale (seconds and minutes) the anatomical connections are persistent and stable.

- Functional connectivity is defined as the statistical dependence between neuronal activation in separate areas of the brain. This is a statistical concept based on measures such as correlation, covariance and coherence. Functional connectivity, being measured by statistical quantities, has a strong temporal dependence.

- Effective connectivity describes the influence that one neuronal system exerts on the other, thus reflecting the causal interactions between the different active areas of the brain.

The study of anatomical, functional and effective connectivity leads to a better understanding of all the processes that take place in the brain. Throughout this thesis we will focus on functional connectivity. Indeed, since brain activity can be interpreted as the realisation of a multivariate stochastic process, statistical connectivity metrics are a great tool to identify the dependencies among the time courses that describe the activity of each source. In the next section we will go through some of the most commonly used connectivity metrics.

3.6 Metrics and computation

With the term connectivity metrics we refer to a wide range of statistical metrics that aim at quantifying and explaining the statistical interdependence between different signals. From an operative point of view, functional connectivity may be measured at sensor level, where it quantifies the interdependence among the time

series provided by the MEEG sensors, or at source space level, where it quantifies the interdependence between the time series associated with different brain areas o sources.

A large variety of connectivity metrics have been proposed over the years, which can be used to quantify functional connectivity either in the sensor or in the source spaces. There are linear and non linear metrics to detect linear and non linear interactions; there are time based metrics and frequency based metrics; and still, there are parametric and non parametric metrics (Bastos and Schoffelen, 2016; Sakkalis, 2011; Pereda et al., 2005). An exhaustive description of all the metrics is beyond the scope of this thesis. In the following some linear, frequency based metrics will be described.

3.6.1 Coherence and its derivatives

Definition 3.1. Let $\{\mathbf{x}(t)\}_{t=0}^{T-1}$ be the realisation of a multivariate stochastic process of dimension N. For each pair $\{X_j(t), X_k(t)\}$, $j, k \in \{1, \ldots, N\}$, the Coherency function at frequency f is defined as

$$COH_{j,k}(f) = \frac{\tilde{S}_{j,k}(f)}{\sqrt{\tilde{S}_{j,j}(f)\tilde{S}_{k,k}(f)}}, \tag{3.20}$$

where $\tilde{S}_{j,k}(f)$ is the estimated cross-power spectrum between $x_j(t)$ and $x_k(t)$ as defined in Section 1.3.
Given the coherency function, the coherence function is defined as its magnitude, i.e

$$\Gamma_{j,k}(f) = \frac{|\tilde{S}_{j,k}(f)|}{\sqrt{\tilde{S}_{j,j}(f)\tilde{S}_{k,k}(f)}}, \tag{3.21}$$

Coherency ranges from 0 to 1. When $\Gamma_{j,k}(f) = 0$ the activities of the two signals $\{x_j(t), x_k(t)\}$ at frequency f are linearly independent. On the contrary, $\Gamma_{j,k}(f) = 1$ indicates maximum correlation between the signals (Pereda et al., 2005). It is also worth noticing that coherence is sensitive to both phase and amplitude changes in the signals, therefore it may not be altogether clear the weight of each of such contributions (Lachaux et al., 1999).

One of the main issues that connectivity metrics have to face is volume conduction, i.e. the transmission of an electric primary current source through biological tissue. Such a phenomenon is responsible for signal spread at sensor level, that is the activity of one source may be detected by multiple sensors, resulting in connectivity values that do not reflect the actual connectivity patterns. On the other

hand, volume conduction, together with intrinsic limitations of the inverse operators employed to estimate brain activity, is also responsible of spatial blur at source level. This means that the estimated activity at a given location leaks to other locations resulting in artificial and spurious interactions between the estimated sources activity. To overcome these problems Nolte and colleagues (Nolte et al., 2004) suggested to only consider the imaginary part of coherency which necessarily reflects true interactions.

Definition 3.2. Let $\{\mathbf{x}(t)\}_{t=0}^{T-1}$ be the realisation of a multivariate stochastic process of dimension N. For each pair $\{x_j(t), x_k(t)\}$, $j, k \in \{1, \ldots, N\}$, the imaginary part of coherency at frequency f is defined as

$$imCOH_{j,k}(f) = \frac{\text{Im}(\tilde{S}_{j,k}(f))}{\sqrt{\tilde{S}_{j,j}(f)\tilde{S}_{k,k}(f)}}. \tag{3.22}$$

3.6.2 Phase Locking Value and its derivatives

Definition 3.3. Let $\{\mathbf{x}(t)\}_{t=0}^{T-1}$ be the realisation of a multivariate stochastic process of dimension N. For each pair $\{x_j(t), x_k(t)\}$, $j, k \in \{1, \ldots, N\}$, the Phase Locking Value (PLV) at frequency f is defined as

$$PLV_{j,k}(f) = \frac{1}{P}\left|\sum_{p=1}^{P} \frac{\hat{x}_j^{(p)}(f)\hat{x}_k^{(p)}(f)^*}{|\hat{x}_j^{(p)}(f)||\hat{x}_k^{(p)}f)|}\right|, \tag{3.23}$$

where P is the number of segments (or tapers) as defined in Sections 1.3.1 and 1.3.2; and $\hat{x}^{(p)}$ is defined as in equations (1.18) or (1.23), accordingly to the method used for the computation of the cross-power spectrum (i.e. Welch's method or multitapers).

PLV was introduced by Lachaux and colleagues (Lachaux et al., 1999) with the purpose of quantifying the phase synchronisation of pairs of signals. PLV ranges from 0 to 1 and it assumes value 0 when there is no phase synchronisation and value 1 when there is perfect synchronisation.
Similarly to the case of coherency, also PLV came with two variations in order to suppress zero-lag connectivity associated with volume conduction and source leakage, namely the imaginary part of PLV ($iPLV$) and the corrected imaginary part of PLV ($ciPLV$), defined as follow (Bruña et al., 2018).

Definition 3.4. Let $\{\mathbf{x}(t)\}_{t=0}^{T-1}$ be the realisation of a multivariate stochastic process of dimension N. For each pair $\{x_j(t), x_k(t)\}$, $j, k \in \{1, \ldots, N\}$, the $iPLV$

at frequency f is defined as

$$iPLV_{j,k}(f) = \frac{1}{P}\left|\sum_{p=1}^{P}\frac{\mathrm{Im}\left(\hat{x}_j^{(p)}(f)\hat{x}_k^{(p)}(f)^*\right)}{|\hat{x}_j^{(p)}(f)||\hat{x}_k^{(p)}f)|}\right|, \tag{3.24}$$

while the $ciPLV$ at frequency f is defined as

$$ciPLV_{j,k}(f) = \frac{\frac{1}{P}\left|\sum_{p=1}^{P}\frac{\mathrm{Im}\left(\hat{x}_j^{(p)}(f)\hat{x}_k^{(p)}(f)^*\right)}{|\hat{x}_j^{(p)}(f)||\hat{x}_k^{(p)}f)|}\right|}{\sqrt{1-\left(\frac{1}{P}\left|\sum_{p=1}^{P}\frac{\mathrm{Im}\left(\hat{x}_j^{(p)}(f)\hat{x}_k^{(p)}(f)^*\right)}{|\hat{x}_j^{(p)}(f)||\hat{x}_k^{(p)}f)|}\right|\right)^2}}, \tag{3.25}$$

where P is the number of segments (or tapers) as defined in sections 1.3.1 and 1.3.2; $\hat{x}^{(p)}$ is defined as in equations (1.18) or (1.23), accordingly to the method used for the computation of the cross-power spectrum (i.e. Welch's method or multitapers); and $\mathrm{Im}(\cdot)$ is the imaginary part.

3.6.3 Phase Lag Index and its derivatives

Definition 3.5. Let $\{\mathbf{x}(t)\}_{t=0}^{T-1}$ be the realisation of a multivariate stochastic process of dimension N. For each pair $\{x_j(t), x_k(t)\}$, $j,k \in \{1,\ldots,N\}$, the Phase Lag Index (PLI) at frequency f is defined as

$$PLI_{j,k}(f) = \left|\frac{1}{P}\sum_{p=1}^{P}\mathrm{Im}\left(\hat{x}_j^{(p)}(f)\hat{x}_k^{(p)}(f)^*\right)\right|, \tag{3.26}$$

where P is the number of segments (or tapers) as defined in sections 1.3.1 and 1.3.2; $\hat{x}^{(p)}$ is defined as in equation (1.18) of (1.23), accordingly to the method used for the computation of the cross-power spectrum (i.e. Welch's method or multitapers); and $\mathrm{Im}(\cdot)$ is the imaginary part.

PLI was introduced by Stam and colleagues (Stam et al., 2007) with the aim of obtaining a reliable estimate of phase synchronisation that is invariant to volume conduction and source leakage. The PLI ranges from 0 to 1; a value of 0 indicates either no coupling or a coupling centred around $k\pi$, whereas a value of 1 indicates perfect coupling at a phase difference different from $k\pi$.
Successively, Vink and colleagues (Vinck et al., 2010) introduced the weighted PLI ($wPLI$) to overcome the high sensitivity of the PLI to small perturbation of the phase around zero due to the noise effects, which turn phase lags into leads and vice versa.

Definition 3.6. Let $\{\mathbf{x}(t)\}_{t=0}^{T-1}$ be the realisation of a multivariate stochastic process of dimension N. For each pair $\{x_j(t), x_k(t)\}$, $j, k \in \{1, \dots, N\}$, the weighted Phase Lag Index ($wPLI$) at frequency f is defined as

$$wPLI_{j,k}(f) = \frac{\left|\mathrm{Im}\left(\tilde{S}_{j,k}(f)\right)\right|}{\frac{1}{P}\sum_{p=1}^{P}\left|\mathrm{Im}\left(\hat{x}_j^{(p)}(f)\hat{x}_k^{(p)}(f)^*\right)\right|}, \tag{3.27}$$

where P is the number of segments (or tapers) as defined in sections 1.3.1 and 1.3.2; $\hat{x}^{(p)}$ is defined as in equations (1.18) or (1.23), accordingly to the method used for the computation of the cross-power spectrum (i.e. Welch's method or multitapers); and $\mathrm{Im}(\cdot)$ is the imaginary part.

As final remark, we must say that all functional connectivity measures can provide insightful information on brain functioning, however it is good practice to gather such information with those obtained by other analysis approaches. Indeed, for instance, it has been demonstrated that features derived from the power spectrum of the individual sources and features derived from functional connectivity metrics are not independent (Demuru et al., 2020), therefore they have to be considered together rather than apart.

3.7 The two-step approach and its drawbacks

As mentioned above, functional connectivity can be estimated either at sensor level or at source space level. However, the latter approach is preferable, as it has the advantage of reducing the impact of volume conduction and providing more easily interpretable results (Lai et al., 2018; Schoffelen and Gross, 2009; Barzegaran and Knyazeva, 2017; Van de Steen et al., 2019).

The general workflow for connectivity estimation at source space level relies on a two–step process (Schoffelen and Gross, 2019a):

i. First neural activity is estimated by solving the MEEG inverse problem;

ii. Then functional connectivity is computed using a desired metric.

Naturally, the connectivity estimate achieved in the second step will depend on the inverse method used to estimate the neural activity during the first step and on the possible parameters that are required to apply the chosen method. Indeed, in the next chapters we will see that this two-step approach may hide some pitfalls, as, counter-intuitively, the best possible neural activity estimate may not lead to the best possible connectivity estimate.

Chapter 4

Analytical results on the two-step estimation of the cross-power spectrum

As mentioned at the end of the previous chapter, functional connectivity is usually estimated in a two-step process: first, an estimate of the source time courses is obtained using an inverse method; then, frequency-domain connectivity metrics are computed from the cross-power spectrum of the reconstructed source time courses. However, empirical evidence suggests that the two-step approach might feature an unexpected parameter tuning issue. Indeed, as seen in Chapter 2, usual regularisation approaches require the selection of a proper regularisation parameter. It would seem natural that the optimal estimate of the cross-power spectrum can only be attained with the optimal reconstruction of the signal. Yet, in (Hincapié et al., 2016) the authors have shown that the value of the regularisation parameter that provides the best reconstruction of the source spectral power does not coincide with the value that provides the best reconstruction of the source-level functional connectivity quantified through coherence.

In this chapter we present the results published in (Vallarino et al., 2020). That is, motivated by the empirical result presented in (Hincapié et al., 2016), we investigate the following problem: let $\mathbf{y}(t)$ be noisy and indirect measurements of a multivariate stochastic process $\mathbf{X}(t)$; let $\mathbf{x}_\lambda(t)$ be the reconstruction of the hidden signal, obtained by means of a regularisation algorithm; finally, assume that the cross-power spectrum of $\mathbf{X}(t)$, $\mathbf{S}^{\mathbf{X}}(f)$, is estimated from the reconstructed signal $\mathbf{x}_\lambda(t)$; under these conditions, does the optimal regularisation parameter for the reconstruction of the hidden signal coincide with the optimal regularisation parameter for the reconstruction of its cross-power spectrum?

In particular, we will see that the answer is "no" when the regularised solution

is computed via Tikhonov regularisation, thus confirming the empirical results of (Hincapié et al., 2016). We will also see that the answer is "yes" when the regularised solution is computed via tSVD, thus showing that the answer to the question actually depends on the choice of the inverse method. In addition, the potential of a one-step approach relying on a mathematical model directly relating the measured data to the unknown cross-power spectrum will be shown.

This chapter is organised as follow: in Section 4.1 we provide the general definitions and formalise the problem. In Section 4.2 we express the reconstructions errors in terms of the filter factors and provide an interpretation. Section 4.3 contains the main results of this chapter. In Section 4.4 we compare the filter factors of the two-step approach with those of a possible one-step approach. In Section 4.5 we show the results of a numerical simulation in which we remove the somewhat restrictive assumptions that are needed to prove the theorems of Section 4.2. The results will be discussed in Section 4.6.

4.1 Definition of the problem

Let us consider the MEEG problem (3.19)

$$\mathbf{y}(t) = \mathbf{G}\mathbf{x}(t) + \mathbf{n}(t),$$

being $\mathbf{y}(t) \in \mathbb{R}^M$, $\mathbf{x}(t) \in \mathbb{R}^N$ and $\mathbf{n}(t) \in \mathbb{R}^M$ realisations of the multivariate stochastic processes $\mathbf{Y}(t)$, $\mathbf{X}(t)$ and $\mathbf{N}(t)$, and $\mathbf{G} \in \mathbb{R}^{M\times N}$ a leadfield matrix. $\mathbf{N}(t)$ is the measurement noise process, which is assumed to be a zero-mean Gaussian process independent from $\mathbf{X}(t)$. For ease of presentation, we further assume $M \leq N$ and $\mathbf{G}$ to be a full row rank matrix so that all its singular values are strictly positive; however, the results below can be easily extended to the general case.

We consider the case where one is interested in reconstructing the cross-power spectrum of the process $\mathbf{X}(t)$, as defined in Definition 1.12 and we consider the case when the reconstruction of the cross-power spectrum is achieved in a two-step process as described in Section 3.7 and the estimate is computed with the Welch's method (Welch, 1967).
In this work we will focus on tSVD and Tikhonov regularisation. The reason of this specific choice is as follows: the Tikhonov method is one of the more commonly employed methods for connectivity estimation in MEEG, and it has been used by Hincapié and colleagues in the paper that motivated this study (Hincapié et al., 2016); tSVD is a method which is easy to deal with analytically, and in addition it will provide a different result than the Tikhonov method, thus showing that the answer to the main question of this study is method-dependent.

We recall that, by means of Equations (2.16a) and (2.16b), the regularised so-

lution reads

$$\begin{aligned}\mathbf{x}_\lambda(t) &= \mathbf{W}_\lambda \mathbf{y}(t) = \mathbf{V}\boldsymbol{\Phi}(\lambda)\boldsymbol{\Sigma}^\dagger \mathbf{U}^\top \mathbf{y}(t) \\ &= \sum_{i=1}^{M} \varphi_i(\lambda) \frac{\mathbf{u}_i^\top \mathbf{y}(t)}{\sigma_i} \mathbf{v}_i,\end{aligned}$$

being $\mathbf{u}_i$ and $\mathbf{v}_i$ the i-th columns of $\mathbf{U}$ and $\mathbf{V}$, with $\mathbf{G} = \mathbf{U}\boldsymbol{\Sigma}\mathbf{V}^\top$, $\boldsymbol{\Sigma} = \text{diag}(\sigma_1, \ldots, \sigma_M)$ and being the i-th component of the filter factors

$$\varphi_i(\lambda) = \begin{cases} 1 & \text{if} \quad i \leq \lambda \\ 0 & \text{if} \quad i > \lambda \end{cases} \qquad \lambda \in \{1, \ldots, M\} \tag{4.1}$$

in case of tSVD and

$$\varphi_i(\lambda) = \frac{\sigma_i^2}{\sigma_i^2 + \lambda} \qquad \lambda \geq 0. \tag{4.2}$$

in case of Tikhonov regularisation.

On the other hand, using the Welch's method, the cross-power spectrum estimate will be given by

$$\mathbf{S}^{\mathbf{x}_\lambda}(f) = \frac{1}{PW} \sum_{p=1}^{P} \hat{\mathbf{x}}_\lambda^p(f) \hat{\mathbf{x}}_\lambda^p(f)^H, \qquad f = 0, \ldots, L-1, \tag{4.3}$$

being $\hat{\mathbf{x}}_\lambda^p(f) = \sum_{t=0}^{L-1} \mathbf{x}_\lambda^p(t) w(t) e^{-\frac{2\pi i t f}{L}}$ and $W = \sum_{t=0}^{L-1} w(t)^2$. We stress out the dependence of the cross-power spectrum on λ.

From now on, for simplicity, we omit the dependence of $\boldsymbol{\Phi}$ and φ_i on λ. Also note that in the two methods the parameter λ assumes values in different sets. In tSVD λ determines the number of retained SVD components, and therefore assumes integer values in $\{1, \ldots, M\}$, where a small λ value means few retained components and thus an high level of regularisation. In Tikhonov regularisation λ determines the strength with which each SVD component contributes to the solution; in this case λ assumes continuous values in $[0, +\infty)$ and the higher the value the higher the degree of regularisation.

For the two mentioned methods, we consider the problem of the optimal choice of the regularisation parameter λ for the reconstruction of the cross-power spectrum. We define optimality through the minimisation of the norm of the discrepancy, specifically we define the two following optimal values for the parameter.

Definition 4.1. Consider the regularised solution (2.16a) and the cross-power spectrum estimate (4.3) associated with a realisation of equation (3.19); we define the

optimal parameter for the reconstruction of $\mathbf{x}(t)$

$$\lambda^*_{\mathbf{x}} = \arg\min_{\lambda} \varepsilon_{\mathbf{x}}(\lambda) \quad \text{with} \quad \varepsilon_{\mathbf{x}}(\lambda) = \sum_t \|\mathbf{x}_\lambda(t) - \mathbf{x}(t)\|_2^2 \quad , \tag{4.4}$$

and the optimal parameter for the reconstruction of $\mathbf{S}^{\mathbf{x}}(f)$

$$\lambda^*_{\mathbf{S}} = \arg\min_{\lambda} \varepsilon_{\mathbf{S}}(\lambda) \quad \text{with} \quad \varepsilon_{\mathbf{S}}(\lambda) = \sum_f \|\mathbf{S}^{\mathbf{x}_\lambda}(f) - \mathbf{S}^{\mathbf{x}}(f)\|_F^2 \quad , \tag{4.5}$$

where $\|\cdot\|_2$ and $\|\cdot\|_F$ are the ℓ_2-norm and the Frobenius norm, respectively; $\varepsilon_{\mathbf{x}}(\lambda)$ and $\varepsilon_{\mathbf{S}}(\lambda)$ will be called reconstruction errors.

In the following sections we shall answer the following question: does the optimal regularisation parameter for the reconstruction of $\mathbf{x}(t)$, $\lambda^*_{\mathbf{x}}$, coincide with the optimal regularisation parameter for the reconstruction of $\mathbf{S}^{\mathbf{x}}(f)$, $\lambda^*_{\mathbf{S}}$?

4.2 Reconstruction errors with filter factors

In this section we aim at deriving an explicit formulation of $\varepsilon_{\mathbf{x}}(\lambda)$ and $\varepsilon_{\mathbf{S}}(\lambda)$ in terms of the filter factors $\mathbf{\Phi}$. To this end we observe that from equations (3.19) and (2.16a) we can derive the following relationship between the true and the reconstructed signal:

$$\mathbf{x}_\lambda(t) = \mathbf{R}_\lambda \mathbf{x}(t) + \mathbf{W}_\lambda \mathbf{n}(t) \tag{4.6}$$

where $\mathbf{R}_\lambda = \mathbf{W}_\lambda \mathbf{G}$ is the resolution matrix (de Peralta Menendez et al., 1996; Hansen, 2005).

A similar relationship between the true and the estimated cross-power spectrum can be derived by substituting equation (4.6) into definition (4.3) and by exploiting the linearity of the Discrete Fourier Transform:

$$\mathcal{S}^{\mathbf{x}_\lambda}(f) = (\mathbf{R}_\lambda \otimes \mathbf{R}_\lambda)\, \mathcal{S}^{\mathbf{x}}(f) + (\mathbf{W}_\lambda \otimes \mathbf{W}_\lambda)\, \mathcal{S}^{\mathbf{n}}(f) \tag{4.7}$$

$$+ (\mathbf{W}_\lambda \otimes \mathbf{R}_\lambda)\, \mathcal{S}^{\mathbf{xn}}(f) + (\mathbf{R}_\lambda \otimes \mathbf{W}_\lambda)\, \mathcal{S}^{\mathbf{nx}}(f) \quad , \tag{4.8}$$

where $\mathcal{S}^{\mathbf{x}}(f)$ is the vector obtained by concatenating the columns of the matrix $\mathbf{S}^{\mathbf{x}}(f)$, $\otimes$ is the Kronecker product, and $\mathbf{S}^{\mathbf{xn}}(f)$ is the cross-spectrum between $\mathbf{x}$ and $\mathbf{n}$, i.e., following the notation in equation (4.3), $\mathbf{S}^{\mathbf{xn}}(f) = \frac{1}{PW} \sum_{p=1}^{P} \hat{\mathbf{x}}^p(f) \hat{\mathbf{n}}^p(f)^H$.

Since $\mathbf{X}(t)$ and $\mathbf{N}(t)$ are independent, $\mathcal{S}^{\mathbf{xn}}(f)$ and $\mathcal{S}^{\mathbf{nx}}(f)$ are negligible provided that enough data time-points are available. Hence from Definition 4.1 it follows

$$\varepsilon_{\mathbf{x}}(\lambda) = \sum_t \|(\mathbf{R}_\lambda - \mathbf{I}_N)\, \mathbf{x}(t) + \mathbf{W}_\lambda \mathbf{n}(t)\|_2^2 \tag{4.9}$$

$$\varepsilon_{\mathbf{S}}(\lambda) = \sum_f \left\| \left(\mathbf{R}_\lambda \otimes \mathbf{R}_\lambda - \mathbf{I}_{N^2}\right) \mathcal{S}^{\mathbf{x}}(f) + \left(\mathbf{W}_\lambda \otimes \mathbf{W}_\lambda\right) \mathcal{S}^{\mathbf{n}}(f) \right\|_2^2 \tag{4.10}$$

where $\mathbf{I}_N$ is the identity matrix of size $N \times N$.

Proposition 4.2. *The reconstruction errors defined in (4.4) and (4.5) are given by:*

$$\varepsilon_{\mathbf{x}}(\lambda) = \sum_t \sum_{i=M+1}^{N} \left(\mathbf{v}_i^\top \mathbf{x}(t)\right)^2 + \sum_t \sum_{i=1}^{M} \left[(\varphi_i - 1)^2 \left(\mathbf{v}_i^\top \mathbf{x}(t)\right)^2 + \varphi_i^2 \frac{\left(\mathbf{u}_i^\top \mathbf{n}(t)\right)^2}{\sigma_i^2} \right] \tag{4.11}$$

and

$$\begin{aligned} \varepsilon_{\mathbf{S}}(\lambda) = \sum_f \sum_{\substack{i \geq M+1 \text{ or} \\ j \geq M+1}} \left| (\mathbf{v}_i \otimes \mathbf{v}_j)^\top \mathcal{S}^{\mathbf{x}}(f) \right|^2 + \sum_f \sum_{i,j=1}^{M} \Bigg[& (\varphi_i \varphi_j - 1)^2 \left| (\mathbf{v}_i \otimes \mathbf{v}_j)^\top \mathcal{S}^{\mathbf{x}}(f) \right|^2 \\ & + \left(\frac{\varphi_i \varphi_j}{\sigma_i \sigma_j} \right)^2 \left| (\mathbf{u}_i \otimes \mathbf{u}_j)^\top \mathcal{S}^{\mathbf{n}}(f) \right|^2 + 2 (\varphi_i \varphi_j - 1) \frac{\varphi_i \varphi_j}{\sigma_i \sigma_j} Re \left(\overline{(\mathbf{v}_i \otimes \mathbf{v}_j)^\top \mathcal{S}^{\mathbf{x}}(f)} (\mathbf{u}_i \otimes \mathbf{u}_j)^\top \mathcal{S}^{\mathbf{n}}(f) \right) \Bigg] \end{aligned} \tag{4.12}$$

Proof. To prove equation (4.11) we observe that

$$\mathbf{W}_\lambda = \mathbf{V} \mathbf{\Phi} \mathbf{\Sigma}^\dagger \mathbf{U}^\top = \sum_{i=1}^{M} \mathbf{v}_i \frac{\varphi_i}{\sigma_i} \mathbf{u}_i^\top$$

and

$$\mathbf{R}_\lambda - \mathbf{I}_N = \mathbf{V} \mathbf{\Phi} \mathbf{\Sigma}^\dagger \mathbf{\Sigma} \mathbf{V}^\top - \mathbf{I}_N = \sum_{i=1}^{M} \mathbf{v}_i (\varphi_i - 1) \mathbf{v}_i^\top - \sum_{i=M+1}^{N} \mathbf{v}_i \mathbf{v}_i^\top .$$

Then the thesis follows from equation (4.9) by exploiting the orthonormality of $\mathbf{V}$ and the independence between processes $\mathbf{X}(t)$ and $\mathbf{N}(t)$.
Analogously, equation (4.12) follows from equation (4.10) by observing

$$\mathbf{W}_\lambda \otimes \mathbf{W}_\lambda = (\mathbf{V} \otimes \mathbf{V}) \left(\mathbf{\Phi} \mathbf{\Sigma}^\dagger \otimes \mathbf{\Phi} \mathbf{\Sigma}^\dagger \right) (\mathbf{U} \otimes \mathbf{U})^\top = \sum_{i,j=1}^{M} (\mathbf{v}_i \otimes \mathbf{v}_j) \frac{\varphi_i \varphi_j}{\sigma_i \sigma_j} (\mathbf{u}_i \otimes \mathbf{u}_j)^\top$$

and

$$\begin{aligned} \mathbf{R}_\lambda \otimes \mathbf{R}_\lambda - \mathbf{I}_{N^2} &= (\mathbf{V} \otimes \mathbf{V}) \left(\mathbf{\Phi} \mathbf{\Sigma}^\dagger \mathbf{\Sigma} \otimes \mathbf{\Phi} \mathbf{\Sigma}^\dagger \mathbf{\Sigma} - \mathbf{I}_{N^2} \right) (\mathbf{V} \otimes \mathbf{V})^\top \\ &= \sum_{i,j=1}^{M} (\mathbf{v}_i \otimes \mathbf{v}_j)(\varphi_i \varphi_j - 1)(\mathbf{v}_i \otimes \mathbf{v}_j)^\top - \sum_{\substack{i \geq M+1 \text{ or} \\ j \geq M+1}} (\mathbf{v}_i \otimes \mathbf{v}_j)(\mathbf{v}_i \otimes \mathbf{v}_j)^\top \end{aligned}$$

□

Remark 4.3. *The expression in (4.11) is a classic result in regularisation theory (Hansen, 2005), in which the reconstruction error is expressed in terms of three distinct components. The first component is the norm of the projection of the original signal onto the kernel of* $\mathbf{G}$*, i.e. the part of the signal that cannot be reconstructed. The second term is the regularisation error, i.e. the error introduced by regularisation itself; indeed, this term vanishes when the value of all the filters is one. The last term is the perturbation error, i.e. the backprojection of stochastic noise components onto the reconstructed signal, that regularisation tries to reduce.*

Remark 4.4. *Expression (4.12) is the analogue of (4.11) for the cross-power spectrum estimated with the two-step approach. The reconstruction error* $\varepsilon_{\mathbf{S}}(\lambda)$ *here is made of four distinct components: three of them have the same interpretation of those appearing in* $\varepsilon_{\mathbf{x}}(\lambda)$*; the fourth term is a non-vanishing mixed term, that depends on both the signal and the noise spectra; as we shall see below, this term turns out to be negative at least in some special cases.*

4.3 The relationship between the optimal regularisation parameters: two case studies

We will now address the main question posed in the introduction of the current chapter: does the optimal regularisation parameter for the reconstruction of the time-series coincide with the optimal regularisation parameter for the reconstruction of the cross-power spectrum? As we shall see, the answer depends on the specific choice of the inverse method, i.e. on the form of the filter factors. Here we study first the case of tSVD, and then the case of the Tikhonov method.

In order to proceed analytically, in this section we make the further assumption that both the signal and the noise are white-noise Gaussian processes, with covariance matrices $\omega^2\mathbf{I}_N$ and $\alpha^2\mathbf{I}_M$, respectively. The Gaussian assumption is often not too far fetched; in MEEG, particularly, it is widely used and, even though perhaps the data distribution is not exactly Gaussian, the Gaussian assumption is implicit (when not explicit) in the vast majority of connectivity studies (Nolte et al., 2019). The white-noise assumption, on the other hand, is stronger, as it implies that there is no temporal structure in the signal: we will come back to this point in Section 4.6.

4.3.1 Truncated SVD

When tSVD is employed, by substituting the values of the corresponding filter factors into equations (4.11) and (4.12) we get the following corollary of Proposition 4.2.

Corollary 4.5. *Consider the tSVD estimate $\mathbf{x}_\lambda(t)$ given by equation* (2.16b)*, with regularisation parameter $\lambda \in \{1, \dots, M\}$. Then*

$$\varepsilon_{\mathbf{x}}(\lambda) = \sum_t \sum_{i=\lambda+1}^{N} \left(\mathbf{v}_i^\top \mathbf{x}(t)\right)^2 + \sum_t \sum_{i=1}^{\lambda} \frac{\left(\mathbf{u}_i^\top \mathbf{n}(t)\right)^2}{\sigma_i^2} \tag{4.13}$$

and

$$\varepsilon_{\mathbf{S}}(\lambda) = \sum_f \sum_{\substack{i\geq\lambda+1 \text{ or} \\ j\geq\lambda+1}} \left|(\mathbf{v}_i \otimes \mathbf{v}_j)^\top \mathcal{S}^{\mathbf{x}}(f)\right|^2 + \sum_f \sum_{i,j=1}^{\lambda} \frac{\left|(\mathbf{u}_i \otimes \mathbf{u}_j)^\top \mathcal{S}^{\mathbf{n}}(f)\right|^2}{\sigma_i^2 \sigma_j^2} \tag{4.14}$$

Remark 4.6. *When regularisation is accomplished through tSVD, the mixed term in $\varepsilon_{\mathbf{S}}(\lambda)$ vanishes; this allows us to compute the optimal regularisation parameter explicitly.*

Theorem 4.7. *Let $x_\lambda(t)$ be the tSVD estimate as given by equation* (2.16b)*, with regularisation parameter $\lambda \in \{1, \dots, M\}$; assume $\mathbf{X}(t)$ and $\mathbf{N}(t)$ to be white-noise Gaussian processes with covariance matrices $\omega^2\mathbf{I}_N$ and $\alpha^2\mathbf{I}_M$, respectively. Then*

$$\lambda_{\mathbf{x}}^* = \lambda_{\mathbf{S}}^* = \max\left\{\lambda \in \{1, \dots, M\} \; s.t \; \sigma_\lambda \geq \frac{\alpha}{\omega}\right\} \tag{4.15}$$

Proof. As $\mathbf{X}(t)$ and $\mathbf{N}(t)$ are white-noise Gaussian processes with covariance matrices $\omega^2\mathbf{I}_N$ and $\alpha^2\mathbf{I}_M$, we have $\mathbf{S}^{\mathbf{x}}(f) = \omega^2\mathbf{I}_N$ and $\mathbf{S}^{\mathbf{n}}(f) = \alpha^2\mathbf{I}_M$. Provided that enough data time-points are available[1], these imply that

$$\sum_t \left(\mathbf{v}_i^\top \mathbf{x}(t)\right)^2 = T\omega^2 \qquad \sum_t \left(\mathbf{u}_i^\top \mathbf{n}(t)\right)^2 = T\alpha^2 \tag{4.16}$$

and

$$\left|(\mathbf{v}_i \otimes \mathbf{v}_j)^\top \mathcal{S}^{\mathbf{x}}(f)\right|^2 = \omega^4 \left|\mathbf{v}_j^\top \mathbf{v}_i\right|^2 = \omega^4 \delta_{ij} \tag{4.17}$$

$$\left|(\mathbf{u}_i \otimes \mathbf{u}_j)^\top \mathcal{S}^{\mathbf{n}}(f)\right|^2 = \alpha^4 \left|\mathbf{u}_j^\top \mathbf{u}_i\right|^2 = \alpha^4 \delta_{ij} \tag{4.18}$$

where δ_{ij} is the Kronecker delta. By substituting equalities (4.16)-(4.18) in equations (4.13) and (4.14) we get

$$\varepsilon_{\mathbf{x}}(\lambda) = (N - \lambda)\, T\omega^2 + T\alpha^2 \sum_{i=1}^{\lambda} \frac{1}{\sigma_i^2}$$

[1]The sufficient number of time points is of course dependent on the size of the problem, and in particular it grows with the dimensions of the data and of the unknown.

$$\varepsilon_{\mathbf{S}}(\lambda) = (N-\lambda)\, L\omega^4 + L\alpha^4 \sum_{i=1}^{\lambda} \frac{1}{\sigma_i^4}$$

The thesis follows by observing that the increments

$$\varepsilon_{\mathbf{x}}(\lambda) - \varepsilon_{\mathbf{x}}(\lambda-1) = -T\omega^2 + \frac{T\alpha^2}{\sigma_\lambda^2}$$

and

$$\varepsilon_{\mathbf{S}}(\lambda) - \varepsilon_{\mathbf{S}}(\lambda-1) = -L\omega^4 + \frac{L\alpha^4}{\sigma_\lambda^4}$$

are non-decreasing functions of λ and thus $\varepsilon_{\mathbf{x}}(\lambda)$ and $\varepsilon_{\mathbf{S}}(\lambda)$ have a unique minimum at the biggest λ for which such increments are negative. □

4.3.2 Tikhonov method

We now consider the case when regularisation is performed by means of the standard Tikhonov formula.

Corollary 4.8. *Let $x_\lambda(t)$ be the Tikhonov estimate as given by equation (2.16b), with regularisation parameter $\lambda \geq 0$. Then*

$$\begin{aligned}\varepsilon_{\mathbf{x}}(\lambda) = &\sum_t \sum_{i=M+1}^{N} \left(\mathbf{v}_i^\top \mathbf{x}(t)\right)^2 \\ &+ \sum_t \sum_{i=1}^{M} \left[\frac{\lambda^2}{(\sigma_i^2+\lambda)^2} \left(\mathbf{v}_i^\top \mathbf{x}(t)\right)^2 + \frac{\sigma_i^2}{(\sigma_i^2+\lambda)^2} \left(\mathbf{u}_i^\top \mathbf{n}(t)\right)^2 \right]\end{aligned} \tag{4.19}$$

and

$$\begin{aligned}\varepsilon_{\mathbf{S}}(\lambda) = &\sum_f \sum_{\substack{i\geq M+1 \text{ or} \\ j\geq M+1}} \left|(\mathbf{v}_i \otimes \mathbf{v}_j)^\top \mathcal{S}^{\mathbf{x}}(f)\right|^2 \\ &+ \sum_f \sum_{i,j=1}^{M} \Big[\left(\frac{\sigma_i^2\sigma_j^2}{(\sigma_i^2+\lambda)(\sigma_j^2+\lambda)} - 1 \right)^2 \left|(\mathbf{v}_i \otimes \mathbf{v}_j)^\top \mathcal{S}^{\mathbf{x}}(f)\right|^2 \\ &+ \frac{\sigma_i^2\sigma_j^2}{(\sigma_i^2+\lambda)^2(\sigma_j^2+\lambda)^2} \left|(\mathbf{u}_i \otimes \mathbf{u}_j)^\top \mathcal{S}^{\mathbf{n}}(f)\right|^2 \\ &+ 2\left(\frac{\sigma_i^2\sigma_j^2}{(\sigma_i^2+\lambda)(\sigma_j^2+\lambda)} - 1 \right) \frac{\sigma_i\sigma_j}{(\sigma_i^2+\lambda)(\sigma_j^2+\lambda)} \mathrm{Re}\left(\overline{(\mathbf{v}_i \otimes \mathbf{v}_j)^\top \mathcal{S}^{\mathbf{x}}(f)} (\mathbf{u}_i \otimes \mathbf{u}_j)^\top \mathcal{S}^{\mathbf{n}}(f) \right) \Big]\end{aligned} \tag{4.20}$$

Again we assume that $\mathbf{X}(t)$ and $\mathbf{N}(t)$ are white-noise Gaussian processes with covariance matrices $\omega^2\mathbf{I}_N$ and $\alpha^2\mathbf{I}_M$. Under this assumption equations (4.19) and

(4.20) become

$$\varepsilon_{\mathbf{x}}(\lambda) = T(N-M)\omega^2 + T\omega^2 \sum_{i=1}^{M} \frac{\lambda^2}{(\sigma_i^2+\lambda)^2} + T\alpha^2 \sum_{i=1}^{M} \frac{\sigma_i^2}{(\sigma_i^2+\lambda)^2} \tag{4.21}$$

and

$$\begin{aligned}\varepsilon_{\mathbf{S}}(\lambda) = {} & L(N-M)\omega^4 + L\omega^4 \sum_{i=1}^{M} \left(\frac{\sigma_i^4}{(\sigma_i^2+\lambda)^2} - 1 \right)^2 + L\alpha^4 \sum_{i=1}^{M} \frac{\sigma_i^4}{(\sigma_i^2+\lambda)^4} \\ & + 2L\omega^2\alpha^2 \sum_{i=1}^{M} \left(\frac{\sigma_i^4}{(\sigma_i^2+\lambda)^2} - 1 \right) \frac{\sigma_i^2}{(\sigma_i^2+\lambda)^2} \quad ,\end{aligned} \tag{4.22}$$

where we notice that, as anticipated in the previous section, the fourth addend is negative; this fact suggests that, to the extent that the other terms are comparable to those in the corresponding expression for the tSVD (4.14), the reconstruction error generated by the Tikhonov method is smaller than the one generated by tSVD.

By differentiating equations (4.21) and (4.22) we have

$$\frac{d}{d\lambda}\varepsilon_{\mathbf{x}}(\lambda) = 2T\left(\omega^2\lambda - \alpha^2\right) \sum_{i=1}^{M} \frac{\sigma_i^2}{(\sigma_i^2+\lambda)^3} \tag{4.23}$$

and

$$\begin{aligned}\frac{d}{d\lambda}\varepsilon_{\mathbf{S}}(\lambda) = {} & 4L\omega^2 \sum_{i=1}^{M} \frac{\sigma_i^2}{(\sigma_i^2+\lambda)^5}(\alpha^2 + \sigma_i^2\omega^2) \\ & \cdot \left(\lambda + \sigma_i^2 + \sqrt{\sigma_i^4 + \sigma_i^2 \frac{\alpha^2}{\omega^2}} \right) \left(\lambda + \sigma_i^2 - \sqrt{\sigma_i^4 + \sigma_i^2 \frac{\alpha^2}{\omega^2}} \right) \quad .\end{aligned} \tag{4.24}$$

We are now able to prove the following theorem.

Theorem 4.9. *Let $x_\lambda(t)$ be the Tikhonov estimate as given by equation (2.16b), with regularisation parameter $\lambda \geq 0$; assume $\mathbf{X}(t)$ and $\mathbf{N}(t)$ to be white-noise Gaussian processes with covariance matrices $\omega^2\mathbf{I}_N$ and $\alpha^2\mathbf{I}_M$, respectively. Then*

$$\lambda_{\mathbf{x}}^* = \frac{\alpha^2}{\omega^2} \tag{4.25}$$

and

$$\lambda_{\mathbf{S}}^* < \frac{\lambda_{\mathbf{x}}^*}{2} \tag{4.26}$$

Proof. The first statement simply follows from equation (4.23) by observing that

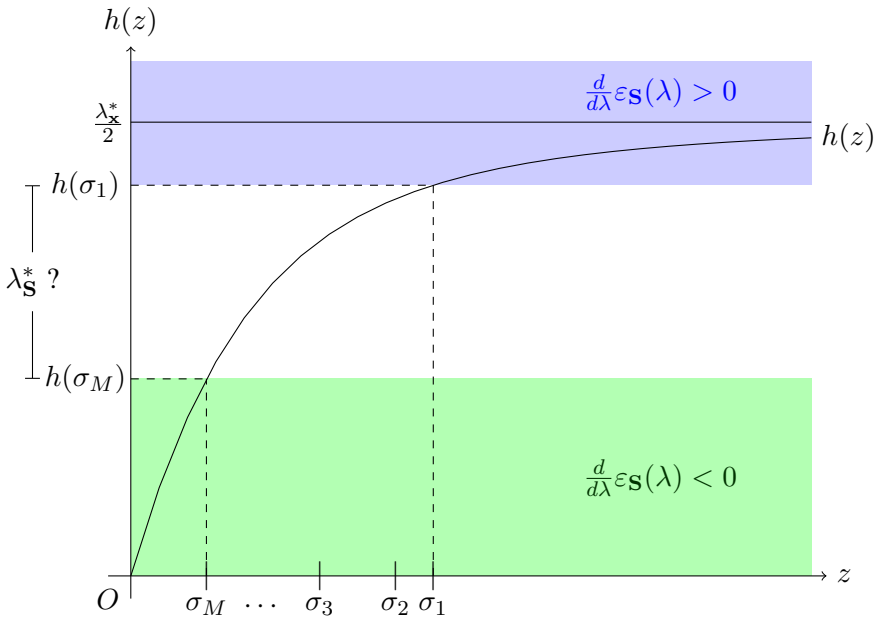

Figure 4.1: Plot of the function h(z) defined in the proof of Theorem 4.9. h(z) is related to the sign of the addends at the right hand side of (4.24). If $\lambda < h(\sigma_M)$ all the addends in (4.24) are negative therefore $\varepsilon_{\mathbf{S}}(\lambda)$ is decreasing (green area), whereas if $\lambda > h(\sigma_1)$ all the addends in (4.24) are positive therefore $\varepsilon_{\mathbf{S}}(\lambda)$ is increasing (blue area); it follows that the optimal regularisation parameter $\lambda^*_{\mathbf{S}}$ lies in the interval $[h(\sigma_M); h(\sigma_1)]$. Moreover, for $\lambda \geq \frac{\lambda^*_{\mathbf{x}}}{2}$ all the addends in (4.24) are positive regardless of the singular values, and therefore $\varepsilon_{\mathbf{S}}(\lambda)$ is increasing; this fact leads to the inequality $\lambda^*_{\mathbf{S}} < \frac{\lambda^*_{\mathbf{x}}}{2}$

$\frac{d}{d\lambda}\varepsilon_{\mathbf{x}}(\lambda) \geq 0$ if and only if $\lambda \geq \frac{\alpha^2}{\omega^2}$.
Instead, equation (4.24) implies that $\frac{d}{d\lambda}\varepsilon_{\mathbf{S}}(\lambda) > 0$ if

$$\lambda > -\sigma_i^2 + \sqrt{\sigma_i^4 + \sigma_i^2 \frac{\alpha^2}{\omega^2}} \quad . \tag{4.27}$$

Consider the function $h : [0, +\infty) \ni z \to -z^2 + \sqrt{z^4 + z^2 \frac{\alpha^2}{\omega^2}}$. As schematically shown in Figure 4.1, h is strictly increasing and bounded above by $\frac{\lambda^*_{\mathbf{x}}}{2} = \frac{\alpha^2}{2\omega^2}$. As a consequence, the condition (4.27) is satisfied if $\lambda \geq \frac{\lambda^*_{\mathbf{x}}}{2}$, that means $\varepsilon_{\mathbf{S}}(\lambda)$ is strictly increasing in $[\frac{\lambda^*_{\mathbf{x}}}{2}, +\infty)$ and thus inequality (4.26) holds. □

The main interest of Theorem 4.9 is that it provides a simple relationship between $\lambda^*_{\mathbf{S}}$ and $\lambda^*_{\mathbf{x}}$. However, expression (4.24) contains more information about the values of $\lambda^*_{\mathbf{S}}$, as stated in the following Theorem.

Theorem 4.10. *Under the same hypotheses of Theorem 4.9, the value of $\lambda^*_{\mathbf{S}}$ belongs to the interval $[h(\sigma_M), h(\sigma_1)]$, where $h(z) = -z^2 + \sqrt{z^4 + z^2 \frac{\alpha^2}{\omega^2}}$.*

Proof. As schematically shown in Figure 4.1, when $\lambda > h(\sigma_1)$, all the addends in (4.24) are positive and thus $\frac{d}{d\lambda}\varepsilon_{\mathbf{x}}(\lambda)$ is positive; on the other hand, when $\lambda < h(\sigma_M)$ the derivative $\frac{d}{d\lambda}\varepsilon_{\mathbf{x}}(\lambda)$ is negative as all the addends are negative. □

Remark 4.11. *Theorem 4.10 also gives information on the limiting behaviour of* $\lambda^*_{\mathbf{S}}$ *as* $\lambda^*_{\mathbf{x}} = \frac{\alpha^2}{\omega^2}$ *approaches very small or very large values. In the no-noise scenario, when* $\lambda^*_{\mathbf{x}} \sim 0$, $\lambda^*_{\mathbf{S}}$ *grows approximately linearly with* $\lambda^*_{\mathbf{x}}$*. The other boundary is however more interesting. Indeed, when* $\lambda^*_{\mathbf{x}} \to \infty$ *the extremes of the interval* $h(\sigma_1)$ *and* $h(\sigma_M)$ *grow with the same order of* $\sqrt{\lambda^*_{\mathbf{x}}}$*. Therefore, when noise gets larger not only* $\lambda^*_{\mathbf{S}}$ *is smaller than* $\lambda^*_{\mathbf{x}}$*, but it also grows more slowly.*

Remark 4.12. *Theorems 4.9 and 4.10 imply that, when regularisation is accomplished through the Tikhonov method,* $\lambda^*_{\mathbf{x}}$ *does not depend on the forward matrix* $\mathbf{G}$*, while* $\lambda^*_{\mathbf{S}}$ *does. The fact that* $\lambda^*_{\mathbf{x}}$ *does not depend on* $\mathbf{G}$ *may appear counter-intuitive: if the singular values grows, also the effective SNR of the data grow, and then the regularisation parameter should become smaller. In fact, the regularisation parameter does become smaller with respect to the data; in other words, this is the classic behaviour of the optimal regularisation parameter, where we are changing the SNR by increasing the strength of the exact signal, rather than decreasing the variance of the noise.*

Remark 4.13. *When* $M = N$ *and* $\sigma_1 = \cdots = \sigma_M = 1$*, the forward matrix* $\mathbf{G}$ *is orthogonal and the inverse problem in equation (3.19) is well-posed. Theorems 4.9 and 4.10 imply that* $\lambda^*_{\mathbf{S}}$ *and* $\lambda^*_{\mathbf{x}}$ *are different also under these conditions, as*

$$h(\sigma_M) = h(\sigma_1) = -1 + \sqrt{1 + \frac{\alpha^2}{\omega^2}} < \frac{\alpha^2}{\omega^2}$$

Although unrealistic, this case is of particular interest in M/EEG functional connectivity because it corresponds to the ideal case where there is no cross-talk or source-leakage between sources (Hauk et al., 2019).

Indeed, in this case the resolution matrix is proportional to the identity matrix ($\mathbf{R}_\lambda = (1+\lambda)^{-1}\,\mathbf{I}_N$*), i.e. the estimate at one location is not influenced by neural activity at different locations. Our result shows that also in this ideal case the optimal values of the regularisation parameters are different.*

4.4 Beyond the two-step approach: Filter factor for a direct estimation of $\mathbf{S}^{\mathbf{x}}(f)$ from $\mathbf{S}^{\mathbf{y}}(f)$

As an alternative to the two-step approach described so far, one may directly estimate the cross-power spectrum of the unknown $\mathbf{S}^{\mathbf{x}}(f)$ from that of the data

$\mathbf{S}^{\mathbf{y}}(f)$. Indeed, from equation (3.19) and from the linearity of the Fourier Transform it follows

$$\mathcal{S}^{\mathbf{y}}(f) = (\mathbf{G} \otimes \mathbf{G})\mathcal{S}^{\mathbf{x}}(f) + \mathcal{S}^{\mathbf{n}}(f) \quad , \tag{4.28}$$

which describes a linear inverse problem.

Analogously to what we did in the previous sections for the forward operator $\mathbf{G}$, we can introduce the SVD of the forward operator $\mathbf{G} \otimes \mathbf{G} = (\mathbf{U} \otimes \mathbf{U})(\mathbf{\Sigma} \otimes \mathbf{\Sigma})(\mathbf{V} \otimes \mathbf{V})^{\top}$, up to reordering the elements of $\mathbf{\Sigma} \otimes \mathbf{\Sigma}$ and the corresponding columns of $\mathbf{U} \otimes \mathbf{U}$ and $\mathbf{V} \otimes \mathbf{V}$. We can then express a *one-step* regularised estimate of the cross-spectrum in terms of the SVD and of the filter factors

$$\mathcal{S}^{\mathbf{x}}_{\lambda}(f) = (\mathbf{V} \otimes \mathbf{V})\, \widetilde{\mathbf{\Phi}}(\lambda)\, (\mathbf{\Sigma} \otimes \mathbf{\Sigma})^{\dagger}\, (\mathbf{U} \otimes \mathbf{U})^{\top}\, \mathcal{S}^{\mathbf{y}}(f) \tag{4.29}$$

$$= \sum_{i,j}^{M} \widetilde{\varphi}_{i,j}(\lambda) \frac{(\mathbf{u}_i \otimes \mathbf{u}_j)^{\top}\, \mathcal{S}^{\mathbf{y}}(f)}{\sigma_i \sigma_j} (\mathbf{v}_i \otimes \mathbf{v}_j) \quad . \tag{4.30}$$

In particular, if Tikhonov regularisation is employed, the filter factors read

$$\widetilde{\varphi}_{i,j}(\lambda) = \frac{\sigma_i^2 \sigma_j^2}{\sigma_i^2 \sigma_j^2 + \lambda} \tag{4.31}$$

while in tSVD the components such that the product $\sigma_i \sigma_j$ is below the threshold defined by λ are filtered out. Instead, in the classic two-step approach the filter factors for the estimated cross-spectrum are simply given by the product of the filter factors for the estimated source time-courses, that means each of the singular value σ_i and σ_j is individually filtered, instead of their product $\sigma_i \sigma_j$. Indeed, the cross-spectrum of the regularised estimate $\mathbf{x}_{\lambda}(t)$ in equation (2.16a) is

$$\mathcal{S}^{\mathbf{x}_{\lambda}}(f) = (\mathbf{V} \otimes \mathbf{V}) \left(\mathbf{\Phi}\mathbf{\Sigma}^{\dagger} \otimes \mathbf{\Phi}\mathbf{\Sigma}^{\dagger} \right) (\mathbf{U} \otimes \mathbf{U})^{\top}\, \mathcal{S}^{\mathbf{y}}(f) \tag{4.32}$$

$$= \sum_{i,j}^{M} \varphi_i(\lambda)\varphi_j(\lambda) \frac{(\mathbf{u}_i \otimes \mathbf{u}_j)^{\top}\, \mathcal{S}^{\mathbf{y}}(f)}{\sigma_i \sigma_j} (\mathbf{v}_i \otimes \mathbf{v}_j) \quad . \tag{4.33}$$

As a comparison in Figures 4.2 and 4.3 we plotted the filter factors $\widetilde{\varphi}_{i,j}(\lambda)$ and $\varphi_i(\lambda)\varphi_j(\lambda)$ for the tSVD and Tikhonov method. The forward matrix was obtained by randomly selecting (uniform sampling) $M = 20$ sensors and $N = 25$ source locations from a standard MEG forward operator based on a realistic, three-layer boundary element method (BEM) head model, publicly available within the mne-python software (Gramfort et al., 2014). Such selection of a subset of rows and columns allows to produce more readable plots than those obtained by using the whole leadfield, that would be qualitatively similar but with a denser cloud of points. The specific choice of source and sensor locations does not modify the re-

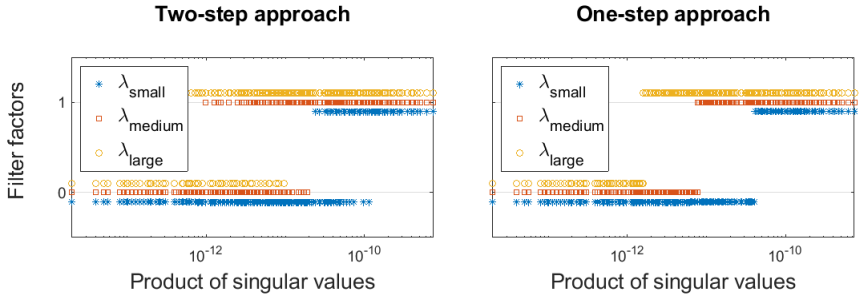

Figure 4.2: Filter factors for the tSVD method. On the x-axis the product of the singular values $\sigma_i\sigma_j$, on the y-axis the corresponding values of the filter factors $\varphi_i(\lambda)\varphi_j(\lambda)$ for the two-step approach (left) and $\widetilde{\varphi}_{i,j}(\lambda)$ for the one-step approach (right). The three different colours correspond to three different values of the regularisation parameter, as illustrated in the legend. Please notice that the filter factors for tSVD are either zero or one, but different colours are plotted at slightly different levels for the sake of clarity.

sults: we tried several random configurations and they all provided similar plots. Figure 4.2 and 4.3 highlight the potential advantages of the one-step approach over the two-step approach. In the case of tSVD, the filter factors of the two-step approach are zero whenever either $i < \lambda$ or $j < \lambda$, which implies a jittering behaviour when plotted as a function of the product $\sigma_i\sigma_j$. In the one-step approach this issue is not present, because filtering is applied directly to the product of the singular values. In the case of the Tikhonov method we observe a similar behaviour, where in the one-step approach the filter factors increase smoothly when the product $\sigma_i\sigma_j$ increases, while in the two-step approach also higher values of such product may be severely filtered because of the effect of the regularisation parameter on the individual singular values.

4.5 A numerical simulation

In this section we use a numerical simulation to show what happens when the rather restrictive assumption of a white Gaussian signal, that was needed to prove the results in Section 4.3, no longer holds. We exploit the same simulation to show that in this case the one-step approach described by equation (4.29) enables to estimate the cross-power spectrum with a lower reconstruction error. We remark, however, that this simulation is just an example and is not meant to be a full validation.

Following Hincapié et al. (Hincapié et al., 2016), we simulated two interacting oscillatory sources. The first source was placed in the temporal lobe of the left hemisphere, the second source was placed in the occipital lobe of the right hemisphere at a distance of 11.8 cm from the first one. The time courses of the two

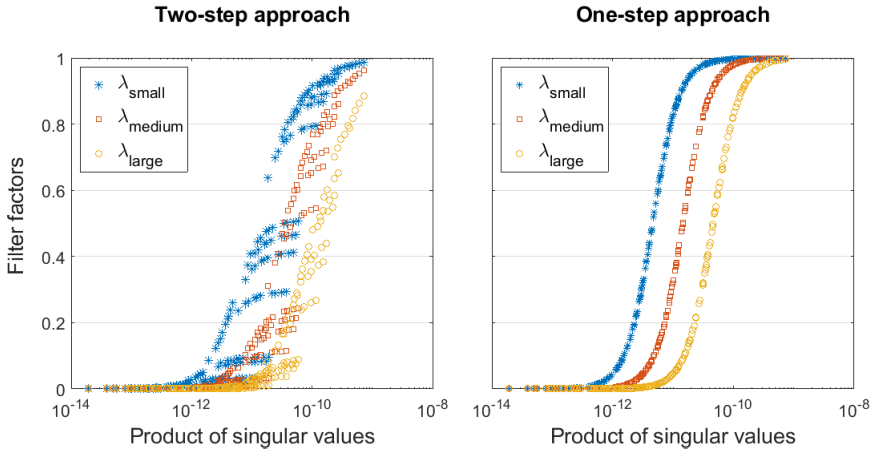

Figure 4.3: Filter factors for the Tikhonov method. On the x-axis the product of the singular values $\sigma_i\sigma_j$, on the y-axis the corresponding values of the filter factors $\varphi_i(\lambda)\varphi_j(\lambda)$ for the two-step approach (left) and $\widetilde{\varphi}_{i,j}(\lambda)$ for the one-step approach (right). The three different colours correspond to three different values of the regularisation parameter, as illustrated in the legend.

sources were simulated with a coherence level of 0.4, as follows: first the base frequency was set to 12 Hz for both sources; then the instantaneous frequency was randomly drawn independently around the base frequency, causing fluctuations in the phase relationship between the two signals. A total number of $T = 30,000$ time points was used. The process was repeated until the desired level of coherence (0.4) was attained.

Source time courses were then projected to the sensor level through a forward operator obtained by downsampling the same MEG leadfield used in the previous section; the final forward operator has $M = 102$ sensors (magnetometers) and $N = 274$ source points guaranteeing a uniform coverage of the brain. With the exception of the two oscillatory sources, all other source time courses were set to zero. White Gaussian noise was added at the sensor level to reach five different values of Signal-to-Noise Ratio (SNR) defined as

$$\text{SNR} = 10\log_{10}\left(\frac{\sum_{t=0}^{T-1}||\mathbf{G}\mathbf{x}(t)||^2}{\sum_{t=0}^{T-1}||\mathbf{n}(t)||^2}\right) \quad , \tag{4.34}$$

where $\mathbf{n}(t) = \sigma\tilde{\mathbf{n}}(t)$, being $\tilde{\mathbf{n}}(t) \sim \mathcal{N}(\mathbf{0}, \mathbf{I}_M)$, and σ was defined in order to attain the desired SNR. The values of SNR were evenly selected in the range $[-10\text{dB}, 10\text{dB}]$.

For each simulated data we numerically computed the two optimal parameters $\lambda^*_{\mathbf{x}}$ and $\lambda^*_{\mathbf{S}}$, as defined in Definition 4.1, for tSVD and for the Tikhonov method. The optimal values are reported in Table 4.1. For both methods, optimal recon-

struction of the cross-power spectrum requires less regularisation than optimal reconstruction of the signal. For tSVD this result is qualitatively different from the white noise case, where we proved that the two optimal parameters are equal; for the Tikhonov method, on the other hand, the optimal values obey the same inequality, and the ratio between the optimal values is very similar to the one reported in (Hincapié et al., 2016). This is expected, since the numerical simulation here was constructed following the same scheme.

Finally, we numerically computed the optimal regularisation parameter for the one-step approach defined as

$$\tilde{\lambda}^*_{\mathbf{S}} = \arg\min_{\lambda} \tilde{\varepsilon}_{\mathbf{S}}(\lambda) \quad \text{with} \quad \tilde{\varepsilon}_{\mathbf{S}}(\lambda) = \sum_f \|\mathbf{S}^{\mathbf{x}}_{\lambda}(f) - \mathbf{S}^{\mathbf{x}}(f)\|^2_F \tag{4.35}$$

and we compared the reconstruction error reached by the one-step and the two-step approach when the corresponding optimal regularisation parameters are employed, i.e. $\varepsilon_{\mathbf{S}}(\lambda^*_{\mathbf{S}})$ and $\tilde{\varepsilon}_{\mathbf{S}}(\tilde{\lambda}^*_{\mathbf{S}})$. Figure 4.4 shows the reconstruction errors for the cross-power spectrum for tSVD and Tikhonov method for both the two-step and the one-step approach as a function of the SNR. The line corresponding to the two-step approach is always above the one corresponding to the one-step approach, showing that the latter provides a better estimation for the cross-power spectrum.

	tSVD		Tikhonov		
SNR	$\lambda^*_{\mathbf{x}}$	$\lambda^*_{\mathbf{S}}$	$\lambda^*_{\mathbf{x}}$	$\lambda^*_{\mathbf{S}}$	$\lambda^*_{\mathbf{S}}/\lambda^*_{\mathbf{x}}$
-10	7	25	110	$9.36 \cdot 10^{-1}$	$8.5 \cdot 10^{-3}$
-5	8	35	35.0	$2.93 \cdot 10^{-1}$	$8.4 \cdot 10^{-3}$
0	8	45	9.86	$9.53 \cdot 10^{-2}$	$9.7 \cdot 10^{-3}$
5	25	53	3.15	$3.00 \cdot 10^{-2}$	$9.5 \cdot 10^{-3}$
10	28	69	1.12	$9.40 \cdot 10^{-3}$	$8.4 \cdot 10^{-3}$

Table 4.1: $\lambda^*_{\mathbf{x}}$ and $\lambda^*_{\mathbf{S}}$ for the different values of SNR. In tSVD, the number of retained SVD components for the reconstruction of the cross-power spectrum is always higher than for the time-series reconstruction, showing that less regularisation is needed for the first one. For the Tikhonov method, $\lambda^*_{\mathbf{S}}$ is always smaller than $\lambda^*_{\mathbf{x}}$, showing that less regularisation is needed for the cross-power spectrum reconstruction.

4.6 Discussion

In this chapter we presented the results published in (Vallarino et al., 2020). Motivated by an analysis pipeline which is largely used for connectivity studies in the MEEG community, we have considered the problem of whether, in a two-step

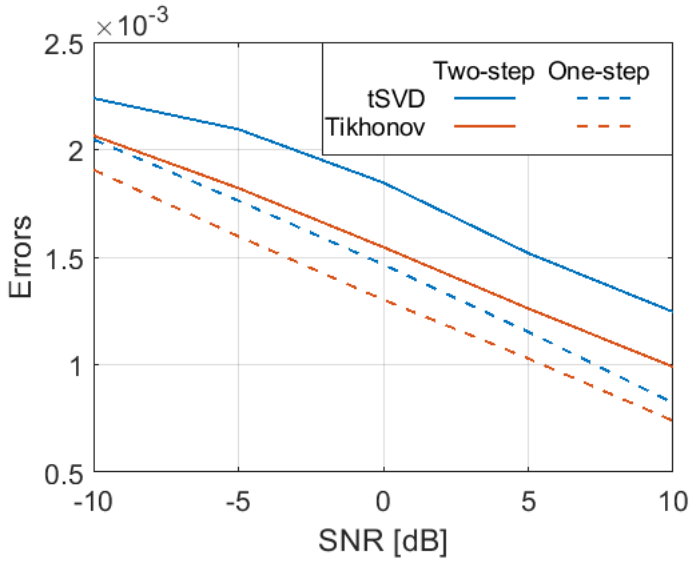

Figure 4.4: Reconstruction errors for the cross-spectrum reconstruction as a function of the SNR for tSVD (blue) and for the Tikhonov method (red), for the two-step (solid line) and for the one-step (dotted line) approach. For both methods the one-step approach provides a better reconstruction of the cross-power spectrum.

approach to the reconstruction of the cross-power spectrum of an unobservable signal, one should set the regularisation parameter differently than what one would do for the reconstruction of the signal itself.

First, making use of filter factor analysis, we obtained an explicit expression for the reconstruction error for the cross-power spectrum under the two-step approach. This formula is the analogous of the well-known formula for the reconstruction error in linear inverse problems, and holds in general. Then, under additional hypotheses of a white Gaussian signal and white Gaussian noise, we proved that the optimal values coincide for tSVD, while in the Tikhonov method the optimal value for the cross-power spectrum is at most half the optimal value for the signal, thus proving also that the answer actually depends on the inverse method. We speculate that such difference may be partly due to the fact that, with white Gaussian signals, the error in estimating the cross-power spectrum involves the square of the filter factors; for tSVD, where filter factors can only be 0 or 1, the components corresponding to the largest singular values will possibly be weighted by a 1, and when the filter is squared for the cross-spectrum, the largest component will still be weighted by a 1. For Tikhonov, where filter factors range in the interval $[0, 1]$, the components corresponding to the largest singular values will be weighted by a factor lower than one, and when such factor is squared it becomes even smaller; therefore, in order not to filter excessively the largest components, a smaller regularisation parameter is needed.

The results of Section 4.3 are in line with the results of (Hincapié et al., 2016), which showed empirically that the optimal estimate of connectivity is obtained with a regularisation parameter smaller than the one providing the optimal estimate of the power spectrum, i.e. of the signal strength. Quantitatively, the recommendation in (Hincapié et al., 2016) was to use a parameter two orders of magnitude lower, while our main theorem for the Tikhonov method guarantees $\lambda^*_{\mathbf{S}} < \lambda^*_{\mathbf{x}}/2$.

Theorems 4.7, 4.9 and 4.10 have been obtained under the somewhat unrealistic assumption that the signal is a white-noise Gaussian process. While this is an important limitation with respect to the applications, preliminary numerical results indicate that the optimal value for the cross-spectrum is further reduced by the presence of a temporal structure in the signal: in the numerical simulation in Section 6 we observed that, with interacting, oscillatory signals, the optimal values in tSVD no longer coincide, and $\lambda^*_{\mathbf{S}}$ in the Tikhonov method is approximately two orders of magnitude smaller than $\lambda^*_{\mathbf{X}}$, in line with the mentioned results in (Hincapié et al., 2016). In any case, in the next chapters we will see the effect of a more plausible temporal structure of the input waveforms.

In addition, our results so far only concern the cross-power spectrum; in Chapter 6 we will present some preliminary results on the impact of the regularisation parameter on the estimated value of connectivity measures, such as Imaginary part of Coherency, Phase Locking Value and Phase Lag Index.

Finally, as we point out in Section 4.4, our results suggest that the two-step approach to estimation of the cross-power spectrum, and more in general of brain functional connectivity, might be sub-optimal. This idea is in line with literature on the topic (Kiebel et al., 2008; Cheung et al., 2010; Fukushima et al., 2015; Ossadtchi et al., 2018; Subramaniyam et al., 2017; Tronarp et al., 2018). Indeed, by looking at the filter factors obtained by the two-step approach, and comparing them to the filter factors one would get with a one-step approach to estimate the cross-power spectrum, we expect a better behaviour for this second option. Newly presented methods such as PSIICOS (Ossadtchi et al., 2018) present one-step approaches to the estimation of connectivity that benefit from this fact. In Chapter 7 a deeper analysis of a possible one-step approach and its potential will be presented.

Chapter 5

The impact of spectral complexity on the two-step estimation of the cross-power spectrum

The work presented in this chapter is the natural prosecution of the previous one. Indeed, in Chapter 4 we introduced the issue of optimally choosing the regularisation parameter when estimating the cross-power spectrum from MEG data in a two-step approach. We presented some analytical results that support the findings presented in (Hincapié et al., 2016), and we validated them through a simulation. However, in order to prove those results we assumed few properties that are not realistically satisfied by neural activity. In the current chapter we focus on validating the results of the previous chapter through more realistic numerical simulations. In addition we investigate how the spectral properties of the neural activity influence the parameter providing the best possible estimate of the cross-power spectrum.

Specifically, in this chapter we present the results published in (Vallarino et al., 2021b). Differently from Chapter 4 we only consider the Tikhonov method (better known as Minimum Norm Estimation (MNE) in the MEG world (Hämäläinen and Ilmoniemi, 1994a)) as it is one of the most commonly used inverse methods in connectivity studies (Anzolin et al., 2019; Mahjoory et al., 2017; Hincapié et al., 2017); we study the interplay between the regularisation parameter providing the reconstructed neural time series minimising the relative error in ℓ_2-norm, and the one that allows the optimal estimate of the cross-power spectrum according to the normalised Frobenius norm. The conceptual motivation of this problem is illustrated in Figure 5.1, which tentatively sketches the result of some investigations in MEG-based connectivity research, i.e. that the regularisation parameter leading to the optimal estimate of the neural activity may not lead to the optimal estimate of the cross-power spectrum and, vice versa (Hincapié et al., 2016; Vallarino et al.,

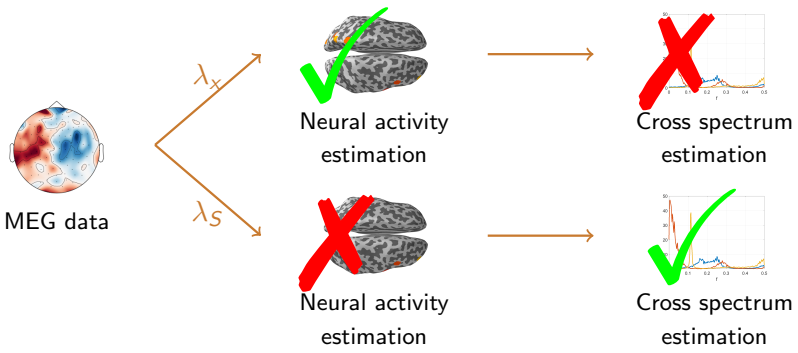

Figure 5.1: Schematic representation of the differences between the regularisation parameter providing the best time series estimate ($\lambda_{\mathbf{x}}$) and the one providing the best cross-power spectrum estimate ($\lambda_{\mathbf{S}}$). The first one provides an optimal reconstruction of the neural activity, but it may not lead to an optimal estimate of the cross-power spectrum; vice versa $\lambda_{\mathbf{S}}$ provides an optimal reconstruction of the cross-power spectrum at the expense of a sub-optimal estimate of the time series.

2020).

This chapter focuses on an analysis of the impact of spectral complexity of the actual neural signal on the value of the two regularisation parameters. Specifically, we simulated synthetic MEG signals and discuss how the optimal parameter for the reconstruction of the cross-power spectrum depends on its signal-to-noise ratio and how this latter quantity is related to the spectral richness of the neural sources. To this aim, we considered a simulation setting in which the signal is modelled as a multivariate autoregressive process.

The chapter is organised as is as follows. Section 5.1 introduces the problem in a formal way. Section 5.2 describes how the synthetic data are simulated and analysed. Section 5.3 presents the results of the analysis. Our conclusions are offered in Section 5.4.

5.1 Definition of the problem

Let us consider the MEEG problem (3.19)

$$\mathbf{y}(t) = \mathbf{G}\mathbf{x}(t) + \mathbf{n}(t),$$

which can be interpreted as a realisation of the linear model

$$\mathbf{Y}(t) = \mathbf{G}\mathbf{X}(t) + \mathbf{N}(t), \tag{5.1}$$

being $\mathbf{y}(t) \in \mathbb{R}^M$, $\mathbf{x}(t) \in \mathbb{R}^N$ and $\mathbf{n}(t) \in \mathbb{R}^M$ realisations of the multivariate stochastic processes $\mathbf{Y}(t)$, $\mathbf{X}(t)$ and $\mathbf{N}(t)$, and $\mathbf{G} \in \mathbb{R}^{M\times N}$ a leadfield matrix.

$\mathbf{N}(t)$ is the measurement noise process, which is assumed to be a white Gaussian process with zero mean and covariance matrix $\alpha^2\mathbf{I}$, i.e. $\mathbf{N}(t) \sim \mathcal{N}(0, \alpha^2\mathbf{I})$, independent from $\mathbf{X}(t)$.

We are interested in reconstructing the cross-power spectrum of $\mathbf{X}(t)$, as defined in Definition 1.12, and we exploit Welch's method to its estimation. That is, recalling Section 1.3.1,

$$\mathbf{S}^{\mathbf{x}}(f) = \frac{1}{PW}\sum_{p=1}^{P}\hat{\mathbf{x}}^p(f)\hat{\mathbf{x}}^p(f)^H, \qquad f = 0, \dots, L-1, \tag{5.2}$$

being $\hat{\mathbf{x}}^p(f) = \sum_{t=0}^{L-1}\mathbf{x}^p(t)w(t)e^{-\frac{2\pi i t f}{L}}$ and $W = \sum_{t=0}^{L-1}w(t)^2$.

It is often the case that the data reaches high dimension, and visual inspection of the cross-power spectrum is not doable. In such cases a metric that describes the spectral properties of the signals would be useful. Here we use the spectral complexity coefficient, defined as follows.

Definition 5.1. Given a realisation $\mathbf{x}(t)$ of the process $\mathbf{X}(t)$, and the corresponding cross-power spectrum $\mathbf{S}^{\mathbf{x}}(f)$, we define the spectral complexity coefficient as the average of the elements of the upper triangular part of the matrix obtained by computing the squared ℓ_2-norm over the frequencies of $\mathbf{S}^{\mathbf{x}}_{j,k}(f)$, $j, k = 1, \dots, N$, that is

$$c = \frac{2}{N(N+1)}\sum_{j=1}^{N}\sum_{k=j}^{N}\sum_{f}\left|S^{\mathbf{x}}_{j,k}(f)\right|^2. \tag{5.3}$$

The spectral complexity coefficient assumes small values if the elements of the cross-power spectrum are flat, that is when time series do not present any periodic trend and no dependencies among the pairs of time series are present. On the contrary, it assumes large values if the elements of the cross-power spectrum are peaked, that is when time series present periodic trends and complex relations among them. Finally, we observe that in Definition 5.1 only the elements on the upper triangular part of $\mathbf{S}^{\mathbf{x}}(f)$ are considered because $\mathbf{S}^{\mathbf{x}}(f)$ is Hermitian.

Let us get back to equation (3.19). Further than an estimate of the hidden data $\mathbf{x}(t)$, an estimate of the cross-power spectrum can be obtained from $\mathbf{y}(t)$. Such estimate can be achieved through a two-step process, as described in Section 3.7:

i. First, a regularised estimate $\mathbf{x}_\lambda(t)$ of $\mathbf{x}(t)$ is obtained by solving the inverse problem associated with equation (3.19). Here we consider the Tikhonov

regularised solution (Tikhonov et al., 2013) of the problem which is defined as

$$\mathbf{x}_\lambda(t) = \arg\min_{\mathbf{x}(t)} \left\{ \|\mathbf{G}\mathbf{x}(t) - \mathbf{y}(t)\|_2^2 + \lambda \|\mathbf{x}(t)\|_2^2 \right\}; \tag{5.4}$$

where λ is a proper regularisation parameter and $\|\cdot\|_2$ is the ℓ_2-norm.

ii. Then, the corresponding estimate of the cross-power spectrum $\mathbf{S}^{\mathbf{x}_\lambda}(f)$ is computed from the reconstructed time series using Welch's method.

Remark 5.2. *In many applied fields, Tikhonov regularisation with an ℓ_2 penalty term has been outdated by more modern techniques that use sparsity–inducing penalisation terms such as ℓ_1 or ℓ_p with $0 < p < 1$. Indeed, also in the MEEG literature there has been considerable effort in developing ℓ_1 solutions (Matsuura and Okabe, 1995; Uutela et al., 1999), and mixed norm solutions (Gramfort et al., 2012); both these approaches have proved to provide superior performances in terms of localisation of neural activity. However, these newer methods are seldom used in connectivity studies, for good reasons: ℓ_1 solutions computed independently at each time point produce extremely jittering reconstructions, resulting in highly sparse time courses that are not suitable for computing connectivity metrics. Mixed norms, that have been developed precisely to overcome this jittering problem, are computationally very expensive, and this actually prevents their use with the large data sets typically involved in connectivity studies.*

As we said in Section 3.7, when applying the described two-step process, the regularisation parameter λ in equation (5.4) has to be set for the computation of $\mathbf{x}_\lambda(t)$. Thus, the problem naturally arises of the choice of such parameter, which can be set in order to optimally reconstruct either $\mathbf{x}_\lambda(t)$ or $\mathbf{S}^{\mathbf{x}_\lambda}(f)$. We define optimality through the minimisation of the normalised norm of the discrepancy between the true and the reconstructed time series and cross-power spectra as follows.

Definition 5.3. Given the regularised solution (5.4) and the cross-power spectrum (5.2), we define the optimal regularisation parameter for the reconstruction of $\mathbf{x}(t)$ as

$$\lambda^*_{\mathbf{x}} = \arg\min_\lambda \varepsilon_{\mathbf{x}}(\lambda) \quad \text{with} \quad \varepsilon_{\mathbf{x}}(\lambda) = \frac{\sum_t \|\mathbf{x}_\lambda(t) - \mathbf{x}(t)\|_2^2}{\sum_t \|\mathbf{x}_\lambda(t)\|_2^2 + \sum_t \|\mathbf{x}(t)\|_2^2} \quad ; \tag{5.5}$$

and the optimal parameter for the reconstruction of $\mathbf{S}^{\mathbf{x}}(f)$ as

$$\lambda^*_{\mathbf{S}} = \arg\min_\lambda \varepsilon_{\mathbf{S}}(\lambda) \quad \text{with} \quad \varepsilon_{\mathbf{S}}(\lambda) = \frac{\sum_f \|\mathbf{S}^{\mathbf{x}_\lambda}(f) - \mathbf{S}^{\mathbf{x}}(f)\|_F^2}{\sum_f \|\mathbf{S}^{\mathbf{x}_\lambda}(f)\|_F^2 + \sum_f \|\mathbf{S}^{\mathbf{x}}(f)\|_F^2} \quad ; \tag{5.6}$$

where $\|\cdot\|_F$ is the Frobenius norm; $\varepsilon_{\mathbf{x}}(\lambda)$ and $\varepsilon_{\mathbf{S}}(\lambda)$ will be called reconstruction errors.

The reconstruction errors range from 0 to 1 and penalise both a too small and a too large value of λ. In fact, they assume their maximum value when either λ is very high and thus $\mathbf{x}_\lambda(t)$ is negligible with respect to $\mathbf{x}(t)$, or when λ is too small and thus, vice versa, $\mathbf{x}(t)$ is negligible with respect to $\mathbf{x}_\lambda(t)$. This definition may appear overly complex compared to, e.g., a mere ℓ_2-norm of the difference; however, in the presence of sparse data where only few time series are non-zero, the simple ℓ_2-norm would prefer a very high regularisation parameter in order to minimise the error on the null time series, at the expense of the error on the non-zero ones; our definition aims to cope with this limitation of the ℓ_2-norm. A similar definition has been introduced in (Chella et al., 2019).

In experimental contexts, where $\mathbf{x}(t)$ is not known, the choice of the optimal regularisation parameter is crucial. This matter is widely discussed in literature (Thompson et al., 1991; Hanke and Hansen, 1993; Hansen, 1998; Vogel, 2002), and many criteria have been proposed. Such criteria apply to equation (3.19) and can be used to set the regularisation parameter $\lambda_{\mathbf{x}}$. A possibility is to set the regularisation parameter as a function of the signal-to-noise ratio (SNR), which describes the level of the desired signal with respect to that of the measurement noise; for equation (5.1) the SNR is defined as follows.

Definition 5.4. Consider the linear model (5.1). We define the signal-to-noise ratio of $\mathbf{X}(t)$ related to such model as

$$\mathrm{SNR}^{\mathbf{X}} = 10\log_{10}\left(\frac{\sum_t \|\mathbf{G}\mathbf{X}(t)\|_2^2}{\sum_t \|\mathbf{N}(t)\|_2^2}\right). \tag{5.7}$$

To the best of our knowledge, the choice of the optimal regularisation parameter for the reconstruction of the cross-power spectrum has never been related to the signal-to-noise ratio. This relation will be presented in Section 5.3; however we first need to relate the cross-power spectrum of the unknown $\mathbf{S}^{\mathbf{X}}(f)$ with that of the data $\mathbf{S}^{\mathbf{Y}}(f)$.

By computing the cross-power spectrum of both sides of equation (5.1) and from the linearity of the Fourier transform it follows that

$$\mathbf{S}^{\mathbf{Y}}(f) = \mathbf{G}\mathbf{S}^{\mathbf{X}}(f)\mathbf{G}^\top + \mathbf{S}^{\mathbf{N}}(f), \tag{5.8}$$

where the mixed terms $\mathbf{S}^{\mathbf{XN}}(f)$ and $\mathbf{S}^{\mathbf{NX}}(f)$ are negligible thanks to the independence between $\mathbf{X}(t)$ and $\mathbf{N}(t)$. Just like for equation (5.1), we can define the signal-to-noise ratio for equation (5.8) as follows.

Definition 5.5. Consider the linear model (5.8). We define the signal-to-noise ratio of $\mathbf{S}^{\mathbf{X}}(f)$ related to such model as

$$\mathrm{SNR}^{\mathbf{S}} = 10 \log_{10} \left(\frac{\sum_f \left\| \mathbf{G}\mathbf{S}^{\mathbf{X}}(f)\mathbf{G}^\top \right\|_F^2}{\sum_f \|\mathbf{S}^{\mathbf{N}}(f)\|_F^2} \right). \tag{5.9}$$

This definition is in line with the definition of $\mathrm{SNR}^{\mathbf{X}}$ for the signal, the main difference being in the use of the Frobenius norm rather than the ℓ_2-norm, motivated by the fact that we are working with matrices rather than vectors.

5.2 Generation and analysis pipeline of the MEG simulated data

In this section we will describe the numerical simulation that led to the main results of our study. First we describe how we generated the data and, then, we describe the inverse model and how we numerically computed the optimal regularisation parameters.

5.2.1 Data generation

We simulated sensor level MEG recordings by exploiting the linear model (3.19), thus we needed to set a leadfield matrix, $\mathbf{G}$, and to simulate brain activity, $\mathbf{x}(t)$, and measurement noise, $\mathbf{n}(t)$.

As for the leadfield matrix, we used the matrix available in the sample data set of MNE Python (Gramfort et al., 2014). We selected magnetometers and set a fixed orientation. For computational reasons, the available source space, containing 1884 sources, was uniformly down-sampled to obtain 274 sources. Thus, our model has $M = 102$ sensors and $N = 274$ dipole sources.

For the generation of brain activity, we simulated $N_{mod} = 10$ pairs of active sources, $(z_1(t), z_2(t))^\top$, with unidirectional coupling from the first to the second; their time series follow a multivariate autoregressive (MVAR) model of order $P = 5$

$$\begin{pmatrix} z_1(t) \\ z_2(t) \end{pmatrix} = \sum_{k=1}^{P} \begin{pmatrix} a_{1,1}(k) & 0 \\ a_{2,1}(k) & a_{2,2}(k) \end{pmatrix} \begin{pmatrix} z_1(t-k) \\ z_2(t-k) \end{pmatrix} + \begin{pmatrix} \varepsilon_1(t) \\ \varepsilon_2(t) \end{pmatrix}, \; t = P, \ldots, T. \tag{5.10}$$

The non-zero elements $a_{i,j}(k)$ of the coefficient matrices were drawn from a normal distribution of zero mean and standard deviation γ, and T=10000. We retained only coefficient matrices providing (i) a stable MVAR model (Lütkepohl, 2005)

and (ii) pairs of signals $(z_1(t), z_2(t))^\top$ such that the ℓ_2-norm of the strongest one was less than 3 times the ℓ_2-norm of the weakest one. In order to obtain time series with different spectral complexity coefficients we set γ to N_{mod} different values randomly drawn in the interval $[0.1, 1]$. The values of the spectral complexity coefficient of the N_{mod} simulated time-series are reported in Table 5.1. Finally, the resulting time series $(z_1(t), z_2(t))^\top$ were normalised by the mean of their standard deviations over time, so that pairs of time series drawn from different models had similar magnitude. Figure 5.2 shows a sample of the the cross-power spectra among the simulated pairs of time series. The figure shows that for increasing values of the spectral complexity coefficient the cross-power spectrum of the corresponding time series becomes more peaked. Each pair of simulated time series was then assigned to $N_{loc} = 20$ pairs of point like sources randomly chosen in the source space, so that the ratio of the norms of the corresponding columns of the leadfield matrix was close to one, i.e. they had similar intensity at sensor level, and their distance was grater than 7 cm. The remaining $N - 2$ sources were set to have null activity.

Source space activity was then projected to sensor level by multiplying the simulated source activity by the leadfield matrix and white Gaussian noise, $\mathbf{n}(t)$, was added to obtain $N_{snr} = 6$ levels of $\text{SNR}^{\mathbf{X}}$ evenly spaced in the interval $[-20\text{dB}, 5\text{dB}]$.

Summarising, we generated $N_{mod} \cdot N_{loc} \cdot N_{snr} = 1200$ different sensor level configurations. The green box in Figure 5.3 shows a visual representation of the simulation pipeline.

Table 5.1: The table reports the values of the spectral complexity coefficients, c_j, associated with each simulated MVAR model, m_j, $j = 1, \ldots, N_{mod}$.

Model	1	2	3	4	5	6	7	8	9	10
Spectral complexity coefficient	1.41	1.96	2.14	3.10	3.44	4.17	4.64	5.67	6.69	8.67

5.2.2 Inverse model

Source space time series were reconstructed using Tikhonov method, i.e minimum norm estimate (MNE) (Hämäläinen and Ilmoniemi, 1994a). For each combination of source time series, source locations and $\text{SNR}^{\mathbf{X}}$ level we computed the optimal regularisation parameters $\lambda^*_{\mathbf{X}}$ and $\lambda^*_{\mathbf{S}}$ by minimising the reconstruction errors $\varepsilon_{\mathbf{X}}(\lambda)$ and $\varepsilon_{\mathbf{S}}(\lambda)$, defined in Definition 5.3. The minimisation procedure was achieved by using the Matlab built in function `fminsearch` that implements an iterative procedure based on the simplex method developed by Lagarias and col-

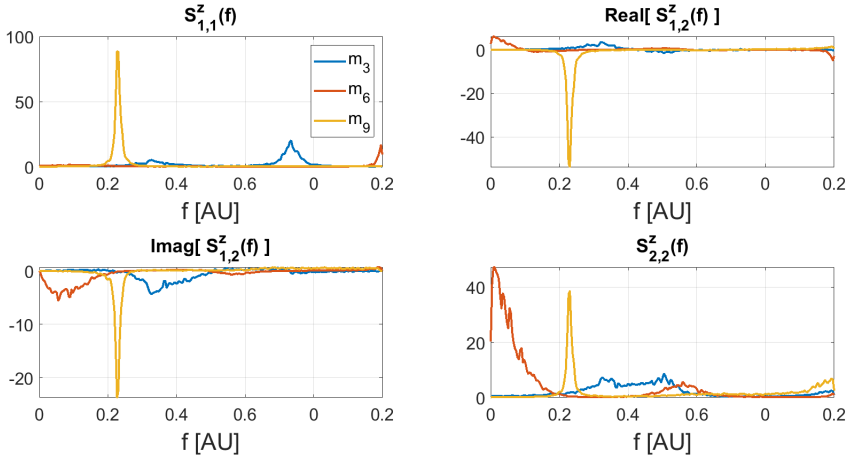

Figure 5.2: Real and imaginary part of the cross-power spectra of three simulated time series. Higher values of spectral complexity correspond to more peaked spectra.

leagues (Lagarias et al., 1998). More in details, $\lambda^*_{\mathbf{x}}$ and $\lambda^*_{\mathbf{S}}$ have been obtained by applying such procedure to $\varepsilon_{\mathbf{x}}(\lambda)$ and $\varepsilon_{\mathbf{S}}(\lambda)$, respectively; in both cases the starting point of the simplex method was set equal to $10^{\left(-\frac{\text{SNR}^{\mathbf{X}}}{10}\right)}$, which corresponds to the optimal value of $\lambda_{\mathbf{x}}$ in the case of white Gaussian signals (Vallarino et al., 2020). The blue box in figure 5.3 describes the inverse procedure to obtain an estimate of the cross-power spectrum and stresses the role of the regularisation parameter in the two-step process.

5.3 Results

In this section we illustrate the results of our analysis. We will begin with the description of the analytical dependence between $\text{SNR}^{\mathbf{X}}$ and $\text{SNR}^{\mathbf{S}}$, then we will highlight how the optimal parameter for the reconstruction of the cross-power spectrum depends on $\text{SNR}^{\mathbf{S}}$ and how this implies that the spectral complexity of the signal is behind such dependence. Finally we will show how the reconstruction error $\varepsilon_{\mathbf{S}}(\lambda)$ behaves for different values of the regularisation parameters. As a byproduct, this analysis also confirms the results of (Vallarino et al., 2020) in the case of a more complex setting.

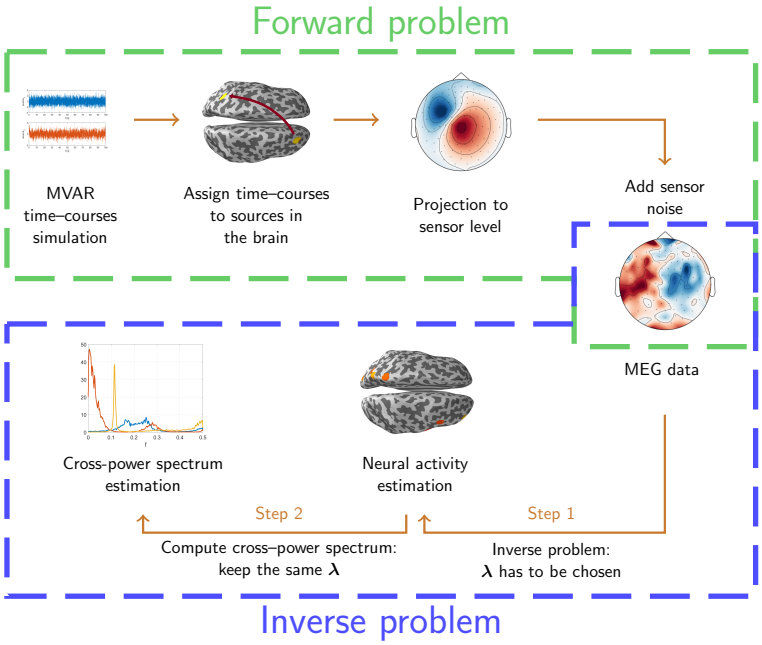

Figure 5.3: Pipeline of the simulation of the data (green box) and of the estimation of the cross-power spectrum (blue box).

5.3.1 Analytical relation between $\text{SNR}^{\mathbf{X}}$ and $\text{SNR}^{\mathbf{S}}$

From equations (5.7) and (5.9) and reminding that $\mathbf{N}(t) \sim \mathcal{N}(0, \alpha^2\mathbf{I})$ it follows that

$$\text{SNR}^{\mathbf{X}} = 10\log_{10}\left(\frac{\sum_t \|\mathbf{G}\mathbf{X}(t)\|_2^2}{MT\alpha^2}\right); \tag{5.11}$$

and

$$\text{SNR}^{\mathbf{S}} = 10\log_{10}\left(\frac{\sum_f \left\|\mathbf{G}\mathbf{S}^{\mathbf{X}}(f)\mathbf{G}^\top\right\|_F^2}{MN_f\alpha^2}\right), \tag{5.12}$$

where T is the number of time points and N_f is the number of frequencies used to compute the cross-power spectrum. Observe that to derive equation (5.12) we used the fact that the cross-power spectrum of a white noise Gaussian process of zero mean and covariance matrix $\alpha^2\mathbf{I}$ is $\mathbf{S}^{\mathbf{N}}(f) = \alpha^2\mathbf{I}$.

By isolating α^2 from equation (5.11) and substituting in equation (5.12) we

obtain

$$\text{SNR}^{\mathbf{S}} = 10\log_{10}\left(\frac{T^2 M \sum_f \left\|\mathbf{G}\mathbf{S}^{\mathbf{X}}(f)\mathbf{G}^\top\right\|_F^2}{N_f \sum_t \|\mathbf{G}\mathbf{X}(t)\|_2^4}\right) + 2\text{SNR}^{\mathbf{X}}. \tag{5.13}$$

Equation (5.13) relates the signal-to-noise ratio of $\mathbf{X}(t)$ with that of $\mathbf{S}^{\mathbf{X}}(f)$. It shows that, for same levels of $\text{SNR}^{\mathbf{X}}$, $\text{SNR}^{\mathbf{S}}$ changes with the spectral complexity coefficient of the signals. In fact, the higher the spectral complexity coefficient, the higher the quantity $\left\|\mathbf{G}\mathbf{S}^{\mathbf{X}}(f)\mathbf{G}^\top\right\|_F^2$. Intuitively, this happens because when the signal has a higher spectral complexity coefficient its cross-power spectrum is more peaked and thus it is stronger over the cross-power spectrum of the noise with respect to a signal with a lower spectral complexity coefficient.

5.3.2 Dependence of $\lambda^*_{\mathbf{S}}$ on $\text{SNR}^{\mathbf{S}}$

As described in Section 5.2 we simulated several sensor level configurations, based on different combinations of spectral complexity coefficients, source locations and $\text{SNR}^{\mathbf{X}}$ levels. For each configuration we collected the two optimal parameters $\lambda^*_{\mathbf{x}}$ and $\lambda^*_{\mathbf{S}}$ and we investigated their dependence on the signal-to-noise-ratio. In accordance with classic results from inverse theory (Hanke and Hansen, 1993), we found that $\lambda^*_{\mathbf{x}}$ depends on the signal-to-noise ratio. What is novel here is the relation between $\lambda^*_{\mathbf{S}}$ and both $\text{SNR}^{\mathbf{X}}$ and $\text{SNR}^{\mathbf{S}}$. Indeed for increasing $\text{SNR}^{\mathbf{X}}$ less regularisation is needed, but such dependence varies with the MVAR models. On the other side, the dependence of $\lambda^*_{\mathbf{S}}$ on $\text{SNR}^{\mathbf{S}}$ is neater and does not depend on the models. Figure 5.4 shows this result; on the left the regularisation parameters for the cross-power spectrum reconstruction versus $\text{SNR}^{\mathbf{X}}$ are shown, while on the right the same parameters are shown with respect to $\text{SNR}^{\mathbf{S}}$. For the ease of presentation the figure shows the parameters related to one source location; while on the left lines corresponding to different MVAR models have different heights, on the right they overlap.

5.3.3 $\lambda^*_{\mathbf{S}} < \lambda^*_{\mathbf{x}}$ and dependency from the spectral complexity

We also investigated the relation between the two optimal regularisation parameters. Figure 5.5 shows the ratio $\frac{\lambda^*_{\mathbf{S}}}{\lambda^*_{\mathbf{x}}}$ versus $\text{SNR}^{\mathbf{X}}$ for the simulated MVAR models. The ratio between the two parameters is always smaller than $\frac{1}{2}$, meaning that $\lambda^*_{\mathbf{S}} < \frac{1}{2}\lambda^*_{\mathbf{x}}$, as it was analytically proved in Chapter 4 (Vallarino et al., 2020). Further to this, the figure shows that for increasing spectral complexity coefficients this ratio gets smaller. This latter result is directly related to equation (5.13). In fact, for same levels of $\text{SNR}^{\mathbf{X}}$, signals with higher spectral complexity have higher

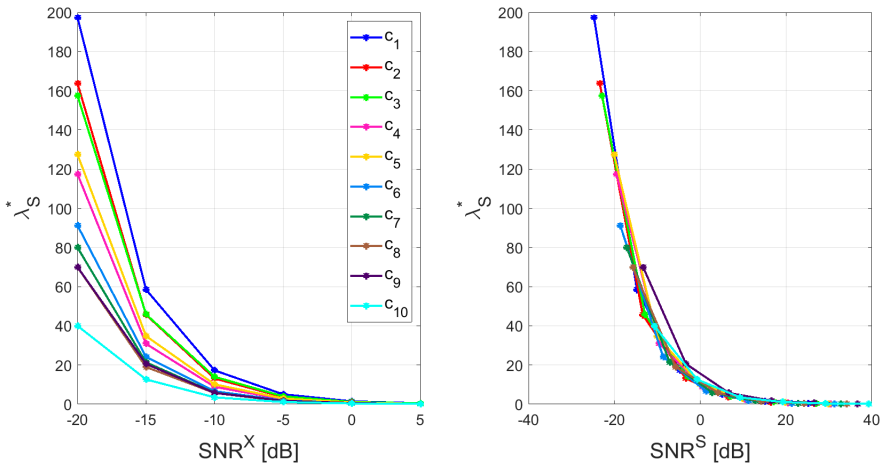

Figure 5.4: Optimal regularisation parameters for the reconstruction of the cross-power spectrum ($\lambda^*_{\mathbf{S}}$) as a function of $\text{SNR}^{\mathbf{X}}$ (left) and $\text{SNR}^{\mathbf{S}}$ (right). Different colours correspond to different MVAR models. On the left, the lines have different heights, while on the right they overlap, meaning that the dependence of $\lambda^*_{\mathbf{S}}$ on $\text{SNR}^{\mathbf{S}}$ is neater with respect to $\text{SNR}^{\mathbf{X}}$.

$\text{SNR}^{\mathbf{S}}$ and, thus, need less regularisation.

5.3.4 The reconstruction errors

To show the benefit of using a value of the regularisation parameter different from $\lambda^*_{\mathbf{x}}$ when estimating the cross-power spectrum, in Figure 5.6 we plotted the reconstruction errors $\varepsilon_{\mathbf{S}}(\lambda)$ as a function of the regularisation parameter (normalised by $\lambda^*_{\mathbf{x}}$) obtained when considering two illustrative realisations of the simulated sensor data. Specifically, we fixed the locations and time courses of the pair of interacting sources and we considered the corresponding simulated MEG data for two levels of $\text{SNR}^{\mathbf{X}}$, namely $\text{SNR}^{\mathbf{X}} = -20$ dB and $\text{SNR}^{\mathbf{X}} = 5$ dB. Similar results where obtained when considering the other source configurations.

As shown by Figure 5.6, for both the values of $\text{SNR}^{\mathbf{X}}$ the value of the reconstruction error significantly decreases when $\lambda^*_{\mathbf{S}}$ is used instead of $\lambda^*_{\mathbf{x}}$. Specifically in this simulation, $\varepsilon_{\mathbf{S}}(\lambda)$ drops from 0.99 to 0.96 when $\text{SNR}^{\mathbf{X}} = -20\text{dB}$, and from 0.92 to 0.77 when $\text{SNR}^{\mathbf{X}} = 5\text{dB}$.

Notably, one may observe that the relative reconstruction errors shown in Figure 5.6 are rather large, being above 90% in the low-SNR case and remaining above 75% even in the high-SNR scenario. We point out that this fact is mainly due to the combined effect of two factors: first, Tikhonov regularisation tends to produce reconstructions that are small but non-zero almost everywhere, as it reduces but does not cancel entirely backprojection of noise; second, in our simulations the

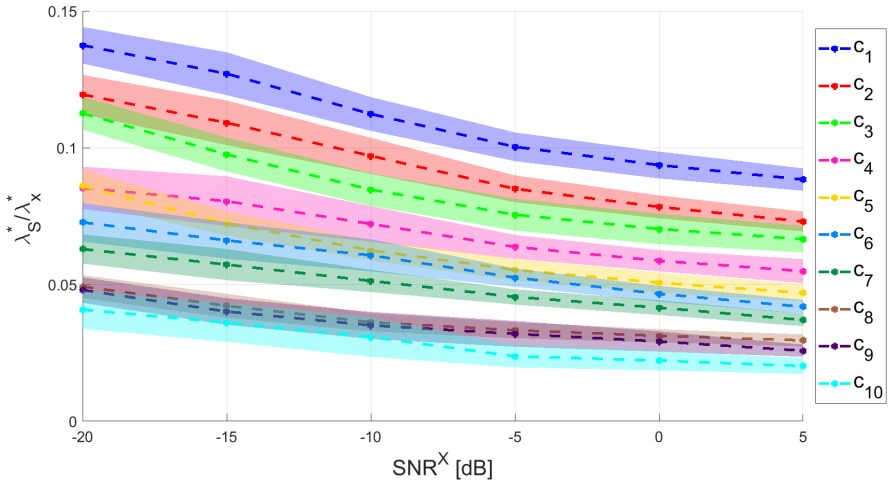

Figure 5.5: Ratio between the optimal parameters ($\frac{\lambda^*_{\mathbf{S}}}{\lambda^*_{\mathbf{x}}}$) as a function of $\text{SNR}^{\mathbf{X}}$. Different colours correspond to MVAR model with different spectral complexities. Dashed lines are the mean of the ratio over the different sources location, while solid colours correspond to the standard deviation of the mean.

true activity is zero everywhere but in two points. These two facts inevitably lead to large relative errors that, however, pleasantly decrease for increasing values of $\text{SNR}^{\mathbf{X}}$.

5.4 Discussion

In this chapter we presented the results published in (Vallarino et al., 2021b), where we investigated the role of the spectral complexity of a time series, $\mathbf{x}(t)$, in the design of an optimal inverse technique for estimating its cross-power spectrum, $\mathbf{S}^{\mathbf{x}}(f)$, from indirect measurements of the time series itself. Motivated by an analysis pipeline widely used for estimating brain functional connectivity from MEG data, we reconstructed the cross-power spectrum in two steps: first, we estimated the unknown time series by using the Tikhonov method; then we computed the cross-power spectrum of the reconstructed time series. In the present work, we used numerical simulations to study how the spectral complexity of $\mathbf{x}(t)$ impacts the value of the regularisation parameter that provides the best reconstruction of the cross-power spectrum.

As a first analytical result, we related $\text{SNR}^{\mathbf{X}}$ to $\text{SNR}^{\mathbf{S}}$, i.e. the signal-to-noise ratio of the time series and the signal-to-noise ratio of the corresponding cross-power spectra. The obtained formula suggests that, for a fixed level of $\text{SNR}^{\mathbf{X}}$, $\text{SNR}^{\mathbf{S}}$ depends on the spectral complexity of $\mathbf{x}(t)$: the higher the spectral complexity coefficient the higher $\text{SNR}^{\mathbf{S}}$. Intuitively this happens because a higher value

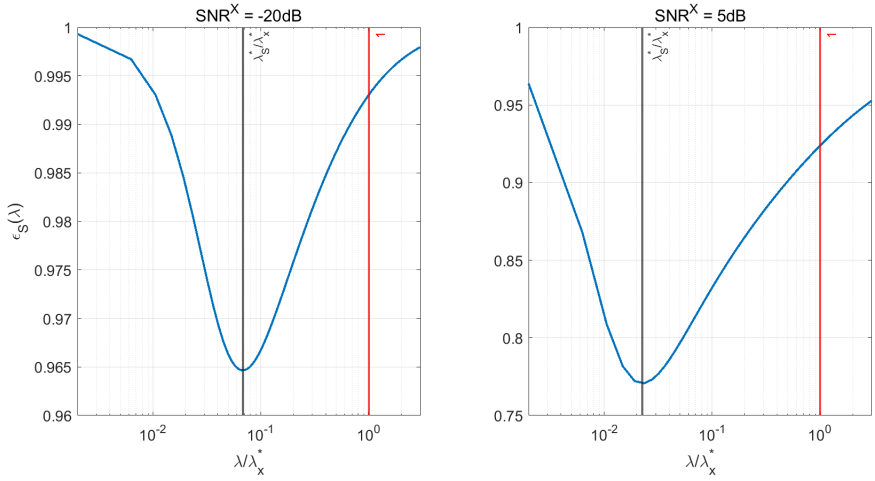

Figure 5.6: Reconstruction error $\varepsilon_{\mathbf{S}}(\lambda)$ for two simulated data mimicking MEG signals with $\text{SNR}^{\mathbf{X}} = -20$dB (lowest considered SNR, left panel) and $\text{SNR}^{\mathbf{X}} = 5$dB (highest considered SNR, right panel). In each panel black and red vertical lines highlight the values of $\varepsilon_{\mathbf{S}}(\lambda)$ in correspondence of $\lambda^*_{\mathbf{S}}$ and $\lambda^*_{\mathbf{x}}$, respectively.

of the spectral complexity coefficient corresponds to a more peaked cross-power spectrum that will emerge over the cross-power spectrum of the noise.

To test the effect of this result on the choice of the Tikhonov regularisation parameter in a practical scenario, we simulated a large set of MEG data and we applied the described two-step approach for estimating the cross-power spectrum of the underlying neural sources. In details, we simulated 1200 synthetic MEG data with varying $\text{SNR}^{\mathbf{X}}$ generated by pairs of coupled point-like sources at varying locations and with different spectral complexities. For each simulated data we computed the two parameters providing the best estimates of the time series ($\lambda^*_{\mathbf{x}}$) and of the cross-power spectrum ($\lambda^*_{\mathbf{S}}$), defined as the ones minimising the relative ℓ_2-norm of the difference between the true and the reconstructed time series/cross-power spectrum according to Definition 5.3. As shown by Figure 5.4, the results of our simulations highlighted a high correlation between the values of $\lambda^*_{\mathbf{S}}$ and of $\text{SNR}^{\mathbf{S}}$.

Eventually, we focused on the relationship between the two parameters $\lambda^*_{\mathbf{x}}$ and $\lambda^*_{\mathbf{S}}$, whose ratio is shown in Figure 5.5. The figure points out that this ratio depends on the spectral complexity of the simulated time series. This fact may be understood in lights of the previous results, as $\lambda^*_{\mathbf{S}}$ depends on $\text{SNR}^{\mathbf{S}}$ that in turns depends on the spectral complexity coefficient. Additionally, we found that, for all the simulated data, $\frac{\lambda^*_{\mathbf{S}}}{\lambda^*_{\mathbf{x}}} < \frac{1}{2}$, in line with the results shown in (Vallarino et al., 2020) for a simplified model where the neural time series were assumed to be white Gaussian processes. Moreover, when the spectral complexity coefficient increases ($c > 5$

in our simulations) the ratio between the two parameters approaches 0.01. This agrees with the results shown in (Hincapié et al., 2016) where, by simulating sinusoidal signals, the authors suggested to use for connectivity estimation a parameter of two orders of magnitude lower. In fact, our numerical results indicate that the use of $\lambda_{\mathbf{S}}^{*}$ results in a substantially lower reconstruction error on the cross-power spectrum, particularly when the data has a high SNR.

The work presented in this chapter focuses on the cross-power spectrum as a connectivity metric, however, it would be interesting to directly investigate the behaviour of the Tikhonov regularisation parameters when other metrics. Some preliminary results will be presented in the next chapter. Finally, the dependence of $\lambda_{\mathbf{S}}^{*}$ on $\mathrm{SNR}^{\mathbf{S}}$ suggests that an analysis of such dependence could be considered for the definition of a rule for choosing $\lambda_{\mathbf{S}}^{*}$ in practical scenarios.

Chapter 6

Numerical results on the two-step estimation of the connectivity metrics

In the previous chapters we investigated the issue of how to set the regularisation parameter to optimally estimate the cross-power spectrum in a two-step approach when using MNE to estimate the neural activity from MEG data. Interestingly, we found that less regularisation is needed to optimally estimate the cross-power spectrum and that an even smaller regularisation parameter should be set for increasing spectral complexity of the neural activity. However, the results of the previous chapters have the limitation of dealing only with the cross-power spectrum as connectivity metric and the assumptions on the neural activity were not fully realistic. In this chapter we consider the same problem, i.e. how to optimally set the regularisation parameter for connectivity estimation, however we widen the set of connectivity metrics and we simulated more complex neural activity configurations. Moreover, we changed the definition of optimality when defining the regularisation parameter for functional connectivity estimation. Indeed, such a definition is not univocal, another common choice to quantify the reliability of the estimated connectivity metrics, other than the ℓ_2-norm, is the area under the curve (AUC), which is the metric that was used in (Hincapié et al., 2016). Therefore in this chapter we will employ such a metric. Specifically, we simulated several MEG sensor level configuration and for each of them we computed the optimal regularisation parameters for neural activity and connectivity estimation. The results confirm and strengthen the ones presented in the previous chapters.

This chapter is organised as follow. In Section 6.1 we define the problem. In Section 6.2 we describe how we simulated the MEG data and the inverse model that we employed. In Section 6.3 the results are described. Finally, in Section 6.4

we discuss the results.

6.1 Definition of the problem

Let us consider the MEEG problem (3.19)

$$\mathbf{y}(t) = \mathbf{G}\mathbf{x}(t) + \mathbf{n}(t),$$

being $\mathbf{y}(t) \in \mathbb{R}^M$, $\mathbf{x}(t) \in \mathbb{R}^N$ and $\mathbf{n}(t) \in \mathbb{R}^M$ the sensor level recordings, the brain activity and the measurement noise, respectively. We are interested in estimating source space connectivity. To this end, we consider $\mathbf{x}(t)$ as a realisation of a multivariate stochastic process and we exploit some of the connectivity metrics defined in Section 3.6. Specifically, we focus on imaginary part of Coherence ($imCOH$), corrected imaginary part of Phase Locking Value ($ciPLV$) and weighted Phase Lax Index ($wPLI$). The rationale behind this choice is that the computation of such metrics starts from the computation of the cross-power spectrum, which is in line with the works presented in Chapters 4 and 5. Moreover, these metrics are modified from their original formulation in order to mitigate the impact on source leackage ad volume conduction. In parallel, in order to provide a more exhaustive and complete analysis and to compare the results with the findings presented in the previous chapters, we also focus on the estimation of the cross-power spectrum itself, and we exploit the Welch's method for its computation. That is, recalling Section 1.3.1,

$$\mathbf{S}^{\mathbf{x}}(f) = \frac{1}{PW}\sum_{p=1}^{P}\hat{\mathbf{x}}^p(f)\hat{\mathbf{x}}^p(f)^H, \qquad f = 0, \dots, L-1, \tag{6.1}$$

being $\hat{\mathbf{x}}^p(f) = \sum_{t=0}^{L-1}\mathbf{x}^p(t)w(t)e^{-\frac{2\pi i t f}{L}}$ and $W = \sum_{t=0}^{L-1}w(t)^2$.
To facilitate the reader we also recall the definitions of the other connectivity metrics. $imCOH$ between $x_j(t)$ and $x_k(t)$ is defined, starting from the cross-power spectrum, as

$$imCOH^{\mathbf{x}}_{j,k}(f) = \frac{\mathrm{Im}(S^{\mathbf{x}}_{j,k}(f))}{\sqrt{S^{\mathbf{x}}_{j,j}(f)S^{\mathbf{x}}_{k,k}(f)}}. \tag{6.2}$$

While $ciPLV$ and $wPLI$ are defined, respectively, as

$$ciPLV^{\mathbf{x}}_{j,k}(f) = \frac{\frac{1}{P}\left|\sum_{p=1}^{P}\frac{\mathrm{Im}\left(\hat{x}_j^{(p)}(f)\hat{x}_k^{(p)}(f)^*\right)}{|\hat{x}_j^{(p)}(f)||\hat{x}_k^{(p)}f)|}\right|}{\sqrt{1-\left(\frac{1}{P}\left|\sum_{p=1}^{P}\frac{\mathrm{Im}\left(\hat{x}_j^{(p)}(f)\hat{x}_k^{(p)}(f)^*\right)}{|\hat{x}_j^{(p)}(f)||\hat{x}_k^{(p)}f)|}\right|\right)^2}}, \tag{6.3}$$

and

$$wPLI^{\mathbf{x}}_{j,k}(f) = \frac{\left|\mathrm{Im}\left(S^{\mathbf{x}}_{j,k}(f)\right)\right|}{\frac{1}{P}\sum_{p=1}^{P}\left|\mathrm{Im}\left(\hat{x}_j^{(p)}(f)\hat{x}_k^{(p)}(f)^*\right)\right|}, \tag{6.4}$$

being $\hat{\mathbf{x}}^p(f) = \frac{1}{L}\sum_{t=0}^{L-1}\mathbf{x}^p(t)w(t)e^{-\frac{2\pi itf}{L}}$, $\mathrm{Im}(\cdot)$ is the imaginary part, and * the complex conjugate.
For the ease of notation we will use $\mathbf{C}^{\mathbf{x}}(f)$ to refer to each of the above defined connectivity metrics, indiscriminately.

In this work, we estimated source space connectivity through a two-step process, as described in Section 3.7:

i. First, a regularised estimate, $\mathbf{x}_\lambda(t)$, of the neural activity, $\mathbf{x}(t)$, is obtained by solving the MEEG inverse problem associated with equation (3.19). Here we consider the Minimum Norm Estimate (MNE) (Hämäläinen and Ilmoniemi, 1994b), which is defined as

$$\mathbf{x}_\lambda(t) = \arg\min_{\mathbf{x}(t)}\left\{\|\mathbf{G}\mathbf{x}(t) - \mathbf{y}(t)\|_2^2 + \lambda\|\mathbf{x}(t)\|_2^2\right\}; \tag{6.5}$$

   where λ is a proper regularisation parameter and $\|\cdot\|_2$ is the ℓ_2-norm.

ii. Then, the corresponding estimate of connectivity, $\mathbf{C}^{\mathbf{x}_\lambda}(f)$, is computed from the estimated time series.

When applying such a two-step process, one needs to set the parameter λ to estimate the neural activity during the first step. Thus it arises the question of how to properly set such a parameter. Counter-intuitively, the parameter providing the optimal estimate of neural activity may not provide the optimal estimate of connectivity. Such a result has already been shown in the previous chapters when connectivity is quantified by the cross-power spectrum and the optimal parameters are defined, barring a normalisation term, as the two values that minimise the ℓ_2-norm of the difference between the actual and estimated neural activity and cross-power spectrum respective. Here, we define optimality as follow.

Definition 6.1. Given the the MNE estimate (6.5), we define the optimal regularisation parameter for the reconstruction of $\mathbf{x}(t)$ as

$$\lambda^*_{\mathbf{x}} = \arg\min_{\lambda} \left\{ \sum_t \|\mathbf{x}_\lambda(t) - \mathbf{x}(t)\|_2^2 \right\}, \tag{6.6}$$

and the optimal parameter for connectivity estimation as

$$\lambda^*_{\mathbf{C}} = \arg \max_{\lambda \in \{\lambda_1,\dots,\lambda_k\}} \{\mathrm{AUC}(\mathbf{C}^{\mathbf{x}_\lambda})\}, \tag{6.7}$$

where $\{\lambda_1, \dots, \lambda_k\}$ is a proper set of parameters, and AUC is the area under the Receiver Operating Characteristic (ROC) curve, which is computed by plotting the True Positive Fraction (TPF) versus the False Positive Fraction (FPF) at different threshold levels.

6.2 Data generation and analysis pipeline

This section is dedicated to the description of the numerical simulation that led to the results of this work. First, we describe how we generated neural activity and sensor level recordings, then, we describe the inverse method and how we numerically computed the optimal regularisation parameters.

6.2.1 Data generation

We exploited the MEG model (3.19) to simulate several MEG recordings. We used a leadfied matrix, $\mathbf{G}$, available within the MNE Python package (Gramfort et al., 2014). We selected magnetometers and set a fixed orientation. For computational reasons the available source space, containing 312 273 sources, was down-sampled. Thus, our model consisted of M=102 sensors and N=6940 dipole sources.
Brain activity was generated with the following pipeline, which was implemented in a Python code.

1. We selected $N_{loc} = 50$ different pairs of sources (seeds) so that their distance is grater than 4 cm and that their intensity at source space level is similar.

2. For each pair of seeds we generated $N_A = 3$ different pair of patches, differing from one other for their extension, which was set equal to $A = 2\ \mathrm{cm}^2,\ 4\ \mathrm{cm}^2,\ 8\ \mathrm{cm}^2$.

3. We generated $N_{mod} = 20$ different pairs of time series, generated from as many MVAR models of order 5, with directional coupling from the first time

series to the second; and we filtered them in the alpha range, i.e. in $8-12$ Hz. The generated time series were assigned to each pair of patches, so that the seeds had maximum intensity, while the intensity of the surrounding sources decreased accordingly to their distance from the seeds.

4. Small perturbation in the frequency domain were introduced to the time series associated with sources within each pair of patches in order to obtain $N_c = 3$ different levels of intra coherence, namely $c = 0.2,\ 0.5,\ 1$.

5. Background activity was assigned to the remaining sources so that the inverse signal-to-noise ratio (SNR) between background activity and patches activity assumed $N_\gamma = 3$ different values, namely $\gamma = 0.1,\ 0.5,\ 0.9$. The time series of each of such sources followed a univariate AR model of order 5.

6. Finally, the simulated brain activity was projected to sensor level by means of the leadfield matrix and white Gaussian noise was added to obtain $N_{SNR} = 4$ different levels of SNR evenly spaced between -20 dB and 5 dB.

As for the MVAR models used to simulate the seed time series at point 4. we exploited equation (5.10). Whereas, the SNR at point 5. is defined as

$$\text{SNR} = \frac{\sum_t \|\mathbf{x}^{in}(t)\|_2^2}{\sum_t \|\mathbf{x}^{bg}(t)\|_2^2}, \tag{6.8}$$

where $\mathbf{x}^{in}(t)$ is the activity of interest, i.e the patches activity, and $\mathbf{x}^{bg}(t)$ is the background activity. On the other hand, the SNR at point 6. is defined as

$$\text{SNR} = \frac{\sum_t \|\mathbf{x}(t)\|_2^2}{\sum_t \|\mathbf{n}(t)\|_2^2}, \tag{6.9}$$

By combining all the mentioned features we obtained $N_{loc} \cdot N_A \cdot N_{mod} \cdot N_c \cdot N_\gamma \cdot N_{SNR} = 108\,000$ different sensor level configurations. Figure 6.1 shows a schematic representation of the simulation pipeline.

6.2.2 Inverse model

Source space activity was estimated using MNE (Hämäläinen and Ilmoniemi, 1994b). For each sensor level configuration we computed the optimal parameters for neural activity, $\lambda^*_{\mathbf{x}}$, and connectivity, $\lambda^*_{\mathbf{C}}$, estimations by exploiting Definitions 6.1 and 6.7, respectively. For the computation of $\lambda^*_{\mathbf{x}}$ we used the minimize function available within the Python package SciPy (Virtanen et al., 2020). Whereas, for the computation of $\lambda^*_{\mathbf{C}}$ we selected $k = 15$ values of parameters, $\{\lambda_1, \ldots, \lambda_k\}$,

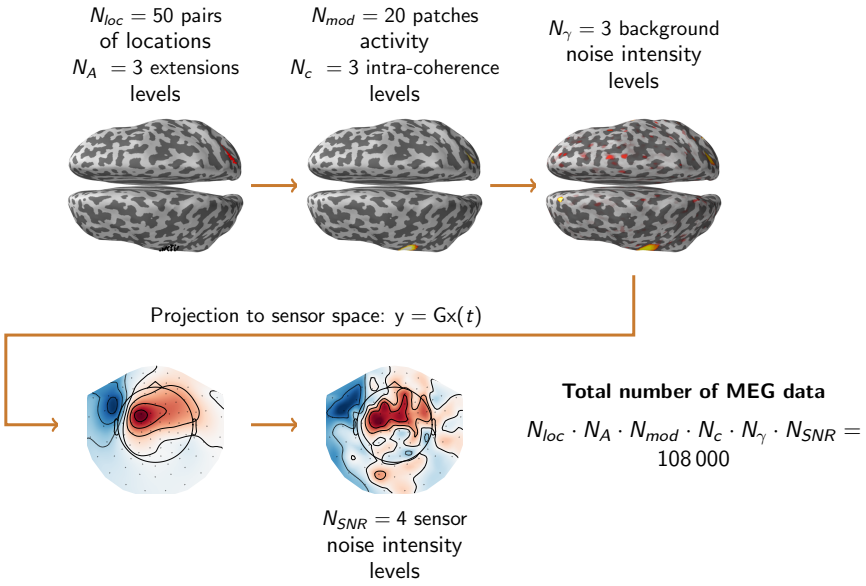

Figure 6.1: Pipeline of the simulation of the generated MEG sensor level data

logarithmically spaced between $\lambda^*_{\mathbf{x}} \cdot 10^{-5}$ and $\lambda^*_{\mathbf{x}} \cdot 10^{1}$. For each of such parameters we computed the corresponding AUC value, (i.e. $\text{AUC}(\mathbf{C}^{\mathbf{x}_{\lambda_i}})$, $i = 1, \ldots, k$). The AUC was computed by plotting the TPF versus the FPF at 20 different threshold levels, α,

$$\text{TPF}(\alpha) = \frac{\text{TP}(\alpha)}{N_{patch_1} \cdot N_{patch_2}}, \tag{6.10}$$

$$\text{FPF}(\alpha) = \frac{\text{FP}(\alpha)}{\frac{N(N+1)}{2} - N_{patch_1} \cdot N_{patch_2}}, \tag{6.11}$$

being N_{patch_1} and N_{patch_2} the number of sources within the simulated patches, thus $N_{patch_1} \cdot N_{patch_2}$ the number of simulated interactions; $\frac{N(N+1)}{2}$ the number of possible interactions between all sources in the source space; $\text{TP}(\alpha)$ the true positives, that is the number of connections between each source within the first patch and and each source within the second patch whose intensity are above α; and $\text{FP}(\alpha)$ the false positives, that is the number of connections between each source within the first patch and each source out of the patches whose intensity are above α. The intensity of each connection is computed as the norm over the frequency within the alpha band of the corresponding connectivity matrix (i.e $\sum_{f \in (8,12)\ Hz} |\mathbf{C}^{\mathbf{x}_\lambda}(f)|^2$).

6.3 Results

In this section we will describe the main results. First, we will show the results from the whole set of simulations. Then, we will show the results for an illustrative case.

6.3.1 Results on the whole set of simulations

Figure 6.2 shows the effect of the regularisation parameter on connectivity estimation in terms of the AUC values. In order to plot the results from all the simulated MEG configurations together, on the x-axis, we set the ratio between the tested parameters and the optimal parameter for the neural activity reconstruction, therefore the red line indicates a tested value of the regularisation parameter equal to the optimal one for neural activity reconstruction, i.e. $\lambda = \lambda^*_{\mathbf{x}}$. For all connectivity metrics the parameter providing the higher mean AUC value is about two order of magnitude lower than $\lambda^*_{\mathbf{x}}$. Such a result is in line with that presented by Hincapiè and colleagues in (Hincapié et al., 2016) and with the results presented in Chapter 4 and 5.

Figure 6.3 shows the regularisation parameters as a function of the SNR for all connectivity metric. The parameters are shown via boxplot; the green boxplots represent $\lambda^*_{\mathbf{x}}$, while the blue bxplots $\lambda^*_{\mathbf{C}}$. Accordingly to the previous chapters the value of the parameters decrease for increasing value of the SNR. We also observe that the $\lambda^*_{\mathbf{x}}$ boxplots show less variance with respect to $\lambda^*_{\mathbf{C}}$. This might be due to the different definition of the parameters, indeed $\lambda^*_{\mathbf{x}}$ assumes values in $\mathbb{R}_+$, while $\lambda^*_{\mathbf{C}}$ assumes values over a discrete set.

6.3.2 Results for an illustrative case

Figure 6.4 shows the improvement of functional connectivity estimation when $\lambda^*_{\mathbf{C}}$ is used instead of $\lambda^*_{\mathbf{x}}$. Indeed, for all connectivity metrics, the the connectivity estimate when $\lambda^*_{\mathbf{C}}$ is used (last column) is much more localised, with respect to the estimates obtained with $\lambda^*_{\mathbf{x}}$ (middle column); thus, resulting in an estimate that is closer to the ground truth (first column). This suggests that using an appropriate parameter does improve functional connectivity reconstruction.

6.4 Discussion

In this chapter we investigated the problem of how to set the regularisation parameter to estimate functional connectivity in a two-step approach, when MNE is used to estimate neural activity from MEG recordings. We simulated a large

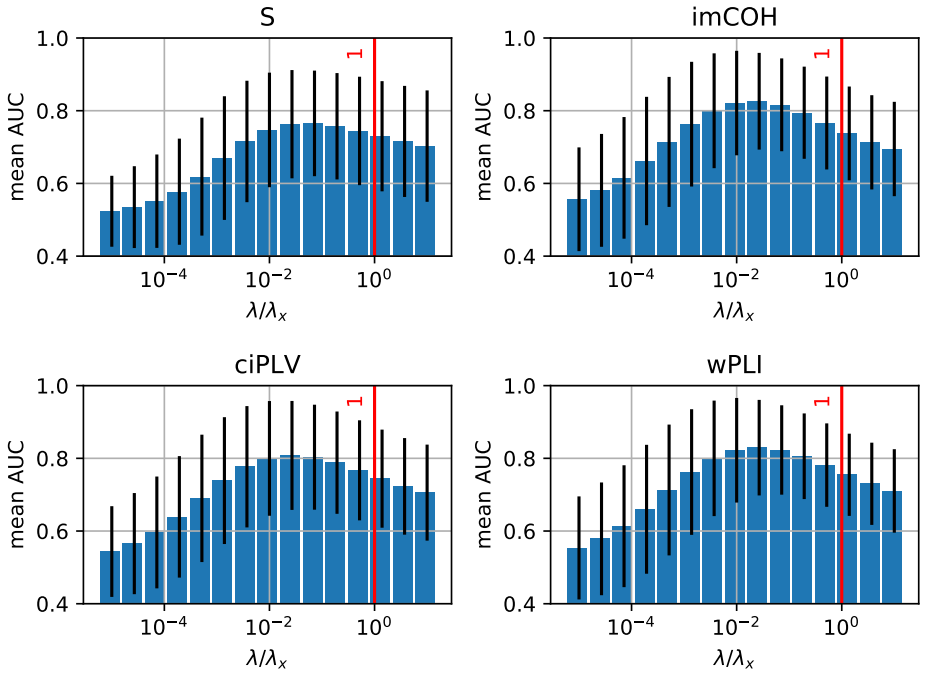

Figure 6.2: Bar plots of the mean AUC value for the tested regularisation parameters and for all connectivity metrics. On the x-axis there is the ratio between the tested parameters and the optimal parameters for neural activity reconstruction. The red line is in correspondence of $\lambda = \lambda^*_{\mathbf{x}}$, while the black lines represent the standard deviation.

amount of MEG data and for each configuration we computed the optimal parameters for neural activity and functional connectivity estimation. We employed four different connectivity metrics, namely the cross-power spectrum, the imaginary part of Coherence, the corrected imaginary part of Phase Locking Value and the weighted Phase Lag index. The results confirm and strengthen the finding presented in Chapters 4 and 5. Indeed, we found that less regularisation is needed to estimate brain activity when the final aim is to estimate functional connectivity, specifically the regularisation parameter providing the best possible estimate o functional connectivity is abut two orders of magnitude smaller than the one providing the best possible estimate of brain activity; such a results is in line with the results presented in (Hincapié et al., 2016). Moreover, through an illustrative example we showed that using a smaller parameter provides evident improvements. Indeed, as shown in Figure 6.4, in the latter case the estimated functional connectivity is much more localised.

The latter results highlights the need of determining a method to properly choose the regularisation parameter. To this end we are currently working on the implementation of a learning algorithm that infer the optimal regularisation param-

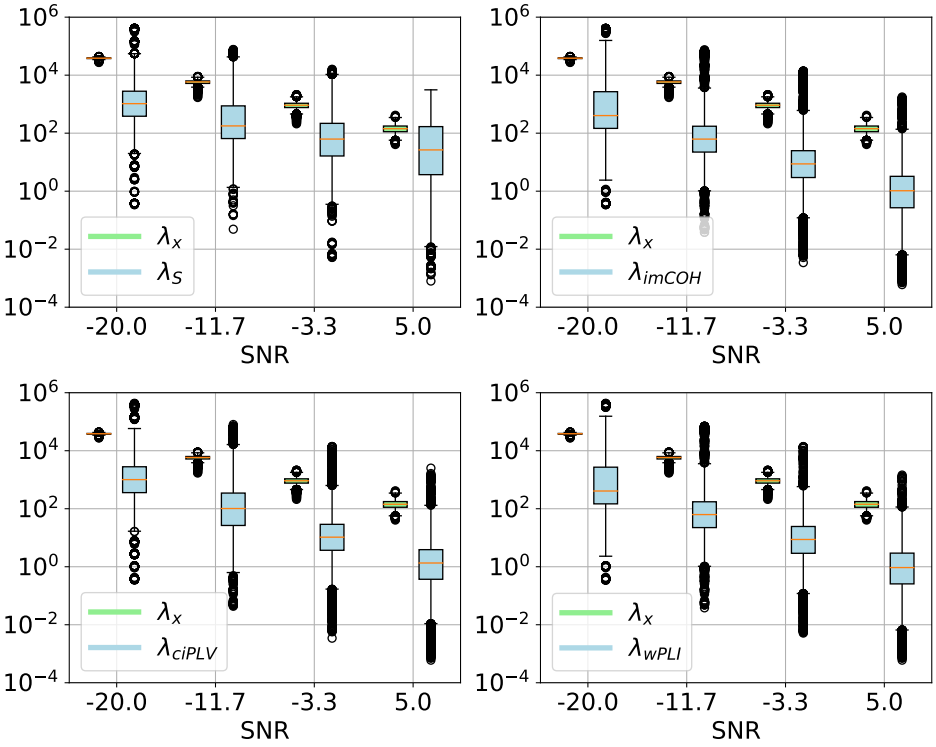

Figure 6.3: Values of $\lambda^*_{\mathbf{x}}$ and $\lambda^*_{\mathbf{C}}$ represented via boxplot as a function of SNR. The green boxplots are related to $\lambda^*_{\mathbf{x}}$ while the blue one to $\lambda^*_{\mathbf{C}}$.

eter from some features of the MEG recordings. The first step in this direction is to study the influence of all the different features that we set when we simulated the MEG data on the regularisation parameter.

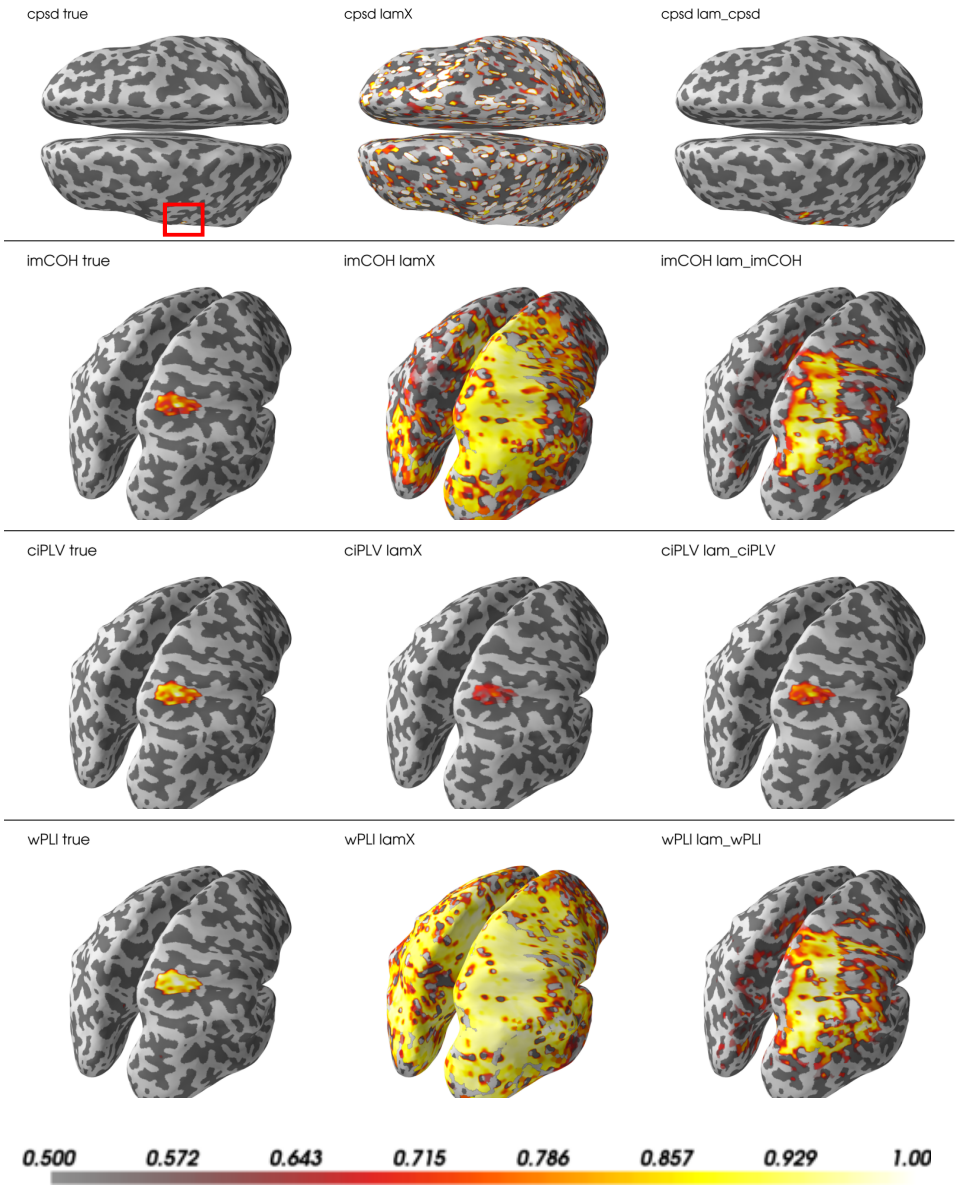

Figure 6.4: Improvements of connectivity estimation when λ^*_C is used instead of λ^*_x. Each row represent a different connectivity metric. The first column shows the simulated functional connectivity, the second column represents the one estimated when λ^*_x is set as regularisation parameter, while the third column represents the one estimated when λ^*_C is set as regularisation parameter.

Chapter 7

A one-step approach for the estimation of the cross power spectrum: some preliminary results

In the previous chapters we investigated the issue of properly setting the regularisation parameter to estimate brain functional connectivity in a two-step approach, when using Tikhonov regularisation method to estimate the neural activity from MEEG data. We intentionally focused on a commonly used pipeline in the neuroscientific community (Schoffelen and Gross, 2019b), but we did not focus on the drawbacks of the pipeline itself. Indeed, it is worth mentioning two main drawbacks. The first is that with a two-step approach the unavoidable errors that are committed when estimating the neural activity during the first step, inevitably propagate on the functional connectivity estimation. A one-step approach, where functional connectivity at source space level is directly estimated from that a sensor level might mitigate such an effect. A possible one-step approach has already been introduce in Chapter 4, where we showed that the Tikhonov filter factors associated with the linear problem that directly relates the cross-power spectrum at source space level with that at sensor level present a smoother behaviour that looks promising. The second drawback is the use of Tikhonov method to solve the inverse problem. Such a method has the great advantage of having a closed formula for the solution of the inverse problem, however the ℓ_2-norm in the penalty term (see Section 2.3) promotes smoothness in the solution, but, when dealing with brain activity this is not desirable, or rather it is desirable along time, but it is not in space as at any time typically few sources are active. Such a limitation can be overcome by employing ℓ_1-regularisation which has the peculiarity of promoting sparsity on

the solution.

It is with these premises that in this chapter we will investigate how a one-step approach together with ℓ_1 regularisation can improve functional connectivity estimation. Specifically we will show some preliminary results obtained by carrying on two simulations. In details, we simulated two MEEG sensor level configurations and for each of them we compared functional connectivity estimated on the one hand with the standard two-step approach plus Tikhonov regularisation, on the other hand with the one-step approach plus ℓ_1 regularisation.

This chapter is organised as follow. In Section 7.1 we will describe the one-step forward problem, while Section 7.2 is dedicated to the inverse problem. In Section 7.3 we describe how we generated the data. In Section 7.4 we will present the results. Finally, we will discuss the results in Section 7.5.

7.1 Forward modeling

Let us consider the MEEG problem (3.19)

$$\mathbf{y}(t) = \mathbf{G}\mathbf{x}(t) + \mathbf{n}(t),$$

which can be interpreted as a realisation of the linear model

$$\mathbf{Y}(t) = \mathbf{G}\mathbf{X}(t) + \mathbf{N}(t), \tag{7.1}$$

being $\mathbf{y}(t) \in \mathbb{R}^M$, $\mathbf{x}(t) \in \mathbb{R}^N$ and $\mathbf{n}(t) \in \mathbb{R}^M$ realisations of the real-valued multivariate stationary stochastic processes $\mathbf{Y}(t)$, $\mathbf{X}(t)$ and $\mathbf{N}(t)$, and $\mathbf{G} \in \mathbb{R}^{M\times N}$ a leadfield matrix. $\mathbf{N}(t)$ is the measurement noise process, which is assumed to be a white Gaussian process with zero mean and covariance matrix $\alpha^2\mathbf{I}$, i.e. $\mathbf{N}(t) \sim \mathcal{N}(0, \alpha^2\mathbf{I})$, independent from $\mathbf{X}(t)$. We are interested in estimating the cross-power spectrum of $\mathbf{X}(t)$, defined, extending Definitions 1.8 and 1.10, as follows.

Definition 7.1. Consider two real-valued multivariate stationary stochastic processes, $\{\mathbf{X}(t)\}_{t\in\mathbb{R}}$ and $\{\mathbf{W}(t)\}_{t\in\mathbb{R}}$, where $\mathbf{X}(t) = (X_1(t), \dots, X_N(t))^\top \in \mathbb{R}^N$ and $\mathbf{W}(t) = (W_1(t), \dots, W_M(t))^\top \in \mathbb{R}^M$. Denoted with $\mathbf{R}^{\mathbf{XW}}(\tau)$ the corresponding correlation function, that is $\mathbf{R}^{\mathbf{XW}}(\tau) = \mathbb{E}\left[\mathbf{X}(t)\mathbf{W}(t+\tau)\right]^\top$, we assume $R^{\mathbf{XW}}_{j,k}(\tau)$ to be absolutely integrable for all $j = 1, \dots, N$ and $k = 1, \dots, M$.
Then, the cross-power spectrum between $\mathbf{X}(t)$ and $\mathbf{W}(t)$ is a one-parameter family of complex-valued matrices $\mathbf{S}^{\mathbf{XW}}(f) \in \mathbb{C}^{N\times M}$, whose entries are defined as the Fourier transform of the corresponding correlation function

$$S^{\mathbf{XW}}_{j,k}(f) = \int_{-\infty}^{+\infty} R^{\mathbf{XW}}_{j,k}(\tau) e^{-2\pi i f\tau} d\tau\,. \tag{7.2}$$

Remark 7.2. *If we consider* $\mathbf{W} = \mathbf{X}$ *in the above definition, we obtain the cross-power spectrum of the process* $\{\mathbf{X}(t)\}_{t\in\mathbb{R}}$*, as defined in Definition 1.10; i.e. a one–parameter family of matrices of size* $N \times N$ *which is denoted as* $\mathbf{S}^{\mathbf{X}}(f) := \mathbf{S}^{\mathbf{XX}}(f)$*. Analogously, for the correlation function we return to Definition 1.8, that is* $\mathbf{R}^{\mathbf{X}}(\tau) := \mathbf{R}^{\mathbf{XX}}(\tau)$*.*

We now resume and extend some concepts that have been introduced in Chapter 4, which are needed for the definition of the one-step linear model.

Proposition 7.3. *Consider two real-valued multivariate stationary stochastic processes,* $\{\mathbf{X}(t)\}_{t\in\mathbb{R}}$ *and* $\{\mathbf{W}(t)\}_{t\in\mathbb{R}}$*, of size* N *and* M*, respectively. Denoted with* $\mathbf{M}^H$ *the Hermitian transpose of a matrix* $\mathbf{M}$*, the following properties hold.*

(a) $\mathbf{S}^{\mathbf{X}}(f) = \mathbf{S}^{\mathbf{X}}(f)^H \quad \forall f$

(b) Given $\mathbf{A} \in \mathbb{R}^{P\times N}$*,* $\mathbf{B} \in \mathbb{R}^{P\times M}$ *and defined* $\mathbf{Z}(t) = \mathbf{AX}(t) + \mathbf{BW}(t)$*, then*

$$\mathbf{S}^{\mathbf{Z}}(f) = \mathbf{AS}^{\mathbf{X}}(f)\mathbf{A}^\top + \mathbf{AS}^{\mathbf{XW}}(f)\mathbf{B}^\top + \mathbf{BS}^{\mathbf{WX}}(f)\mathbf{A}^\top + \mathbf{BS}^{\mathbf{W}}(f)\mathbf{B}^\top \tag{7.3}$$

(c) If $\mathbf{X}(t)$ *and* $\mathbf{W}(t)$ *are independent, then* $\mathbf{S}^{\mathbf{XW}}(f) = 0$*.*

Proof. (a) Because of the stationarity of $\{\mathbf{X}(t)\}_{t\in\mathbb{R}}$, for all $k, j = 1, \dots, N$

$$R^{\mathbf{X}}_{k,j}(\tau) = \mathbb{E}[X_k(t)X_j(t+\tau)] = \mathbb{E}[X_k(t-\tau)X_j(t)] = R^{\mathbf{X}}_{j,k}(-\tau)\,.$$

Thus, the thesis follows from Definition 7.1. Indeed

$$\begin{aligned} S^{\mathbf{X}}_{k,j}(f) = \int_{-\infty}^{+\infty} R^{\mathbf{XW}}_{k,j}(\tau)e^{2\pi i f\tau}d\tau &= \int_{-\infty}^{+\infty} R^{\mathbf{XW}}_{j,k}(-\tau)e^{-2\pi i f\tau}d\tau \\ &= \overline{\int_{-\infty}^{+\infty} R^{\mathbf{XW}}_{j,k}(\tau')e^{-2\pi i f\tau'}d\tau'} = \overline{S^{\mathbf{X}}_{j,k}(f)} \end{aligned}$$

where in the second to last equations we have used the fact that $R^{\mathbf{XW}}_{j,k}(\tau) \in \mathbb{R}$ and set $\tau' = -\tau$.

(b) From the linearity of the mean it follows that

$$\begin{aligned} \mathbf{R}^{\mathbf{Z}}(\tau) &= \mathbb{E}\left[(\mathbf{AX}(t) + \mathbf{BW}(t))(\mathbf{AX}(t+\tau) + \mathbf{BW}(t+\tau))^\top\right] \\ &= \mathbf{AR}^{\mathbf{X}}(\tau)\mathbf{A}^\top + \mathbf{AR}^{\mathbf{XW}}(\tau)\mathbf{B}^\top + \mathbf{BR}^{\mathbf{WX}}(\tau)\mathbf{A}^\top + \mathbf{BR}^{\mathbf{W}}(\tau)\mathbf{B}^\top\,. \end{aligned}$$

Therefore the thesis follows form Definition 7.1, by exploiting the linearity of the Fourier Transform.

(c) Since $\mathbf{X}(t)$ and $\mathbf{W}(t)$ are independent, $\mathbf{R}^{\mathbf{XW}}(\tau) = 0$ for all τ. Therefore, the thesis follows straightforwardly from Definition 7.1.

□

Let us now get back to equation (7.1)

$$\mathbf{Y}(t) = \mathbf{G}\mathbf{X}(t) + \mathbf{N}(t).$$

The processes $\{\mathbf{X}(t)\}_{t\in\mathbb{R}}$, $\{\mathbf{Y}(t)\}_{t\in\mathbb{R}}$ and $\{\mathbf{N}(t)\}_{t\in\mathbb{R}}$ satisfy the hypothesis of Proposition 7.1, thus it immediately follows that the cross-power spectrum of $\{\mathbf{Y}(t)\}_{t\in\mathbb{R}}$ is

$$\mathbf{S}^{\mathbf{Y}}(f) = \mathbf{G}\mathbf{S}^{\mathbf{X}}(f)\mathbf{G}^{\top} + \mathbf{S}^{\mathbf{N}}(f)\,. \tag{7.4}$$

Equation (7.4) defines a linear relationship between the cross-power spectrum of the observable process $\{\mathbf{Y}(t)\}_{t\in\mathbb{R}}$ and that of the unknown process $\{\mathbf{X}(t)\}_{t\in\mathbb{R}}$. More explicitly, we denote with $\mathcal{S}^{\mathbf{X}}(f) \in \mathbb{C}^{N^2}$, and $\mathcal{S}^{\mathbf{Y}}(f), \mathcal{S}^{\mathbf{N}}(f) \in \mathbb{C}^{M^2}$ the vector obtained by stacking the columns of matrices $\mathbf{S}^{\mathbf{X}}(f)$, $\mathbf{S}^{\mathbf{Y}}(f)$, and $\mathbf{S}^{\mathbf{N}}(f)$, respectively. From Equation (7.4) if follows

$$\mathcal{S}^{\mathbf{Y}}(f) = \mathbf{G} \otimes \mathbf{G}\mathcal{S}^{\mathbf{X}}(f) + \mathcal{S}^{\mathbf{N}}(f) \tag{7.5}$$

where $\otimes$ is the Kronecker product.

By splitting real and imaginary parts, Equation (7.5) can be rewritten so to include only real-valued quantities:

$$\begin{pmatrix} \mathrm{Re}(\mathcal{S}^{\mathbf{Y}}(f)) \\ \mathrm{Im}(\mathcal{S}^{\mathbf{Y}}(f)) \end{pmatrix} = \begin{pmatrix} \mathbf{G}\otimes\mathbf{G} & 0 \\ 0 & \mathbf{G}\otimes\mathbf{G} \end{pmatrix} \begin{pmatrix} \mathrm{Re}(\mathcal{S}^{\mathbf{X}}(f)) \\ \mathrm{Im}(\mathcal{S}^{\mathbf{X}}(f)) \end{pmatrix} + \begin{pmatrix} \mathrm{Re}(\mathcal{S}^{\mathbf{N}}(f)) \\ \mathrm{Im}(\mathcal{S}^{\mathbf{N}}(f)) \end{pmatrix}. \tag{7.6}$$

For the ease of notation, let us define

$$\underline{\mathcal{S}}^{\mathbf{W}}(f) \coloneqq (\mathrm{Re}(\mathcal{S}^{\mathbf{W}}(f)), \mathrm{Im}(\mathcal{S}^{\mathbf{W}}(f)))^{\top} \tag{7.7}$$

$$\mathcal{G} = \begin{pmatrix} \mathbf{G}\otimes\mathbf{G} & 0 \\ 0 & \mathbf{G}\otimes\mathbf{G} \end{pmatrix} \tag{7.8}$$

so that equation (7.6) can be written in compact form as

$$\underline{\mathcal{S}}^{\mathbf{Y}}(f) = \mathcal{G}\underline{\mathcal{S}}^{\mathbf{X}}(f) + \underline{\mathcal{S}}^{\mathbf{N}}(f). \tag{7.9}$$

Finally, we stress that in MEEG applications the above equations define a linear relationship between the cross-power spectrum the process that models the MEEG recordings, $\mathcal{S}^{\mathbf{Y}}(f)$, and that of the process that models brain activity, $\mathcal{S}^{\mathbf{X}}(f)$, being $\mathcal{S}^{\mathbf{N}}(f)$, the cross-power spectrum of the process that models the measurement

noise.

7.2 Inverse modelling

As mentioned in the introduction of the current chapter, here we are interested in investigating the potentials of a one-step approach, where the cross-power spectrum at source-space level is directly estimated from that at sensor level, together with the use of ℓ_1 regularisation to promote sparsity on the solution. To validate the proposed method we compared it with the classic two-step approach involving Tikhonov regularisation. In the next two sections we first recall the two-step approach, then we describe the one-step approach.

7.2.1 Two-step approach

The two step estimate of the cross-power spectrum is achieved, accordingly to Section 3.7, as follow.

i. First, a regularised estimate, $\mathbf{x}_\lambda(t)$, of the neural activity, $\mathbf{x}(t)$, is obtained by solving the MEEG inverse problem associated with equation (3.19). Here we consider the Minimum Norm Estimate (MNE) (Hämäläinen and Ilmoniemi, 1994b), which is defined as

$$\mathbf{x}_\lambda(t) = \arg\min_{\mathbf{x}(t)} \left\{ \|\mathbf{G}\mathbf{x}(t) - \mathbf{y}(t)\|_2^2 + \lambda \|\mathbf{x}(t)\|_2^2 \right\}; \qquad (7.10)$$

where λ is a proper regularisation parameter and $\|\cdot\|_2$ is the ℓ_2-norm.

ii. Then the cross-power spectrum, $\mathbf{S}^{\mathbf{x}_\lambda}(f)$, is computed from the estimated time series by exploiting Whelch's method (Welch, 1967).

In order to compute the regularised estimate of neural activity the parameter λ needs to be set. Here, among all possible $\lambda > 0$, we consider the one that provides the optimal estimate of neural activity, where optimality is quantified in terms of the ℓ_2-norm of the difference between the estimated and actual neural activity.

Definition 7.4. Given the regularised solution (7.10), we define the optimal regularisation parameter for the reconstruction of $\mathbf{x}(t)$ as

$$\lambda^*_{\mathbf{x}} = \arg\min_{\lambda} \varepsilon_{\mathbf{x}}(\lambda) \qquad \text{with} \qquad \varepsilon_{\mathbf{x}}(\lambda) = \sum_t \|\mathbf{x}_\lambda(t) - \mathbf{x}(t)\|_2^2; \qquad (7.11)$$

$\varepsilon_{\mathbf{x}}(\lambda)$ will be called reconstruction error.

7.2.2 One-step approach

Let us consider a realisation of equation (7.9)

$$\underline{\mathcal{S}}^{\mathbf{y}}(f) = \mathcal{G}\underline{\mathcal{S}}^{\mathbf{x}}(f) + \underline{\mathcal{S}}^{\mathbf{n}}(f), \tag{7.12}$$

where capital letters $\mathbf{Y}$, $\mathbf{X}$ and $\mathbf{N}$ gave way to small letters $\mathbf{y}$, $\mathbf{x}$ and $\mathbf{n}$ to indicate that we are dealing with realisations of the processes that model MEEG recordings, brain activity and measurement noise respectively. The one-step approach consists in estimating source space level cross-power spectrum, $\underline{\mathcal{S}}^{\mathbf{x}}(f)$, directly from sensor level cross-power spectrum, $\underline{\mathcal{S}}^{\mathbf{y}}(f)$, by solving the inverse problem associated with equation (7.12). To solve such a problem here we use ℓ_1 regularisation method, that is, we solve the minimisation problem

$$\arg\min_{\mathbf{x}}\{\Phi_\lambda(\underline{\mathcal{S}}^{\mathbf{x}}(f))\} \tag{7.13}$$

being

$$\begin{aligned} \Phi_\lambda : \mathbb{R}^{2N^2} &\longrightarrow \mathbb{R} \\ \underline{\mathcal{S}}^{\mathbf{x}}(f) &\longmapsto \|\mathcal{G}\underline{\mathcal{S}}^{\mathbf{x}}(f) - \underline{\mathcal{S}}^{\mathbf{y}}(f)\|_2^2 + \lambda\|\underline{\mathcal{S}}^{\mathbf{x}}(f)\|_1. \end{aligned} \tag{7.14}$$

We implemented the Fast Iterative Shrinkage-Thresholding Algorithm (FISTA) (Beck and Teboulle, 2009) to compute the solution of problem (7.13). More details on ℓ_1 regularisation and FISTA can be found in Section 2.3.3, however in the following we will provide some information on how we implemented the algorithm in this specific case.

Fast Iterative Shrinkage-Thresholding Algorithm (FISTA)

First of all, for computational reasons the algorithm we implemented finds a solution to problem (7.13) for a specific frequency. Henceforth, for the ease of notation, we drop the dependence on frequency of the cross-power spectra, with the meaning that we are evaluating them at the desired frequency. We implemented FISTA on matlab based on the paper of Beck and Teboulle (Beck and Teboulle, 2009). The pseudocode of the algorithm is reported in Algorithm 1. To speed up the computation of $\underline{\mathcal{S}}_k^{\mathbf{x}} = (\mathrm{Re}\mathcal{S}_k^{\mathbf{x}}, \mathrm{Im}\mathcal{S}_k^{\mathbf{x}})^\top$ and $\underline{\mathcal{W}}_k = (\mathrm{Re}\mathcal{W}_k, \mathrm{Im}\mathcal{W}_k)^\top$ at lines 4 and 6 we computed the real and imaginary parts separately, that is

$$\mathrm{Re}\mathcal{S}_k^{\mathbf{x}} = \mathcal{T}_{\frac{\lambda}{L}}\left(\mathrm{Re}\mathcal{W}_{k-1} - \frac{2}{L}(\mathbf{G}\otimes\mathbf{G})^\top((\mathbf{G}\otimes\mathbf{G})\mathrm{Re}\mathcal{W}_{k-1} - \mathrm{Re}\mathcal{S}^{\mathbf{y}})\right) \tag{7.15}$$

$$\mathrm{Im}\mathcal{S}_k^{\mathbf{x}} = \mathcal{T}_{\frac{\lambda}{L}}\left(\mathrm{Im}\mathcal{W}_{k-1} - \frac{2}{L}(\mathbf{G}\otimes\mathbf{G})^\top((\mathbf{G}\otimes\mathbf{G})\mathrm{Im}\mathcal{W}_{k-1} - \mathrm{Im}\mathcal{S}^{\mathbf{y}})\right), \tag{7.16}$$

and

$$\mathrm{Re}\mathcal{W}_k = \mathrm{Re}\mathcal{S}_k^{\mathbf{x}} + \frac{t_{k-1}-1}{t_k}(\mathrm{Re}\mathcal{S}_k^{\mathbf{x}} - \mathrm{Re}\mathcal{S}_{k-1}^{\mathbf{x}}), \tag{7.17}$$

$$\mathrm{Im}\mathcal{W}_k = \mathrm{Im}\mathcal{S}_k^{\mathbf{x}} + \frac{t_{k-1}-1}{t_k}(\mathrm{Im}\mathcal{S}_k^{\mathbf{x}} - \mathrm{Im}\mathcal{S}_{k-1}^{\mathbf{x}}). \tag{7.18}$$

We set the maximum number of iterations, K, equal to 10 000, the tolerance ε equal to 10^{-5}. Accordingly to Section 2.3.3 we set the Lipschitz constant as $L = 2\sigma_{max}(\mathcal{G}^\top\mathcal{G})$; to compute the eigenvalues of $\mathcal{G}^\top\mathcal{G}$ we observed that it is a block diagonal matrix thus its eigenvalues correspond to that of the blocks that define it, i.e $(\mathbf{G}\otimes\mathbf{G})^\top(\mathbf{G}\otimes\mathbf{G})$. Now, the singular values of $\mathbf{G}\otimes\mathbf{G}$ are the products between all possible pairs of singular values of $\mathbf{G}$, thus, denoted with σ_M the maximum singular value of $\mathbf{G}$, the maximum singular value of $\mathbf{G}\otimes\mathbf{G}$ is σ_M^2; and finally the maximum eigenvalue of $(\mathbf{G}\otimes\mathbf{G})^\top(\mathbf{G}\otimes\mathbf{G})$, which is equal to that of $\mathcal{G}$ is σ_M^4. We initialised $\underline{\mathcal{S}}_0^{\mathbf{x}}$ as a Gaussian random vector of zero mean and standard deviation 1. Finally, we run the algorithm for different values of regularisation parameters, λ. We recall that the regularisation parameter trades off the importance given to the penalty and the fidelity terms in equation (7.14); high values of λ generate a too sparse solution that badly fits the data, on the contrary small values of λ generate a little sparse solution that overfits the data. To find a reasonable range for the tested parameters we computed the quantity $2\|\mathcal{G}^\top\underline{\mathcal{S}}^{\mathbf{y}}\|_\infty$ which has been proven to be the upper bound to find non-null solutions (Gerstoft et al., 2015). Then, we set 15 values of λ logarithmically spaced between $2\|\mathcal{G}^\top\underline{\mathcal{S}}^{\mathbf{y}}\|_\infty\cdot 10^{-3}$ and $2\|\mathcal{G}^\top\underline{\mathcal{S}}^{\mathbf{y}}\|_\infty\cdot 10^{-1}$.

7.3 Data generation and simulation pipeline

We exploited the MEEG linear model (3.19) to generate two MEEG sensor level recordings, corresponding to two different brain activity configurations. We used a leadfild matrix available in the sample dataset of MNE Python (Gramfort et al., 2014). We selected magnetometers and set a fixed orientation. For computational reasons, the available source space, containing 1884 sources, was uniformly down-sampled to obtain 274 sources. Thus, our model had $M = 102$ sensors and $N = 274$ dipole sources. For the generation of brain activity, we simulated two different triplets of sources, $(z_1(t), z_2(t), z_3(t))^\top$, whose time series followed two different multivariate autoregressive (MVAR) models of order $P = 5$. As for one brain activity configuration, we imposed unirectional coupling from the first source to the second, while the third one was uncorrelated. The MVAR model that we used to simulate such a configuration was

Algorithm 1: FISTA applied to $\underline{\mathcal{S}}^{\mathbf{y}} = \mathcal{G}\underline{\mathcal{S}}^{\mathbf{x}} + \underline{\mathcal{S}}^{\mathbf{n}}$

Input: $\underline{\mathcal{S}}_0^{\mathbf{x}}$, $\underline{\mathcal{S}}^{\mathbf{y}}$, $\mathcal{G}$, L, λ, K, ε
Output: $\underline{\mathcal{S}}_{k_{end}}^{\mathbf{x}}$

Initialization: $t_0 = 1$, $\underline{\mathcal{W}}_0 = \underline{\mathcal{S}}_0^{\mathbf{x}}$
while $k < K$ **do**
  $k = k + 1$
  $\underline{\mathcal{S}}_k^{\mathbf{x}} = \mathcal{T}_{\frac{\lambda}{L}}\left(\underline{\mathcal{W}}_{k-1} - \frac{2}{L}\mathcal{G}^{\top}(\mathcal{G}\underline{\mathcal{W}}_{k-1} - \underline{\mathcal{S}}^{\mathbf{y}})\right)$
  $t_k = \frac{1}{2} + \frac{1}{2}\sqrt{1 + 4t_{k-1}^2}$
  $\underline{\mathcal{W}}_k = \underline{\mathcal{S}}_k^{\mathbf{x}} + \frac{t_{k-1} - 1}{t_k}(\underline{\mathcal{S}}_k^{\mathbf{x}} - \underline{\mathcal{S}}_{k-1}^{\mathbf{x}})$
  $e = \frac{\|\underline{\mathcal{S}}_k^{\mathbf{x}} - \underline{\mathcal{S}}_{k-1}^{\mathbf{x}}\|_1}{2N^2}$
  if $e < \varepsilon$ **then**
    break
return $\underline{\mathcal{S}}_{k_{end}}^{\mathbf{x}}$

$$\begin{pmatrix} z_1(t) \\ z_2(t) \\ z_3(t) \end{pmatrix} = \sum_{k=1}^{P} \begin{pmatrix} a_{1,1}(k) & 0 & 0 \\ a_{2,1}(k) & a_{2,2}(k) & 0 \\ 0 & 0 & a_{3,3}(k) \end{pmatrix} \begin{pmatrix} z_1(t-k) \\ z_2(t-k) \\ z_2(t-k) \end{pmatrix} + \begin{pmatrix} \varepsilon_1(t) \\ \varepsilon_2(t) \\ \varepsilon_3(t) \end{pmatrix}, \quad t = 0, \ldots, T-1. \tag{7.19}$$

For the other brain activity configuration, we imposed unidirectional coupling from the first source to the second, and from the first to the third. The corresponding MVAR model was

$$\begin{pmatrix} z_1(t) \\ z_2(t) \\ z_3(t) \end{pmatrix} = \sum_{k=1}^{P} \begin{pmatrix} a_{1,1}(k) & 0 & 0 \\ a_{2,1}(k) & a_{2,2}(k) & 0 \\ a_{3,1}(k) & 0 & a_{3,3}(k) \end{pmatrix} \begin{pmatrix} z_1(t-k) \\ z_2(t-k) \\ z_2(t-k) \end{pmatrix} + \begin{pmatrix} \varepsilon_1(t) \\ \varepsilon_2(t) \\ \varepsilon_3(t) \end{pmatrix}, \quad t = 0, \ldots, T-1. \tag{7.20}$$

The non-zero elements $a_{i,j}(k)$ of the coefficient matrices were drown from a normal distribution of zero mean and standard deviation 0.9, and $T = 10\ 000$. We retained only (i) coefficient matrices providing a stable MVAR model [88];

(ii) triplets of signals, $(z_1(t), z_2(t), z_3(t))^\top$, such that the ℓ_2-norm of the strongest one was less than 3 times the ℓ_2-norm of the weakest one; and (iii) triplet of signals, $(z_1(t), z_2(t), z_3(t))^\top$, such that the non-null out of diagonal elements of the cross-power spectrum at the frequency at which they peaked were greater then $1/3$ of the corresponding diagonal elements. Each triplet of time series was assigned to a different triplet of sources randomly chosen in the source space so that their distance was grater than 4 cm, and their intensity at sensor level was similar, that is the ratios of the norms of the corresponding columns of the leadfield matrix were close to one. Null activity was assigned to the remaining $N - 3$ sources. Afterwards, the simulated brain activity was projected to sensor level by multiplying for the leadfield matrix and white Gaussian noise was added so that the signal-to-noise ratio was 5 dB.
Starting from the simulated MEEG recordings we then estimated source space cross-power spectrum by exploiting both the two-step and the one-step approaches. As for the two-step approach we followed the pipeline described in Section 7.2.1: (i) first, we estimated the neural activity using Tikhonov method and setting the regularisation parameter by numerically minimising the reconstruction error, $\varepsilon_{\mathbf{x}}(\lambda)$, using the built-in matlab function fminsearch that implements an iterative procedure based on the simplex method developed by Lagarias and colleagues (Lagarias et al., 1998) and setting the starting point of the simplex method equal to $10^{\left(-\frac{\text{SNR}^{\mathbf{x}}}{10}\right)}$, which corresponds to the optimal value of $\lambda_{\mathbf{x}}$ in the case of white Gaussian signals (Vallarino et al., 2020); (ii) then, from the estimated neural activity, we computed the cross-power spectrum. As for the one-step approach, we first computed the sensor-level cross-power spectrum, then we applied FISTA, as described in Section 7.2.2, to problem (7.13) setting the frequency as the one at which the cross-power spectrum of the simulated brain activity peaked. During both approaches the cross-power spectra were computed by exploiting Welch's method (Welch, 1967).

7.4 Results

Figures 7.1 and 7.2 show the real and imaginary parts, respectively, of the simulated and estimated cross-power spectra, related to the brain activity simulated by exploiting MVAR model (7.19). All spectra in the figures were computed at the frequency at which the cross-power spectrum of the simulated brain brain activity peaked, i.e. the frequency that was used to apply FISTA. In both figures the top row shows the cross-power spectrum of the simulated data, i.e. the ground truth. The numbers on the vertices indicate the source numbers; in this case there was directional coupling from source 1 to source 2, while the third source was uncorrelated.

The green dots in correspondence of the third source indicate its position. The middle and bottom lines show the estimated cross-power spectra by using the one-step and the two-step approaches. In all cases, only connections with intensity in the top 90% were displayed. As for the cross-power spectrum estimated with the one-step approach, only the reconstruction obtained with one regularisation parameter is shown. Such a parameter has been chosen by visual inspection as the one providing the best estimate. It is clear from the figures that the one-step approach plus ℓ_1 regularisation outperforms the classic two-step approach with Tikhonov regularisation. Indeed the one-step approach correctly identifies source 1 and source 2 and the connection between them, while the two-step approach estimates a cloud of connections around the true sources.

Figures 7.3 and 7.4 are the analogue of Figures 7.1 and 7.2, when exploiting MVAR model (7.20). In this case directional coupling from source 1 to source 2 and from source 1 to source 3 was simulated, however, as the first line of the figures, i.e. the ground truth, shows, also connection between source 2 and 3 was present. This is due to the fact that being source 2 and 3 led by the same source, they inevitably show connection between each other, from a statistical viewpoint. This is due to the fact that we are showing the results related to one specific frequency, which may not be representative of the coupling configuration. Also in this case is clear that the one-step approach plus ℓ_1 regularisation outperforms the two step approach plus Tikhonov regularisation. Indeed the one-step approach correctly reconstruct the locations of the active sources and the connections among them, while the two-step approach fails.

7.5 Discussion

In this chapter we showed some preliminary results on the potentials of using a one-step approach to directly estimate the cross-power spectrum of brain activity from the cross-power spectrum of the corresponding MEEG recordings. Specifically, we simulated two brain activity configurations and we generated the corresponding sensor level recordings. We then applied the proposed one-step approach and we compared the estimated cross-power spectra with that obtained by using the classic two-step approach. From Figures 7.1, 7.2, 7.3 and 7.4 it is evident that the proposed method outperforms the classic two-step approach. Indeed, in both cases the one-step approach correctly identifies the active sources and estimates the connections among them, while the two-step approach estimates several spurious connections, which make it impossible to individuate the true ones.

The results we showed regarding the one-step approach refer to a specific regu-

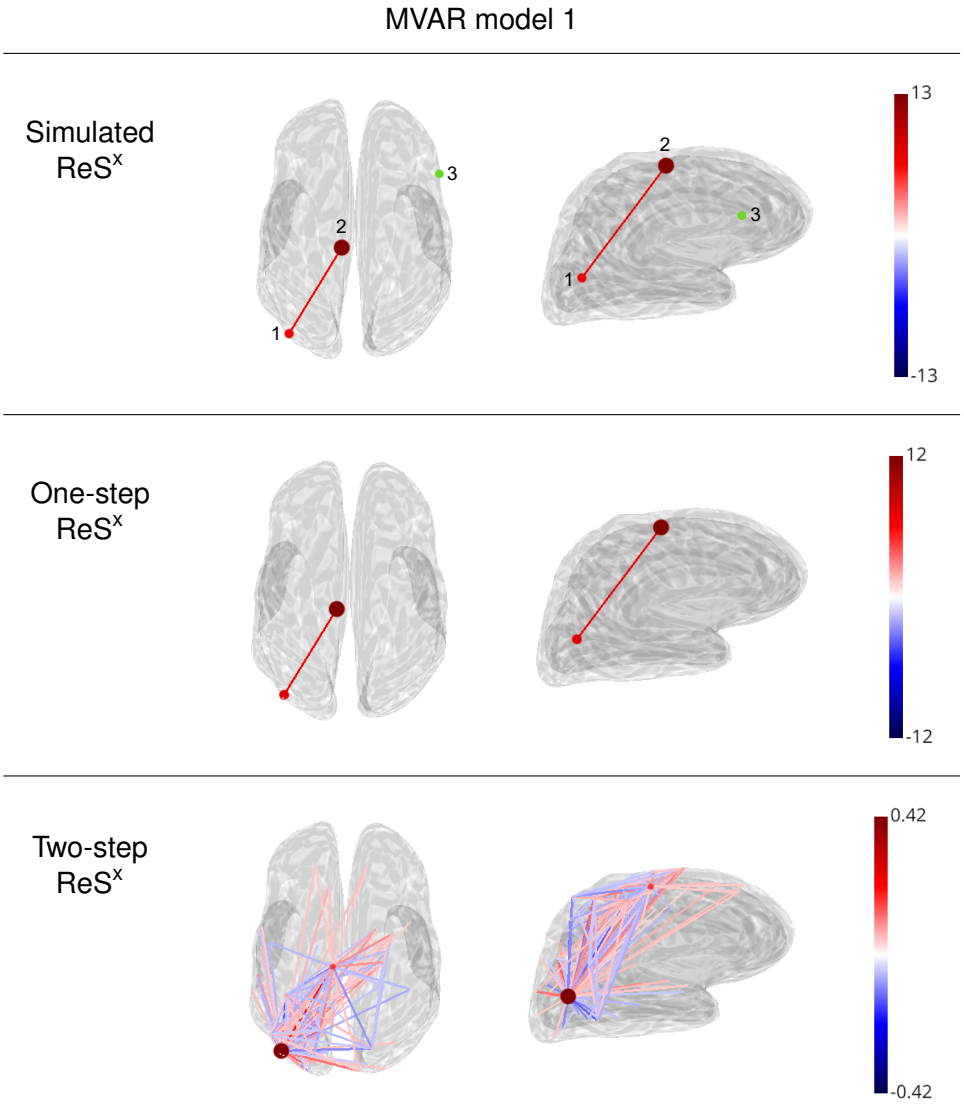

Figure 7.1: Real parts of the simulated cross-power spectra and the ones estimated with the one-step and two-step approaches. Numbers on the top row indicate the simulated sources, whose time courses where simulated exploiting MVAR model 7.19, thus directional coupling from source 1 to source 2 and from source 1 to source 3 was imposed. Only the top 90% connections in absolute value are displayed. Green dots in correspondence of the third sources show the location of the third source, which otherwise would not appear in the plot being the intensities of the components of the cross-power spectrum involving it in the lower 10%.

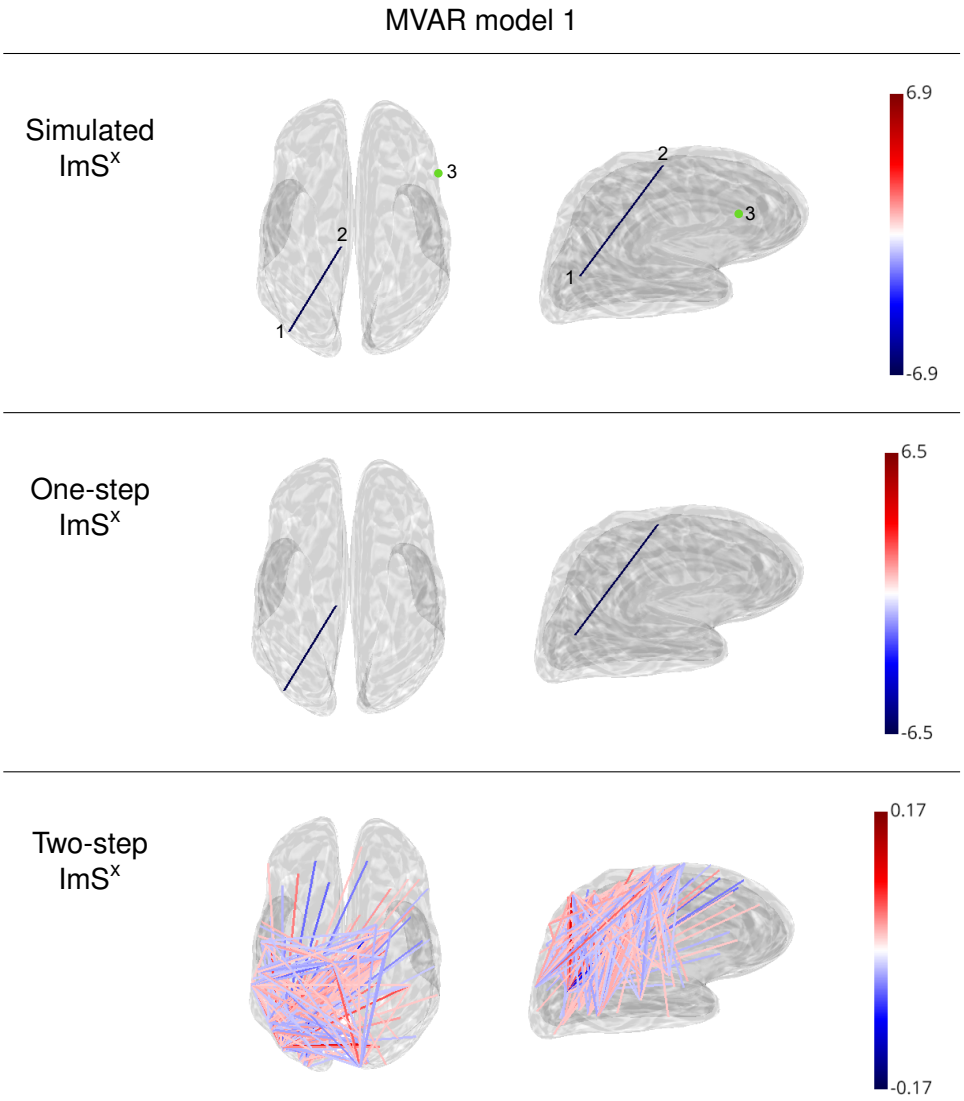

Figure 7.2: Imaginary parts of the simulated cross-power spectra and the ones estimated with the one-step and two-step approaches. Numbers on the top row indicate the simulated sources, whose time courses where simulated exploiting MVAR model 7.19, thus directional coupling from source 1 to source 2 and from source 1 to source 3 was imposed. Only the top 90% connections in absolute value are displayed. Green dots in correspondence of the third sources show the location of the third source, which otherwise would not appear in the plot being the intensities of the components of the cross-power spectrum involving it in the lower 10%.

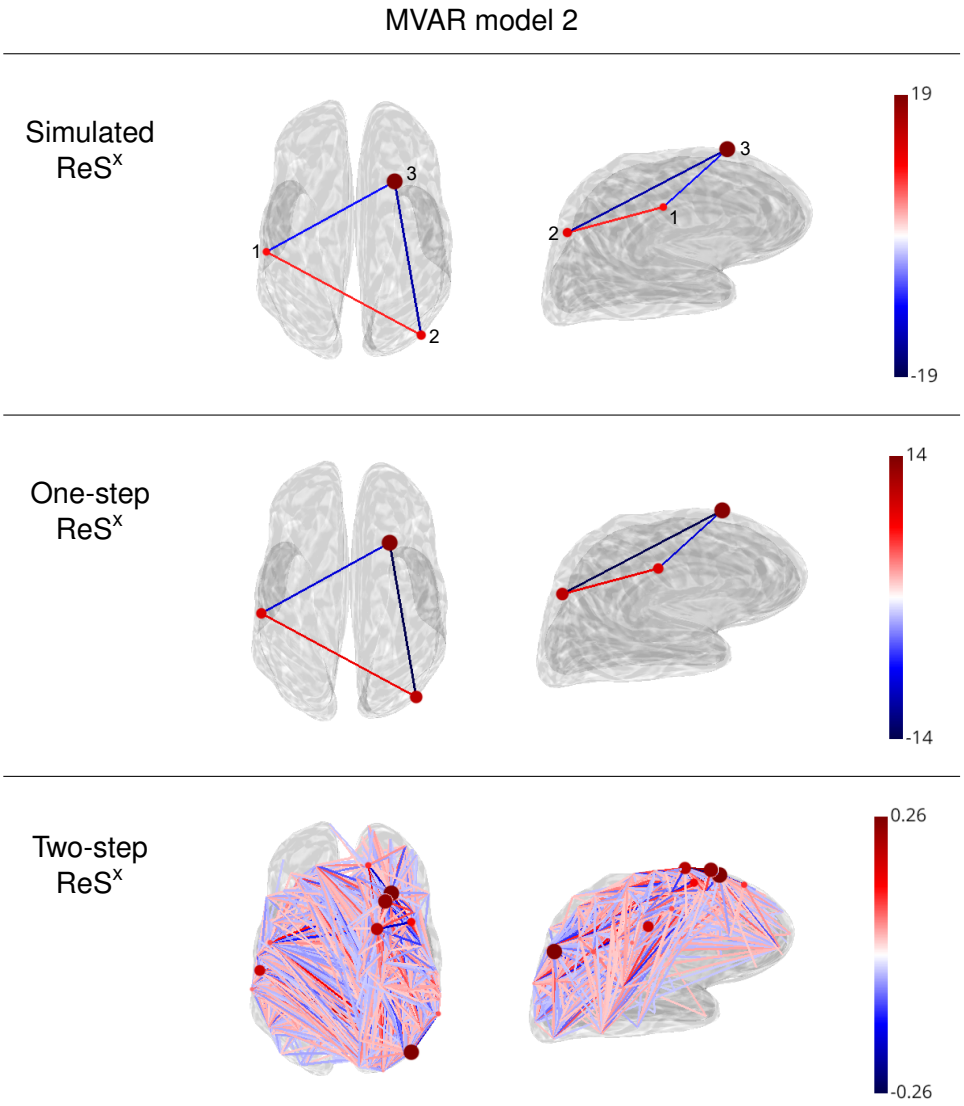

Figure 7.3: Real parts of the simulated cross-power spectra and the ones estimated with the one-step and two-step approaches. Numbers on the top row indicate the simulated sources, whose time courses where simulated exploiting MVAR model 7.20, thus directional coupling from source 1 to source 2, while the third was uncorrelated. Only the top 90% connections in absolute value are displayed.

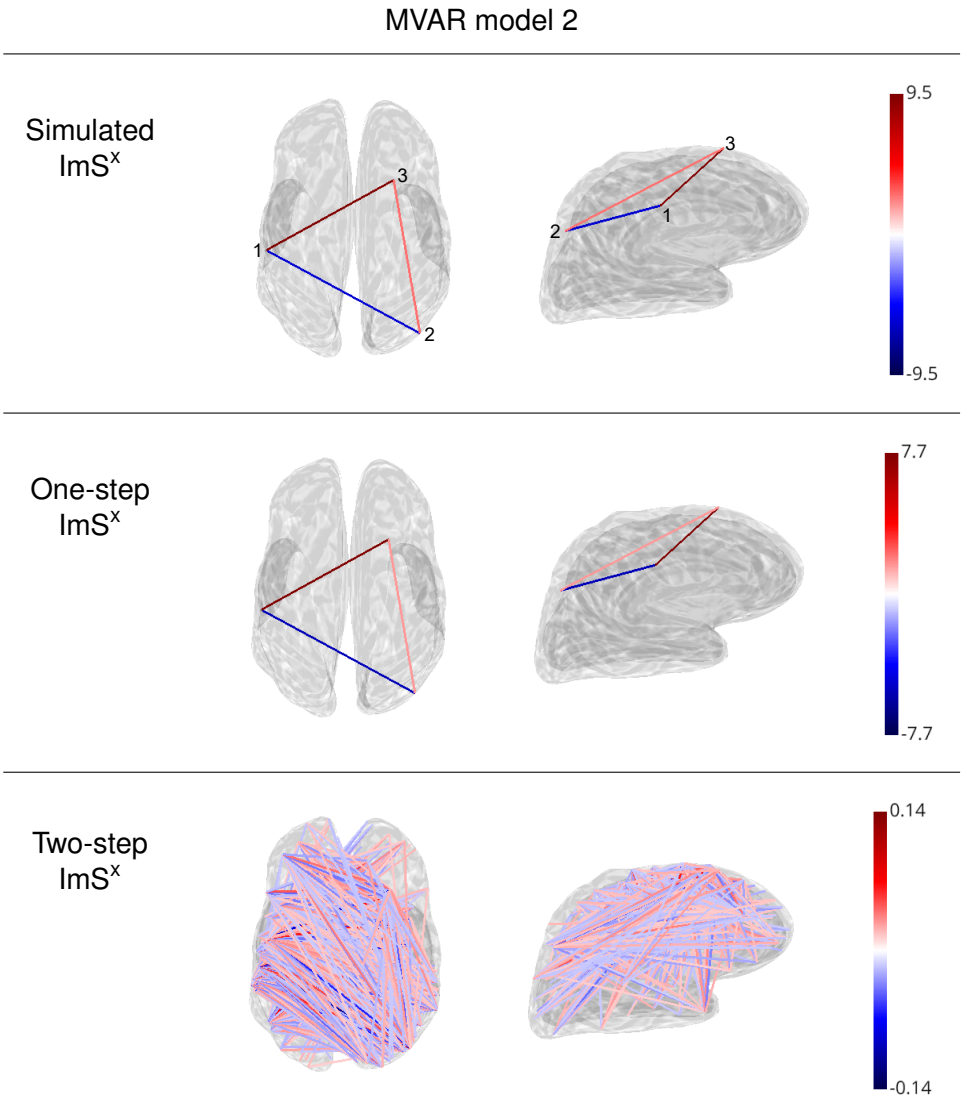

Figure 7.4: Imaginary parts of the simulated cross-power spectra and the ones estimated with the one-step and two-step approaches. Numbers on the top row indicate the simulated sources, whose time courses where simulated exploiting MVAR model 7.20, thus directional coupling from source 1 to source 2, while the third was uncorrelated. Only the top 90% connections in absolute value are displayed.

larisation parameter, λ, which was selected by visual inspection. That is, we tested several parameters, and we showed the one that provided the best cross-power spectrum estimate. The rational behind this choice is that we wanted to compare the one-step and the two-step approaches at their best performances. In fact, also the regularisation parameter for the two-step estimate of the cross-power spectrum was automatically selected as the one providing the best results. Of course, such a choice is not feasible in experimental contexts, where the ground truth is, of curse, not available, however it let us to show the potentials of our method. Future works will investigate the problem of setting the regularisation parameter in experimental contexts.

Finally we must say that, for computational reason, we had to down-sample the source space. Thus, our source space contained only 274 sources. Such a number is small, compared to the dense source spaces that contain up to $30\ 000$ sources, however it is a reasonable number when compared to studies that divide the brain into bigger areas and only study connectivity among these areas (Shen et al., 2012; Mai et al., 2015; Toga et al., 2006).

Chapter 8

Towards applications: the computation of the theta-to-alpha transition frequency from resting state EEG data

In the previous chapters we investigated the problem of optimally estimating brain functional connectivity from MEEG data. The analysis was conducted both in analytical and numerical frameworks, employing, for the latter a large number of simulated data. We mainly focused on the methodological insights of estimating functional connectivity, however it also worth mentioning that functional connectivity can provide important information about brain functioning in both healthy subjects and patients. Numerous studies demonstrated that the spectral content of functional connectivity in the natural frequency bands in patients affected by neurodegenerative diseases is different from that of healthy subjects (Musaeus et al., 2019; Babiloni et al., 2017; Núñez et al., 2019; Duan et al., 2020). Thus, functional connectivity analysis might be a powerful tool in the process of diagnosis (Mammone et al., 2018; Morabito et al., 2016). To this end a correct identification of the natural frequency bands at an individual level is of utmost importance.

In this chapter we will present the results of (Vallarino et al., 2021a), i.e. we will introduce a novel method for the identification of the theta-to-alpha transition frequency (TF). Indeed there is evidence that the EEG power in the alpha band and in the slow-wave frequency bands (e.g. theta and delta) shows a direct and an inverse correlation with cognitive performances, respectively. However, such harmonic behaviours often present significant individual differences (Donoghue et al., 2020) and, moreover, alpha and theta bands, whose power expresses opposite pathophysiological meanings, are contiguous. Therefore, at the individual

level the risk is consistent that part of the alpha power band is included in the range of the theta power (i.e., 4-8 Hz), thus implying a wrong interpretation of its (patho)physiological meaning. Establishing TF at an individual level is therefore of paramount importance in order to avoid misinterpretation of quantitative EEG (qEEG) data. The availability of a computational tool for the determination of TF represents a crucial prerequisite for a meaningful usability of frequency-band power analysis for both research and clinical purposes.

The current standard for TF determination is represented by a more than twenty years old study performed by Klimesch (Klimesch, 1999). This approach relies on the fact that event-related de-synchronisation induces a decrease of the alpha power and an increase of the theta power of the event-related power spectrum, with respect to the power spectrum measured during resting state (Klimesch et al., 1997). It immediately follows that theta-to-alpha TF can be determined by comparison between the task-related and the resting state power spectra. Klimesch's approach has been successfully used in a number of papers (Singh et al., 2015; Moretti et al., 2004, 2007; Saad et al., 2018). However, its main drawbacks are that (i) it needs the acquisition of two data sets, i.e. a resting state and a event-related time series; and (ii) the task utilised for event-related recording must induce changes in the power spectrum significant enough to allow the identification of variations in the alpha and theta power.

This chapter introduces *transfreq*, a publicly-available Python package implementing a novel algorithm for the automated computation of TF from theta to alpha band that works even when just resting-state EEG time series are available. This computational approach relies on the determination of appropriate features associated with the power spectrum measured at each channel, and on the application of an unsupervised algorithm that automatically identifies two clusters of EEG sensors associated with the alpha and theta bands, respectively. In *transfreq* we implemented four different strategies for selecting the sensor-level features and the corresponding clustering algorithms (Saxena et al., 2017). The workflow of these approaches is illustrated in the case of a test-bed example and validated on both an open-source data set and time series recorded during an experiment performed in our laboratory. For most subjects in both data sets *transfreq* estimate a value of TF close to that obtained by using Klimesch's method. Additionally, we show some typical scenarios in which the classic Klimesch's method fails in capturing the correct TF while *transfreq* still returns plausible estimates.

This chapter is organised as follows. Section 8.1 describes the novel method and compares it with the standard Klimesch's approach. Section 8.2 illustrates the results obtained by applying the method in the case of two data sets. Finally in Section 8.3 we will discuss the results.

8.1 Materials and methods

8.1.1 Klimesch's method

A classic approach to compute theta-to-alpha TF is that proposed by Klimesch (Klimesch, 1999) and schematically depicted in Figure 8.1A. In detail, Kilmesch's method requires two EEG recordings as input, one acquired during a resting-state condition and one acquired while the subject is performing a task. For both recordings and for each of the N EEG sensors, the power spectrum (Vallarino et al., 2020; Bendat and Piersol, 2011) of the corresponding time series is computed and normalised by dividing for the norm over all frequencies, i.e., we computed

$$\widetilde{P}_i^{task}(f) = \frac{P_i^{task}(f)}{\sum_f P_i^{task}(f)} \quad \text{and} \quad \widetilde{P}_i^{rest}(f) = \frac{P_i^{rest}(f)}{\sum_f P_i^{rest}(f)}\,, \tag{8.1}$$

where $P_i^{task}(f)$ and $P_i^{rest}(f)$ are the power spectra at frequency f of the signal recorded by the i-th sensor during the task and the resting-state conditions, respectively. Then, the mean over all the EEG channels of the normalised power spectra in (8.1) is computed to obtain two spectral profiles, namely

$$S_{task}(f) = \frac{1}{N}\sum_{i=1}^{N} \widetilde{P}_i^{task}(f) \quad \text{and} \quad S_{rest}(f) = \frac{1}{N}\sum_{i=1}^{N} \widetilde{P}_i^{rest}(f)\,. \tag{8.2}$$

Klimesch's method relies on the fact that S_{rest} usually presents a peak in the alpha band while, due to task-related alpha de-synchronisation, S_{task} presents a lower intensity in the alpha band and a higher intensity in the theta band with respect to S_{rest} (Klimesch, 1996; Klimesch et al., 1998; Schacter, 1977). TF is thus defined as the highest frequency before the individual alpha peak (IAP) at which S_{task} and S_{rest} intersect. Here, the IAP is defined as the frequency in the range [7, 13] Hz at which S_{rest} peaks (Babiloni et al., 2004).

8.1.2 Transfreq algorithm

In this chapter we introduce *transfreq*, a method to automatically compute TF from theta to alpha band when only resting-state EEG data are available. *Transfreq* relies on a rationale similar to that of Klimesch's method. Namely, TF is defined as the intersection between two spectral profiles differing in their content within the alpha and theta bands. However, with respect to Klimesch's method, such profiles are computed by exploiting the fact that alpha and theta activities are not uniformly expressed across the different EEG channels. In fact, some channels present high alpha activity (typically, channels above the occipital lobe), whereas others show lower alpha and higher theta activities (typically, channels corresponding to tem-

poral and frontal brain areas) (Klimesch, 1996; Nunez et al., 2001). Consequently, two groups of channels can be identified: the first group includes channels characterised by a preponderant alpha activity (this group plays a role analogous to the one of EEG data measured at rest in Klimesch's method); the second group includes channels showing preponderant theta activity and limited alpha activity (this second group plays a role analogous to the one of the task-evoked EEG recordings in Klimesch's method).

The *transfreq* pipeline is schematically illustrated by Figure 8.1B and Algorithm 2. In detail, for each EEG channel the normalised power spectrum is computed as in equation (8.1), that is

$$\widetilde{P}_i(f) = \frac{P_i(f)}{\sum_f P_i(f)}, \qquad \forall i \in \{1, \ldots, N\}. \tag{8.3}$$

TF is determined through the following iterative procedure.

(i) Set an initial value for the alpha and theta frequency-bands. Specifically, the alpha frequency-band is identified as a 2 Hz range centred on the IAP, which is defined as the frequency where the power spectrum averaged over all sensors peaks; the theta frequency-band is set equal to $[5, 7]$ Hz, or to $[\text{IAP} - 3,\ \text{IAP} - 1]$ Hz if the previous interval overlaps with the alpha frequency-band.

(ii) Compute, for each channel, the alpha and theta coefficients by averaging the normalised power spectrum $\widetilde{P}_i$ over the corresponding frequency band.

(iii) Apply a clustering algorithm to identify two groups of channels based on the alpha and theta coefficients. The channels in the first group, denoted as G_θ, will be characterised by low alpha and high theta activities, while the channels in the second group, G_α, will be characterised by high alpha and low theta activities. Two spectral profiles are thus obtained through a weighted average of the power spectra over the two groups, that is

$$S_\theta(f) = \frac{1}{\sum_{i \in G_\theta} w_i^\theta} \sum_{i \in G_\theta} w_i^\theta \, \widetilde{P}_i(f) \quad \text{and} \quad S_\alpha(f) = \frac{1}{\sum_{i \in G_\alpha} w_i^\alpha} \sum_{i \in G_\alpha} w_i^\alpha \, \widetilde{P}_i(f), \tag{8.4}$$

where w_i^θ and w_i^α are the theta and alpha coefficients for channel i, respectively.

(iv) Define a first estimate of TF as the highest frequency before the IAP at which S_θ and S_α intersect.

(v) Use the value of TF computed in (iv) to define new, more accurate, alpha and theta frequency bands, set equal to $[\max\{IAP - 1, TF\}, IAP + 1]$ and

$[TF-3, TF-1]$, respectively. Such a choice guarantees the intervals to be fully characterised by alpha and theta activation. Indeed, we chose narrower bands with respect to the classic 4 Hz ranges defined in the literature (Bazanova and Vernon, 2014; Klimesch, 1999) and we impose at least a 1 Hz separation between the intervals.

Steps (ii)-(v) are iterated until a desired level of accuracy is reached, quantified as the difference between two consecutive estimates of TF. The desired level of accuracy is set equal to the highest value between 0.1 Hz and the frequency resolution Δ_f. The rationale behind this choice is that 0.1 Hz is an acceptable error when computing TF. However, if the frequency resolution is lower (i.e $\Delta_f > 0.1$ Hz), setting the desired level of accuracy to 0.1 Hz would be the same as setting it to 0, which is a too strong requirement; therefore in such cases the level of accuracy is set equal to the frequency resolution.

We point out that the effectiveness of *transfreq* depends on the clustering procedure used to define the two groups of channels G_θ and G_α. In *transfreq* we have implemented four different algorithms, described in the next sub-sections.

Algorithm 2: *transfreq* core algorithm

Input: Resting-state EEG data recorded by N sensors
Output: TF
Compute and normalise sensors power spectra as in Eq. (8.3)
Initialise theta and alpha frequency bands
$\varepsilon := |\mathrm{TF}_{\mathrm{new}} - \mathrm{TF}_{\mathrm{old}}| = +\infty$
while $\varepsilon \geq \mathrm{toll}$ **do**
    Compute alpha and theta coefficients, w_i^α, w_i^θ, $i = 1, \ldots, N$
    Define channel groups, G_θ and G_α, through a clustering method
    Update TF
    Update ε
    Update theta and alpha frequency bands

Clustering method 1: 1D thresholding

The first clustering method implemented in *transfreq* is based on the ratio between the alpha and theta coefficients computed for each channel. In fact, channels with a low value of such alpha-to-theta ratio are characterised by low alpha and high theta activities, whereas channels with a high value are characterised by high alpha and low theta activities. The first group of channels, G_θ, is thus defined by the four channels showing the lowest values of the alpha-to-theta ratio, while the second group, G_α, is defined by the four channels showing the highest values of

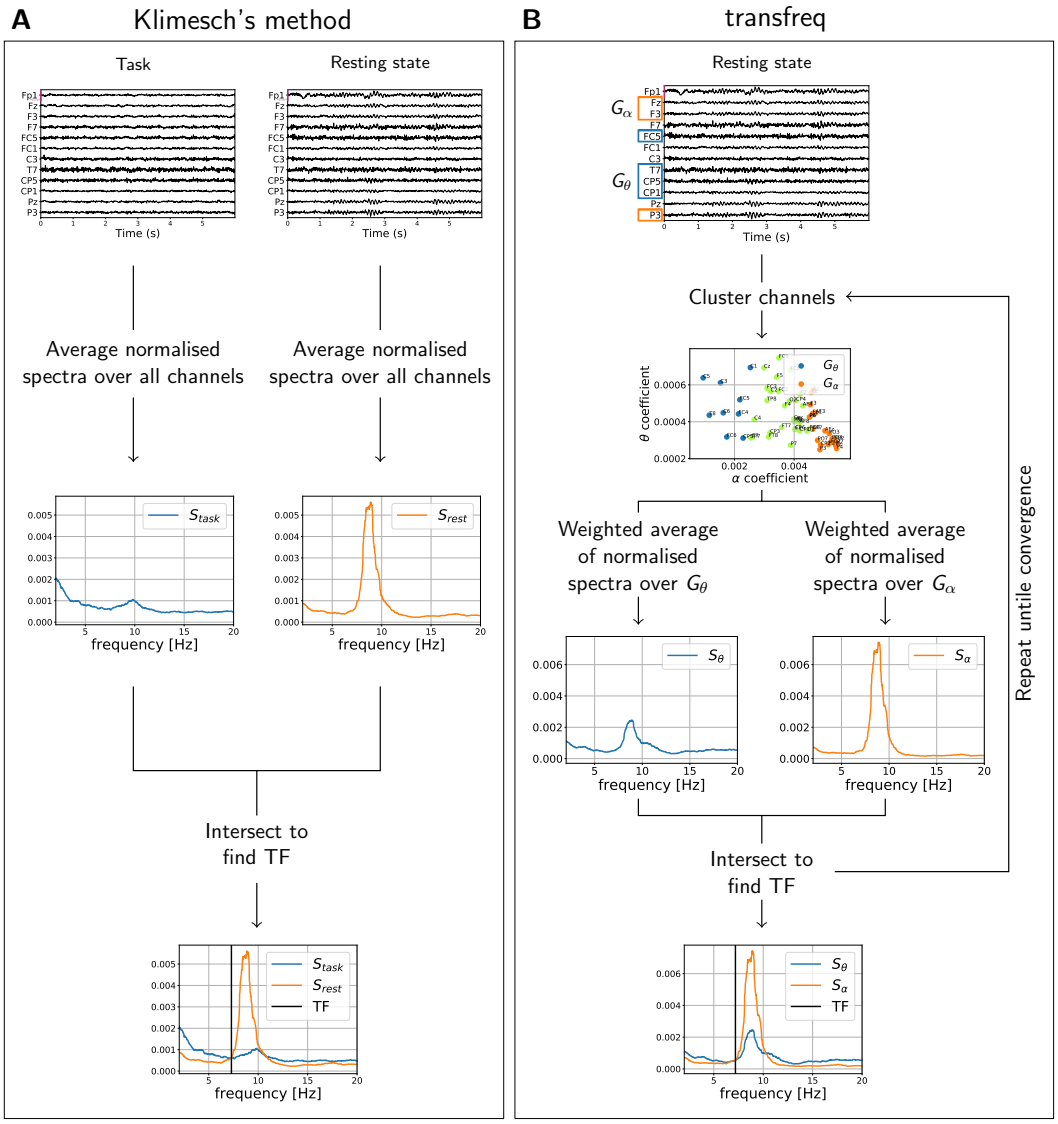

Figure 8.1: Comparison between the pipelines of the classic Kilmesch's method (A) and of *transfreq* (B).

the same ratio. A visual representation of this approach on a representative data set can be seen in Figure 8.2A. In *transfreq*, the number of channels in each group has been set equal to 4 after computing and visually inspecting the results for different values of such a parameter. In fact, the overall behaviour of the algorithm was similar across the different tested values.

Clustering method 2: 1D mean-shift

One drawback of the previous approach is the need to heuristically set the number of channels within the two groups G_α and G_θ. To overcome such a limitation, we implemented a second clustering approach where the Mean Shift algorithm (Comaniciu and Meer, 2002) is used to cluster the EEG sensors with respect to the ratio between the alpha and theta coefficients computed, for each channel, as described in the previous sub-section. To this end we used the MeanShift function available within the Python package Scikit Learn (Pedregosa et al., 2011) that also automatically determines the number of clusters. G_θ is then defined equal to the cluster containing the channel with the lowest value of the alpha-to-theta ratio, while G_α is set equal to the cluster containing the channel with the highest value of the same ratio. A visual representation of this approach on a representative data set can be seen in Figure 8.2B.

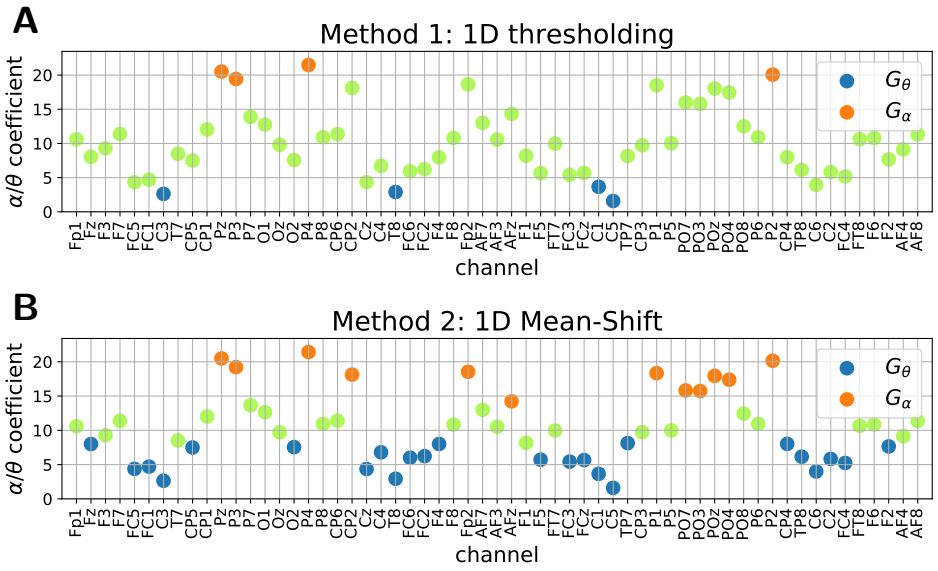

Figure 8.2: Performance illustration of the 1D clustering approaches thresholding (A) and mean-shift (B). Both panels show the value of the ratio between alpha and theta coefficients as function of the EEG sensors. Channels that belong to G_θ and G_α are represented as blue and orange dots, respectively. In *transfreq*, the remaining channels (greed dots) are excluded from the subsequent analysis.

Clustering method 3: 2D k-means

Both approaches described in the previous sub-sections rely on 1-dimensional clustering techniques that use the ratio between the alpha and theta coefficients as feature. In the third approach implemented in *transfreq* we exploited the k-means

algorithm (Lloyd, 1982) to cluster the EEG sensors by using the alpha and theta coefficients as two distinct features. To this end, we used the KMeans function within the Python package Scikit Learn (Pedregosa et al., 2011). The number of clusters to generate is set equal to 2. Then G_α is defined as the cluster whose centroid shows the highest value of the alpha coefficient, while the other cluster defines G_θ. As illustrated in Figure 8.3A, channels belonging to G_α (orange dots) typically present a higher alpha coefficient and a lower theta coefficient than the other ones (blue dots).

Clustering method 4: 2D adjusted k-means

The fourth clustering approach implemented in *transfreq* takes as input the two sensors groups, G_α and G_θ, computed using the k-means algorithm as described in the previous sub-section. However, the two groups are now adjusted so that only sensors showing the highest inter-cluster difference in terms of the alpha and theta coefficient values are retained. To this end, as illustrated in Figure 8.3B, we removed from G_α and G_θ all points laying between the two lines that pass through the centroids and are perpendicular to the segment connecting the two centroids.

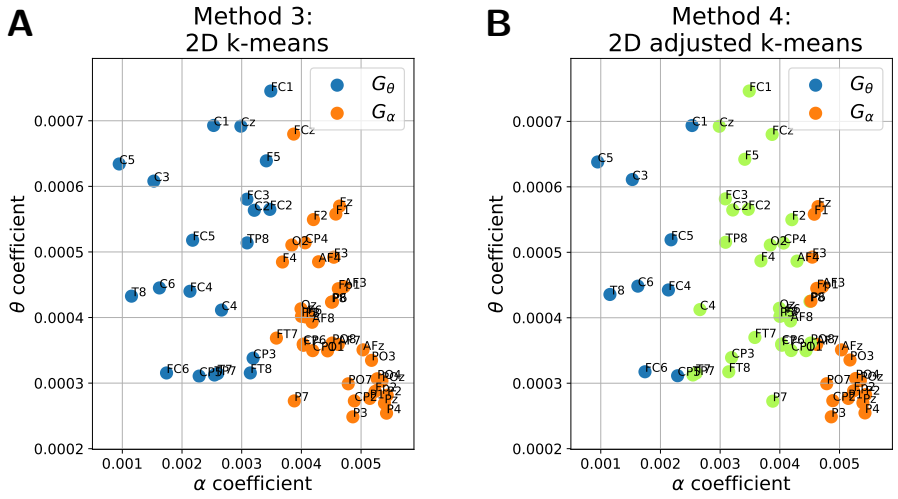

Figure 8.3: Performance illustration of the 2D clustering approaches k-means (A) and adjusted k-means (B). Both panels show the value of the theta coefficients on the y-axis and that of the alpha coefficients on the x-axis. Channels that belong to G_θ and G_α are represented as blue and orange dots, respectively. In *transfreq*, the remaining channels (green dots) are excluded from the subsequent analysis.

8.1.3 Software architecture

The approach described in the previous section is implemented in the publicly available Python library *transfreq* (https://elisabettavallarino.github.io/transfreq/). As shown in Table 8.1, *transfreq* comprises two modules: a set of three operative functions, that allow the estimation of TF either with the classic Klimesch's method or with our approach, and a set of six functions to visualise the results.

Module 1: operative functions

All the operative functions require in input the power spectra of the recorded EEG data. These power spectra have to be provided as matrices of size $N \times F$, where N is the number of EEG sensors and F is the number of frequencies in which the power spectra are evaluated.

The function *compute_transfreq* implements the iterative procedure described in Algorithm 2. Customised estimation of the transition frequency may be obtained through the function *compute_transfreq_manual* by providing two predefined groups of channels G_α and G_θ. In this case, TF is computed by looking at the intersections between the corresponding spectral profiles S_α and S_θ. Both functions return a dedicated dictionary, called *tfbox* in Table 8.1, that contains: (i) the results of the clustering procedure, together with the alpha and theta coefficients, w_i^α and w_i^θ, associated with each sensor; (ii) the name of the employed algorithm; (iii) the estimated value of TF.

In order to provide an exhaustive toolbox for computing the theta-to-alpha TF we also implemented a function for the computation of TF with Klimesch's method. Such a function is named *compute_transfreq_Klimesch* and only returns the estimated value of TF.

Module 2: visualisation functions

As shown in Table 8.1, *transfreq* offers the users two functions to visualise features of the data provided in input, namely the normalised EEG power spectrum (function *plot_psds*) and the corresponding alpha and theta coefficients (function *plot_coefficients*).

Three other functions allow the user to visualise results from each step of our approach, that is: (i) the alpha and theta coefficients grouped according to the results of the clustering procedure (function *plot_clusters*); (ii) the corresponding channels group G_α and G_θ located on top of topographical maps (function *plot_channels*); (iii) the final estimated value of TF on top of the spectral profiles S_α and S_θ (function *plot_transfreq*). The function *plot_channels* makes use of the

Python package visbrain (Combrisson et al., 2019), and, in particular, we modified its function *TopoObj* to optimise it to our visualisation purpose.

Eventually, the function *plot_transfreq_klimesch* is dedicated to plot the value of TF estimated using the classic Klimesch's method.

Module 1: Operative functions		
Name	Description	Input
compute_transfreq	Computation of TF	rest PS
compute_transfreq_manual	Computation of TF (customised clusters)	rest PS; G_α; G_θ
compute_transfreq_klimesch	Computation of TF (Klimesch's method)	rest PS; task PS
Module 2: Visualisation functions		
Name	Description	Input
plot_psds	Normalised PS power spectrum	rest/task PS
plot_coefficients	α and θ coefficients or their ratio	rest/task PS
plot_clusters	Computed clusters	tfbox
plot_channels	G_α and G_θ on scalp	tfbox; channel locations
plot_transfreq	TF on top of S_α and S_θ	rest PS; tfbox
plot_transfreq_klimesch	TF on top of S_{rest} and S_{task}	rest and task PS; TF value

Table 8.1: Functions implemented within *transfreq*. The table provides the name of each function (first column), a short description of their purpose (second column), and the required input variables (third column). Here, rest PS and task PS stand for resting state and task-related EEG power spectrum, respectively; tfbox is a dedicated dictionary output of the operative functions. For some of the functions, an additional set of optional arguments may be passed by the user, such as predefined alpha and theta frequency-band, or the clustering approach to be used for defining G_α and G_θ. The full list of these additional parameters may be found in the package documentation.

8.1.4 Data

We validated *transfreq* by using two EEG data sets. The first one is an open-source data set, while the second one is an in-house data set we recorded in our lab. We used two different data sets to test the robustness of *transfreq* across data recorded in different experimental conditions.

Open-source data set

This data set contains EEG data available at OpenNeuro, a free and open platform for sharing neurophysiological data (Gorgolewski et al., 2017), at the accession number ds003490 (data set DOI doi:10.18112/openneuro.ds003490.v1.1.0). Data comprise both resting state and stimulus auditory oddball EEG recordings, sampled at 500 Hz, from 25 Parkinson's patients and 25 matched controls. For Parkinson's patients, two sessions are available, while for healthy controls one session is available. More information about this data set can be found in the paper by Cavanagh and colleagues (Cavanagh et al., 2018). For each subject and for each session we selected two minutes of recording under stimulation, and one minute resting state eyes-closed recording.

In-house data set for validation

This data set included 80 traces acquired during a previous multicenter study, namely the Innovative Medicines Initiative PharmaCog project: a European ADNI study (Galluzzi et al., 2016). This study aimed at investigating multiple biomarkers in a population with amnesic mild cognitive impairment (MCI), by following subjects for three years or until conversion to dementia. EEG was repeatedly acquired every 6 months; thus the 80 traces refer to 16 subjects undergoing EEG from one to 7 times. The 16 subjects (8 males, 8 females, age range 55-82 years, mean: 70$\pm$6 years; mini-mental state examination score range at first evaluation: 23-30, mean: 26.5$\pm$2.13) included 11 who converted to Alzheimer disease dementia during the follow-up, 2 subjects who convert to frontotemporal dementia, and 3 subjects who remained in an MCI stage or even reverted to a normal condition.
For the analysis we selected two and a half minutes of resting state eyes-closed recording and two and a half minutes of resting-state eyes-opened recording, where data showed a de-synchronisation of the alpha rhythm (Gómez-Ramírez et al., 2017). Both data were recorded with a sampling frequency of 512 Hz.

8.1.5 Data analysis

The recorded time series from both data sets were first pre-processed using the MNE-Python analysis package (Gramfort et al., 2013). For each subject and for each condition, the EEG recording was filtered between 2 and 50 Hz, while bad segments were manually removed and bad channels were interpolated. Then, data were re-referenced using average reference (Offner, 1950) and Independent Component Analysis (ICA) (Jutten and Herault, 1991) was applied for artefact and noise removal. Remaining bad segments were automatically rejected by using the autoreject Python package (Jas et al., 2017). Finally, the pre-processed EEG recordings were visually inspected by experts and discarded when they did not present a visible alpha peak. In this way, in the open-source data set we excluded the first session of four subjects and both sessions of one subject. In the in-house data set all sessions involving four subjects were excluded from the analysis.

Power spectra were computed in the 2-30 Hz range with the multitapers method (Thomson, 1982). With such a method the frequency resolution of the power spectra depends on the time resolution and duration of the EEG recordings. In order to apply the Klimesch's method, the spectral profiles under the two conditions (rest and task) need to have the same frequency resolution. To this end the length of both recordings was set equal to the length of the shortest one. Average duration of the EEG recordings from the open source data set was 58 s, while average duration of the EEG recordings from the in-house data set was 134 s. Afterwards, TF was computed using both the Klimesch's method and *transfreq*. Finally, the results

obtained with Klimesch's method were visually inspected by experts and excluded when the method did not provide reliable results. Exclusion criteria comprised cases in which the two spectral profiles did not intersect as well as cases in which the two spectral profiles overlapped. This process led to the exclusion of 19 EEG recordings from the open-source data set and 14 EEG recordings from the in-house data set. Therefore, the analysis to validate *transfreq* was performed on a total of 50 EEG recordings from the open-source data set and 45 from the in-house data set.

8.2 Results

8.2.1 Transfreq performances on an illustrative example.

We first tested the performances of *transfreq* when applied to an illustrative example picked up from the open-source data set. Figure 8.4 and Figure 8.5 show the results provided by the tool when the four different clustering algorithms were applied. For all algorithms, the resulting G_α mainly contained channels that lie over the occipital lobe and showed a higher alpha activity than the channels in G_θ.

When 1D thresholding is used, both G_α and G_θ contain a pre-defined number of sensors (4 in this case). Instead, the other methods automatically estimate the size of G_θ and G_α, and thus the two groups may contain a different number of channels.

While with the 2D k-means G_α and G_θ span all the EEG channels, the 2D adjusted k-means starts from the two groups defined by using k-means and selects only the channels showing a high inter-cluster difference. Specifically, as illustrated in Figure 8.5, the channels in G_α (G_θ) showed both a high alpha (theta) activity and a low theta (alpha) activity.

Depending on the selected clustering approach, *transfreq* may return different estimates for TF, as illustrated in Figure 8.6. With this subject, the value of TF estimated by the Klimesch's method was 7.29 Hz, while transfreq returned 7.38 Hz with 1D thresholding, 7.39 Hz with 1D mean-shift, 7.22 Hz with 2D k-means, and 7.19 Hz with 2D adjusted k-means.

8.2.2 Validation on the open-source data set

As illustrated in Figure 8.7, for most subjects in the open-source data set, the difference Δ_{TF} between the TF value estimated by *transfreq* and by Klimesch's method was in absolute value below 1 Hz. Specifically, $|\Delta_{TF}|$ was lower than 1 Hz for 82% of the subjects when 1D thresholding was employed for clustering, 76% in the case of 1D mean-shift, 82% for 2D k-means, and 88% for 2D adjusted

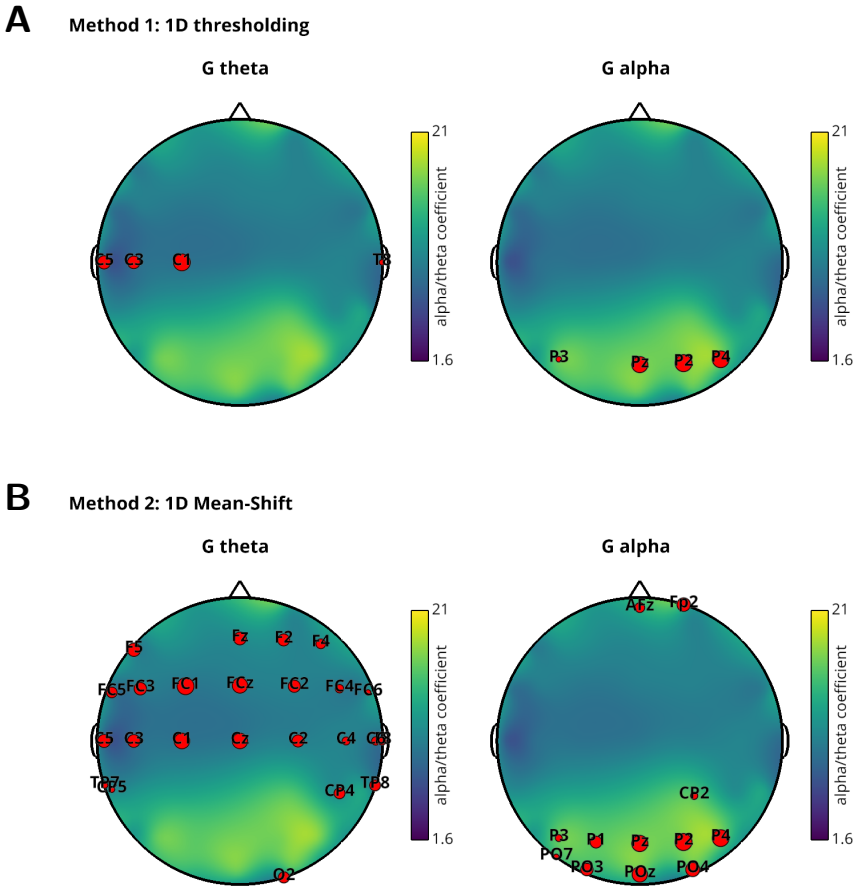

Figure 8.4: Location on the scalp of channels in G_θ (left column) and G_α (right column) for one representative subject from the open-source data set. Sensors have been clustered by using 1D thresholding (upper row) or 1D mean-shift (lower row). In each panel, red dots represent the selected channels and, in the background, the topographical map shows the value of the ratio between alpha and theta coefficients. For the sensors in G_θ, the size of the dots is proportional to the corresponding theta coefficient, w_i^θ, while for those in G_α the size is proportional to the alpha coefficient, w_i^α.

k-means. Figure 8.7 also shows that *transfreq* mainly estimated a lower value of TF than Klimesch's method. Since the lowest values of $|\Delta_{TF}|$ were obtained by clustering the EEG channels by means of the 2D adjusted k-means method, this is suggested as the default approach within *transfreq*.

8.2.3 Improvements of transfreq over the Klimesch's method

Klimesch's method relies on an event-related reduction of the alpha activity that may not occur in practical scenarios due, for example, to an incorrect execution of the task. Indeed, as shown in Figure 8.8, for some of the subjects in the

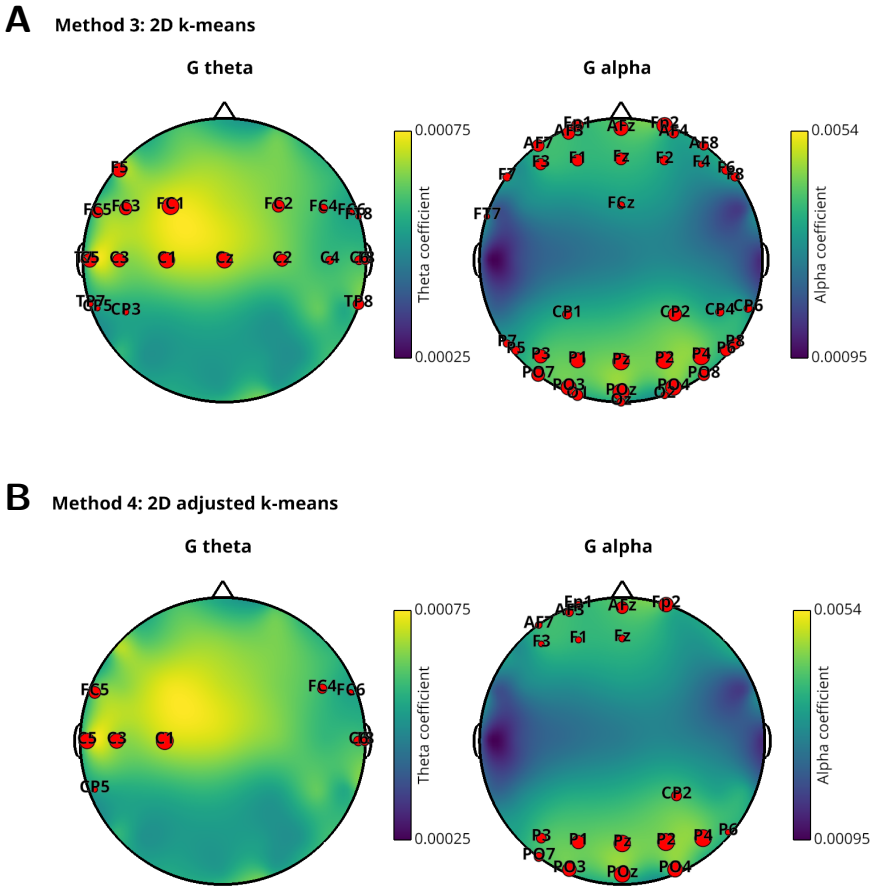

Figure 8.5: Location on the scalp of channels in G_θ (left column) and G_α (right column) for one representative subject from the open-source data set. Sensors have been clustered by using 2D k-means (upper row) or 2D adjusted k-means (lower row). As in Figure 8.4, the red dots depict the selected channels. In the two panels on the left side, referring to G_θ, the size of the sensors and the background topographical maps represent the theta coefficient, w_i^θ. Instead, the two panels on the right side, referring to, G_α, show the alpha coefficients w_i^α.

considered data sets the spectral profiles S_{task} and S_{rest} perfectly overlapped and thus Klimesch's method failed in computing TF.

On the other hand, some subjects may show an event-related modulation of the alpha frequency (Haegens et al., 2014). As represented in Figure 8.9, in this case the shift of the alpha peak in S_{task} prevented the use of Klimesch's method because the two spectral profiles S_{task} and S_{rest} did not intersect in the range [0, 10] Hz.

Transfreq overcomes such limitations of Klimesch's method, since it utilises just resting state recordings, and relies on the selection of specific channels that actually present the desired features, i.e. channels with a low (high) alpha and a

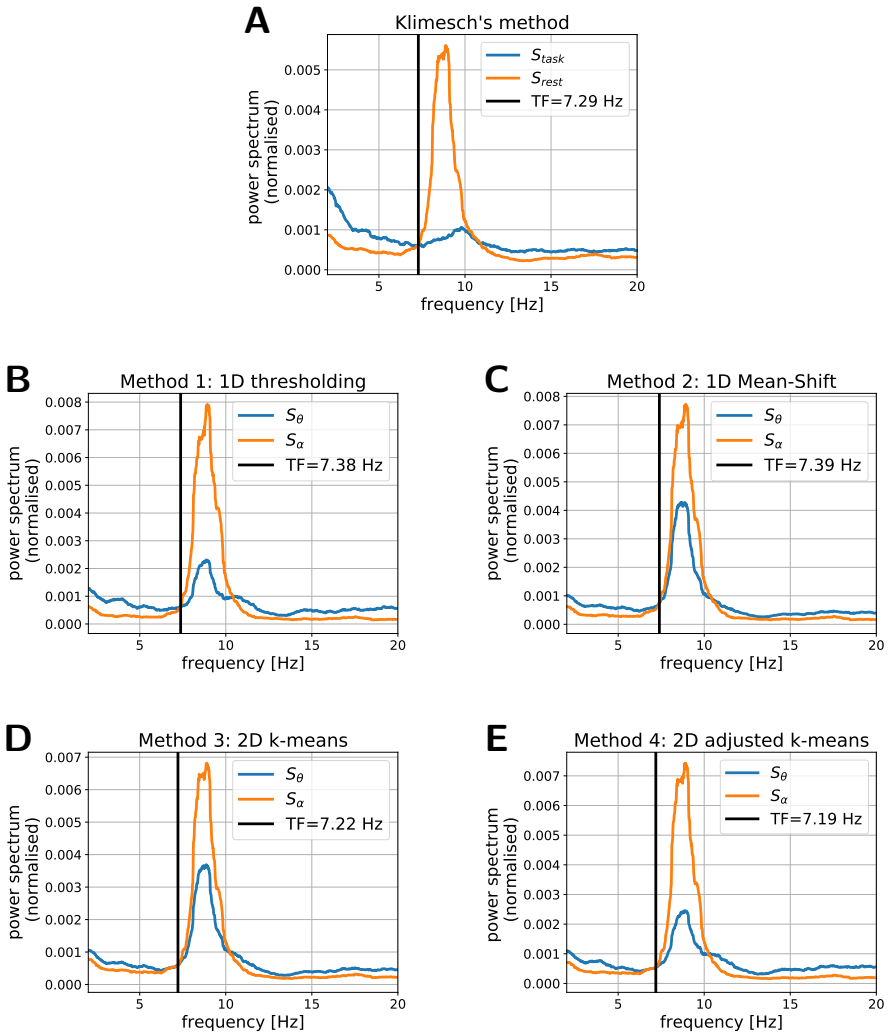

Figure 8.6: TFs estimated with Klimesch's method and with *transfreq* by means of the four clustering methods for one representative subject from the open-source data set. In each panel: the blue line depicts the spectral profile with low alpha and high theta activation, namely S_{task} in Klimesch's method and S_θ in *transfreq*; the orange line shows the spectral profile with high alpha and low theta activation, namely S_{rest} in Klimesch's method and S_α in *transfreq*; the red vertical line indicates the estimated value of TF.

high (low) theta activity for G_θ (G_α). Indeed, as shown in Figures 8.8 and 8.9, right panels, in both scenarios previously described *transfreq* estimated a reliable value for TF. More in general, a visual inspection of the results revealed that Klimesch's method provided an untrustworthy value of TF for 27% of the EEG sessions of the open-source data set, while with *transfreq* only 6% of the results were unreliable.

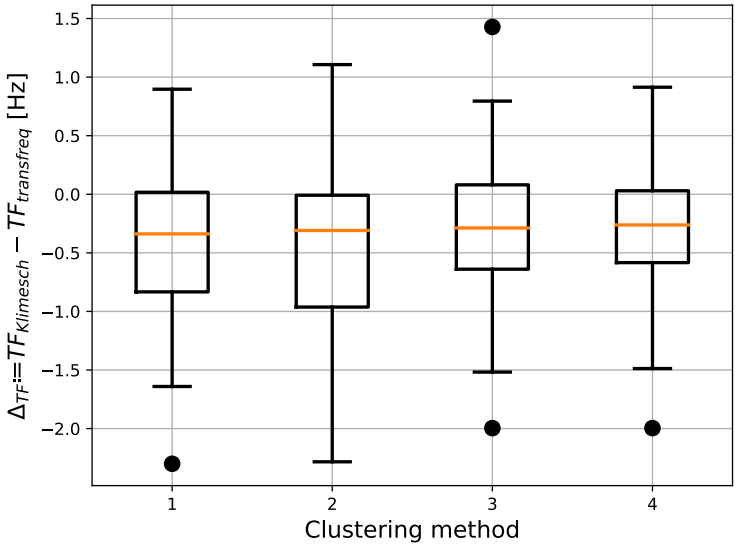

Figure 8.7: Difference between TFs estimated with Klimesch's method ($TF_{Klimesch}$) and with *transfreq* ($TF_{transfreq}$) over the open-source data set. Each boxplot depicts the results obtained when a different clustering approach is used to define the channels group G_θ and G_α, namely: 1D thresholding (Method 1); 1D mean-shift (Method 2); 2D k-means (Method 3); and 2D adjusted k-means (Method 4).

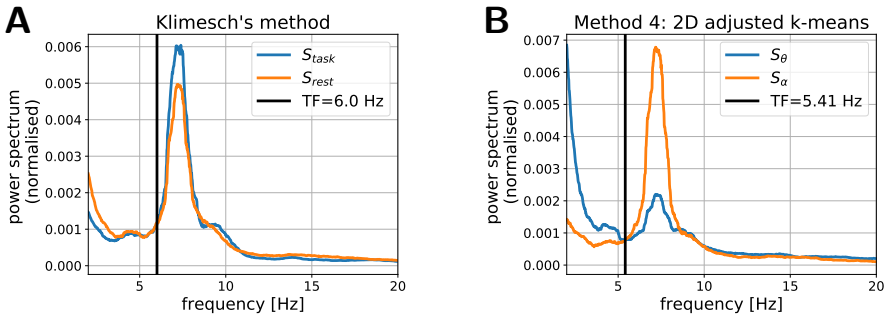

Figure 8.8: Example where Klimesch's method provides unreliable estimate of TF because event-related, S_{task}, and resting-state, S_{rest}, spectral profiles overlap. (A) Results obtained with the Klimesch's method. (B) Results obtained with *transfreq* by using 2D adjusted k-means to compute the spectral profiles S_θ and S_α

8.2.4 Validation on the in-house data set

Figure 8.10 shows that the results obtained by applying *transfreq* on the in-house data set are similar to those obtained on the open-source one. Specifically, *transfreq* generally returned higher estimates of TF with respect to Klimesch's method. However, the absolute value of the difference between the values estimated with the two methods was below 1 Hz for 67% of the subject when 1D

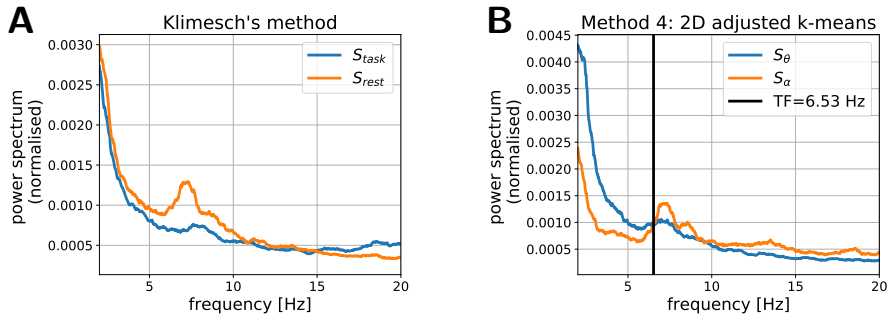

Figure 8.9: Example where Klimesch's method cannot be applied because event-related, S_{task}, and resting-state, S_{rest}, spectral profiles do not intersect in a reasonable frequency range. (A) Results obtained with the Klimesch's method. An event-related shift of the alpha–peak towards higher frequency can be seen in S_{task}. (B) Results obtained with *transfreq* by using 2D adjusted k-means to compute the spectral profiles S_θ and S_α

thresholding was applied, 58% with 1D mean-shift, 73% with 2D k-means, and 62% with 2D adjusted k-means.

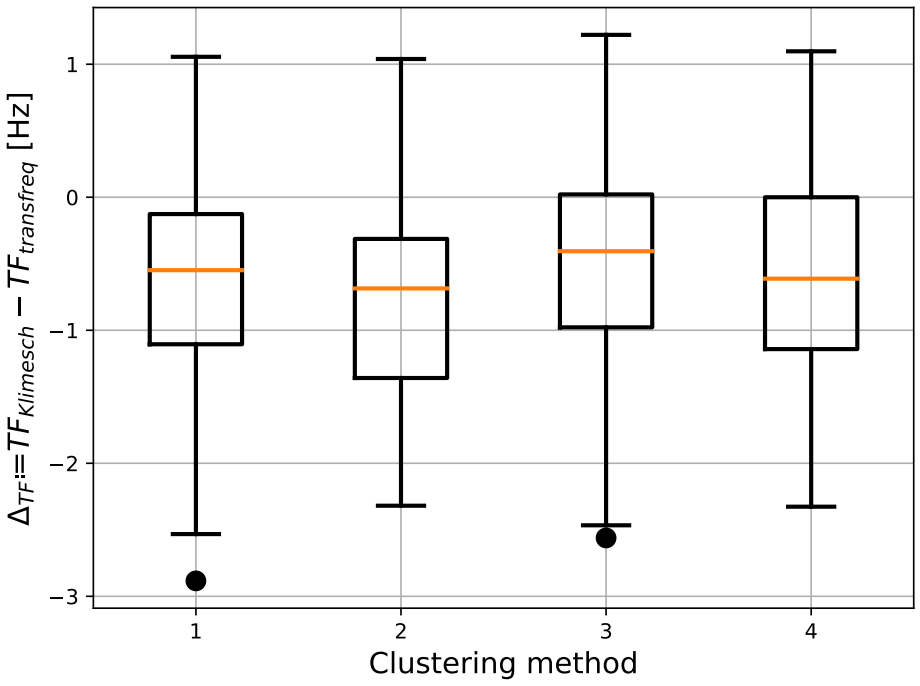

Figure 8.10: Difference between TFs estimated with Klimesch's method ($TF_{Klimesch}$) and with *transfreq* ($TF_{transfreq}$) over the in-house data set. As in Figure 8.7 each boxplot depicts the results obtained when a different clustering approach is used to define G_θ and G_α, namely: 1D thresholding (Method 1); 1D mean-shift (Method 2); 2D k-means (Method 3); and 2D adjusted k-means (Method 4).

8.2.5 Proportional bias in estimating TF

We performed a Bland-Altman analysis (Bland and Altman, 1986) to assess proportional bias in the estimates of TF. Figure 8.11 shows the analysis for the open-source (panel A) and the in-house data sets (panel B), computed on the TF values provided by *transfreq* with adjusted k-means. With the open source data set no proportional bias was present; to confirm this, we computed a regression line and the p-value (null hypothesis: slope equal to zero). Differently, the results with the in-house data set showed a statistically significant ($p < 0.001$) proportional bias. Specifically, Figure 8.11B shows that *transfreq* tends to overestimate TF at higher frequencies (> 8 Hz).

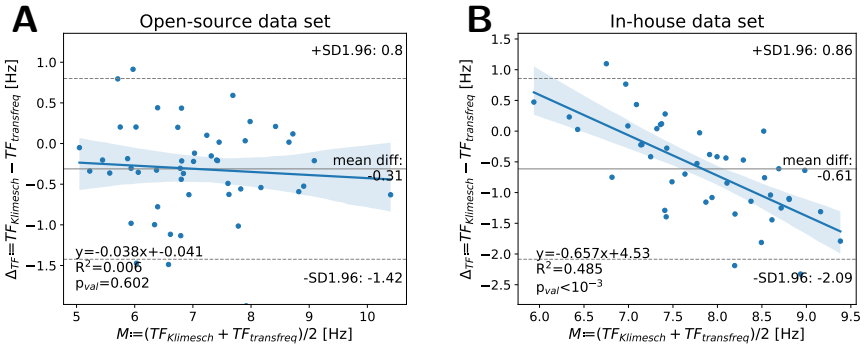

Figure 8.11: Bland-Altman plot between Klimesch's method and transfreq with 2D adjusted k-means for the open-source (A) and the in-house (B) data sets. Grey plain and dotted lines show mean bias and corresponding 95% confidence limits, respectively. Proportional bias regression lines are depicted as blue lines, and the corresponding equations are embedded in the lower-left corner of each panel together with the coefficient of determination (R^2) and the p-value (p_{val}) computed testing the null hypothesis that the slope is equal to zero.

8.3 Discussion

In this chapter we presented the work published in (Vallarino et al., 2021b). Specifically, we described *transfreq*, an open-source Python tool for the computation of the individual transition frequency from theta to alpha band using only one resting-state EEG recording.

A classic approach to compute the theta-to-alpha TF is that proposed by Klimesch (Klimesch, 1999), which requires the power spectrum of two EEG time series, one recorded while the subject is resting and one while the subject is performing a task. However, in studies involving e.g. patients affected by neurodegenerative diseases, the subject may experiment difficulties in performing the required task and thus the corresponding event-related recording may imply difficult interpretation. On

the contrary, *transfreq* uses only resting state data, which reduces the information at disposal but increases the scenario in which *transfreq* can be applied.

By comparing with the results obtained with the classic Klimesch's method on two independent data sets, we demonstrated that *transfreq* returns reliable estimates of TF. Indeed, with the best combination of input parameters, the absolute value of the difference between the value of TF estimated with *transfreq* and with Klimesch's method was below 1 Hz for 88% of the analysed data in the open-source data set, and for 73% for our in-house data set (throughout this chapter Klimesch's method was assumed as ground truth). The differences in the performance over the two data sets may be partially due to the noisier nature of the in-house data set. Moreover, a visual inspection of the estimated values of TF showed that the cases in which the spectral profiles, S_θ and S_α, obtained with *transfreq* intersected ambiguously were considerably less than the cases in which the hypothesis of Klimesch's method on S_{task} and S_{rest} failed.

Among the four approaches implemented in *transfreq* to realise the clustering step, the adjusted k-means showed the best performances in the open-source data set while in the in-house data set the k-means algorithm performed the best. This is probably due to the fact that these algorithms realise a more accurate selection of the sensors within the two groups G_θ and G_α.

However, all four approaches tend to overestimate the value of TF with respect to Klimesch's method. Specifically, the Band-Altman analysis for the in-house data set show that this behaviour seems to be more pronounced for higher values of TF ($>$ 8 Hz). This difference between *transfreq* and Klimesch's method is probably related to the fact that only resting-state data are used in *transfreq*; as a consequence also channels in G_θ may present a fingerprint of the alpha activity.

The two data sets considered in this chapter are EEG data. Future studies may be devoted to investigate a possible extension to MEG data.

Finally, future efforts will be devoted to better compare *transfreq* and the classic Klimesch's method, especially in those scenarios where they return different estimates of TF. To this end, future studies will be devoted to correlate both Klimesch's and *transfreq*'s results with clinical variables and biomarkers.

Conclusions

In this thesis we investigated the problem of optimally estimating brain functional connectivity from magneto/electro-encephalographic (MEEG) data, i.e. from indirect measurements of the magnetic field outside the head and the scalp potential produced by the tiny currents that naturally flow inside the brain and that characterise its activity. With the help of stochastic processes theory we were able to model the time courses associated with sensor level MEEG recordings and brain activity, and to quantify functional connectivity with a bunch of connectivity metrics. Specifically, we focused on connectivity metrics computed in the frequency domain starting from the cross-power spectrum of the source time courses. On the other hand, inverse problems theory provided us with different methods to estimate brain activity time courses from the corresponding MEEG recordings.

First, we focused on a standard pipeline for connectivity estimation, which relies on a two-step process. During the first step the time courses associated with brain activity are estimated by solving the MEEG inverse problem by means of a regularisation technique. Then, during the second step connectivity is computed among the estimated time courses. The regularisation technique employed in the first step requires to set a regularisation parameter which will, of course, influence the subsequent connectivity estimation. Motivated by empirical studies (Hincapié et al., 2016), the core of this thesis was to investigate the role of the regularisation parameter in the two-step process. Chapters 4, 5 and 6 were dedicated to this. Specifically, in Chapter 4 we focused on two regularisation techniques, namely truncated Singular Value Decomposition (tSVD) and Tikhonov regularisation, better known as Minimum Norm Estimate (MNE) in the neuroscientific community, and we analytically compared the regularisation parameters providing the optimal neural activity, $\lambda^*_{\mathbf{x}}$, and cross-power spectrum, $\lambda^*_{\mathbf{S}}$, estimates. By assuming both brain activity and measurement noise to be realisations of white Gaussian processes, we found that, when tSVD is employed, the two parameters coincide (i.e. $\lambda^*_{\mathbf{x}} = \lambda^*_{\mathbf{S}}$), whereas, in the case of Tikhonov regularisation, the two parameters are different, precisely it holds $\lambda^*_{\mathbf{S}} < \frac{\lambda^*_{\mathbf{x}}}{2}$, meaning that less regularisation is needed

for the cross-power spectrum estimation. In Chapter 5, we relaxed the strong hypothesis of white Gaussian process for brain activity, which was essential for the analytical computations, and we numerically investigated the same problem. Still, we quantified connectivity through the cross-power spectrum and we focused on Tikhonov regularisation. We simulated several sensor level MEG configurations and for each of them we numerically computed the optimal parameters $\lambda^*_{\mathbf{X}}$ and $\lambda^*_{\mathbf{S}}$. The results confirmed the findings of Chapter 4. Moreover, by quantifying the spectral complexity of brain activity by a proper scalar coefficient, we found that $\lambda^*_{\mathbf{S}}$ gets even smaller for increasing values of such a coefficient. This latter result was supported by an analytical investigation of the signal-to-noise ratios associated, on one hand, with the MEG linear model ($\text{SNR}^{\mathbf{X}}$), on the other hand, with the model that directly links the source level with the sensor level cross-power spectra ($\text{SNR}^{\mathbf{S}}$). Indeed, for same values of $\text{SNR}^{\mathbf{X}}$, for increasing spectral complexity coefficients, $\text{SNR}^{\mathbf{S}}$ gets smaller, thus less regularisation is needed for the cross-power spectrum estimation. Finally, in Chapter 6, we still focused on Tikhonov regularisation, however we widen the set of connectivity metrics and we simulated more complex and realistic brain activity configurations; then, we numerically computed the optimal regularisation parameters. The results confirmed that $\lambda^*_{\mathbf{C}} < \frac{\lambda^*_{\mathbf{X}}}{2}$, being $\lambda^*_{\mathbf{C}}$ the optimal parameter for connectivity estimation.

The two-step approach has the disadvantage that the unavoidable errors committed in the first step inevitably propagate in the second step. Moreover Tikhonov regularisation promotes smoothness on the solution which is not desirable in the MEEG context. To overcame these two problems, in Chapter 7 we proposed a one-step approach which allows to estimate source space functional connectivity directly from sensor space connectivity. In addition, we replaced Tikhonov regularisation with ℓ_1 regularisation, which promotes sparsity on the solution. Specifically, after defining a new linear model that links source space with sensor level cross-power spectra, we simulated two MEG configurations and we estimated the cross-power spectrum by exploiting both the two-step and the one-step approaches. The results showed that the combination of the one-step approach and ℓ_1 regularisation outperforms the classic two-step approach plus Tikhonov regularisation. Of course, the simulations need to be widened in order to strengthen the results; future works will be devoted to this.

It is worth mentioning that the regularisation methods employed in both the two-step and the one-step approaches require to set a proper regularisation parameter. In this thesis, working in simulation contexts, we were always able to set such a parameter to obtain the best possible estimates. However in experimental settings this is not feasible, therefore there is need to determine a proper criterion

to set it. This is one of the main open issues of this thesis. Future works will be devoted to this and they may imply the implementation of a learning algorithm to automatically infer the regularisation parameter from the MEEG data.

It is also to be noted that this thesis focuses on comparing different pipelines to estimate functional connectivity and identifying the optimal one. However, it does not take into account other transversal issues, such as problems related to the estimation of connectivity metrics from finite data, or the effect of non stationarity of the data, or also the importance of considering the aperiodic components of the neural signals. These issues have been investigated in a number of papers (Donoghue et al., 2020; Sommariva et al., 2019) and are not negligible. It would be interesting to interconnect the results of these papers with the finding presented in this thesis; future works may be devoted to this. Additionally, we have not discussed the effect of source leakage on connectivity estimate when the one-step approach is employed. Indeed, several studies have investigated this problem when a two-step procedure is used to estimate neural time courses (Anzolin et al., 2019; Palva et al., 2018; Wang et al., 2018), however it would be interesting to evaluate the effect of source leakage on a one-step connectivity estimate, and to see whether the one-step approach might reduce its impact.

In Chapter 8, we presented *transfreq*, a Python package for the automated computation of the theta-to-alpha transition frequency (TF). A proper estimation of TF is of utmost importance to correctly define individual frequency bands, and therefore achieve reliable results during the analysis of MEEG data. Our package is freely downloadable and provides the scientists with a user-friendly tool. We proved the performance of our method on both an open source and on an in-house database and we showed that it is reliable by comparing it with a classic approach, namely Klimesch's method. Specifically, with the open-source data set, the absolute value of the difference between the TFs estimated with the two methods was below 1 Hz for 88% of subjects. With the in-house data set the percentage is 73%, however this lower value may be due to the noisier nature of the data.

Finally, future works will employ the results and the methods presented in this thesis in the field of neurodegenerative diseases. Specifically, the objective is to use features computed from the MEEG power spectra, such as the individual transition frequency, as well as connectivity networks to characterise different neurodegenerative disease, including Alzheimer, Parkinson and sleep disorders, with the final aim of finding biomarkers for their early detection.

Bibliography

Acebrón J A, Bonilla L L, Vicente C J P, Ritort F, and Spigler R. The kuramoto model: A simple paradigm for synchronization phenomena. *Reviews of modern physics*, 77(1):137, 2005.

Anzolin A and Astolfi L. Statistical causality in the EEG for the study of cognitive functions in healthy and pathological brains. *Rome: Sapienza University of Rome*, 2018.

Anzolin A, Presti P, Van De Steen F, Astolfi L, Haufe S, and Marinazzo D. Quantifying the effect of demixing approaches on directed connectivity estimated between reconstructed eeg sources. *Brain topography*, 32(4):655–674, 2019.

Astolfi L, Cincotti F, Mattia D, Marciani M G, Baccala L A, de Vico Fallani F, Salinari S, Ursino M, Zavaglia M, Ding L, et al. Comparison of different cortical connectivity estimators for high-resolution eeg recordings. *Human brain mapping*, 28(2):143–157, 2007.

Babiloni C, Miniussi C, Babiloni F, Carducci F, Cincotti F, Del Percio C, Sirello G, Fracassi C, Nobre A C, and Rossini P M. Sub-second "temporal attention" modulates alpha rhythms. a high-resolution EEG study. *Cognitive Brain Research*, 19(3):259–268, 2004.

Babiloni C, Del Percio C, Lizio R, Noce G, Cordone S, Lopez S, Soricelli A, Ferri R, Pascarelli M T, Nobili F, et al. Abnormalities of cortical neural synchronization mechanisms in subjects with mild cognitive impairment due to Alzheimer's and Parkinson's diseases: an EEG study. *Journal of Alzheimer's Disease*, 59(1): 339–358, 2017.

Backus G and Gilbert F. The resolving power of gross earth data. *Geophysical Journal International*, 16(2):169–205, 1968.

Bailey D L, Maisey M N, Townsend D W, and Valk P E. *Positron emission tomography*, volume 2. Springer, 2005.

Baillet S, Mosher J C, and Leahy R M. Electromagnetic brain mapping. *IEEE Signal processing magazine*, 18(6):14–30, 2001.

Bartlett M S. Periodogram analysis and continuous spectra. *Biometrika*, 37(1/2): 1–16, 1950.

Barzegaran E and Knyazeva M G. Functional connectivity analysis in eeg source space: the choice of method. *PloS one*, 12(7):e0181105, 2017.

Bastos A M and Schoffelen J M. A tutorial review of functional connectivity analysis methods and their interpretational pitfalls. *Frontiers in systems neuroscience*, 9:175, 2016.

Bazanova O and Vernon D. Interpreting EEG alpha activity. *Neuroscience & Biobehavioral Reviews*, 44:94–110, 2014.

Bear M, Connors B, and Paradiso M A. *Neuroscience: Exploring the Brain, Enhanced Edition: Exploring the Brain*. Jones & Bartlett Learning, 2020.

Beck A and Teboulle M. A fast iterative shrinkage-thresholding algorithm for linear inverse problems. *SIAM journal on imaging sciences*, 2(1):183–202, 2009.

Bendat J S and Piersol A G. *Random data: analysis and measurement procedures*, volume 729. John Wiley & Sons, 2011.

Bland J M and Altman D. Statistical methods for assessing agreement between two methods of clinical measurement. *The lancet*, 327(8476):307–310, 1986.

Bruña R, Maestú F, and Pereda E. Phase locking value revisited: teaching new tricks to an old dog. *Journal of neural engineering*, 15(5):056011, 2018.

Cabral J, Luckhoo H, Woolrich M, Joensson M, Mohseni H, Baker A, Kringelbach M L, and Deco G. Exploring mechanisms of spontaneous functional connectivity in meg: how delayed network interactions lead to structured amplitude envelopes of band-pass filtered oscillations. *Neuroimage*, 90:423–435, 2014.

Cavanagh J F, Kumar P, Mueller A A, Richardson S P, and Mueen A. Diminished EEG habituation to novel events effectively classifies Parkinson's patients. *Clinical Neurophysiology*, 129(2):409–418, 2018.

Chella F, Marzetti L, Stenroos M, Parkkonen L, Ilmoniemi R J, Romani G L, and Pizzella V. The impact of improved MEG–MRI co-registration on MEG connectivity analysis. *Neuroimage*, 197:354–367, 2019.

Cheung B L P, Riedner B A, Tononi G, and Van Veen B D. Estimation of cortical connectivity from EEG using state-space models. *IEEE Transactions on Biomedical engineering*, 57(9):2122–2134, 2010.

Comaniciu D and Meer P. Mean shift: A robust approach toward feature space analysis. *IEEE Transactions on pattern analysis and machine intelligence*, 24 (5):603–619, 2002.

Combettes P L and Pesquet J C. Proximal splitting methods in signal processing. In *Fixed-point algorithms for inverse problems in science and engineering*, pages 185–212. Springer, 2011.

Combrisson E, Vallat R, O'Reilly C, Jas M, Pascarella A, Saive A l, Thiery T, Meunier D, Altukhov D, Lajnef T, et al. Visbrain: a multi-purpose GPU-accelerated open-source suite for multimodal brain data visualization. *Frontiers in Neuroinformatics*, 13:14, 2019.

Curtis H, Barnes N S, Odone R, and Gandola L. *Invito alla biologia*. Zanichelli, 1981.

Daubechies I, Defrise M, and De Mol C. An iterative thresholding algorithm for linear inverse problems with a sparsity constraint. *Communications on Pure and Applied Mathematics: A Journal Issued by the Courant Institute of Mathematical Sciences*, 57(11):1413–1457, 2004.

De Pasquale F, Della Penna S, Snyder A Z, Lewis C, Mantini D, Marzetti L, Belardinelli P, Ciancetta L, Pizzella V, Romani G L, et al. Temporal dynamics of spontaneous meg activity in brain networks. *Proceedings of the National Academy of Sciences*, 107(13):6040–6045, 2010.

de Peralta Menendez R G, Hauk O, Andino S G, Vogt H, and Michel C. Linear inverse solutions with optimal resolution kernels applied to electromagnetic tomography. *Human brain mapping*, 5(6):454–467, 1997.

de Peralta Menendez R G, Andino S L G, and Lütkenhöner B. Figures of merit to compare distributed linear inverse solutions. *Brain Topography*, 9(2):117–124, 1996.

Demuru M, La Cava S M, Pani S M, and Fraschini M. A comparison between power spectral density and network metrics: an EEG study. *Biomedical Signal Processing and Control*, 57:101760, 2020.

Donoghue T, Haller M, Peterson E J, Varma P, Sebastian P, Gao R, Noto T, Lara A H, Wallis J D, Knight R T, et al. Parameterizing neural power spectra into

periodic and aperiodic components. *Nature neuroscience*, 23(12):1655–1665, 2020.

Duan F, Huang Z, Sun Z, Zhang Y, Zhao Q, Cichocki A, Yang Z, and Solé-Casals J. Topological network analysis of early Alzheimer's disease based on resting-state EEG. *IEEE Transactions on Neural Systems and Rehabilitation Engineering*, 28 (10):2164–2172, 2020.

Ebner A, Sciarretta G, Epstein C M, and Nuwer M. Eeg instrumentation. the international federation of clinical neurophysiology. *Electroencephalography and clinical neurophysiology. Supplement*, 52:7–10, 1999.

Engl H W, Hanke M, and Neubauer A. *Regularization of inverse problems*, volume 375. Springer Science & Business Media, 1996.

Foster J J, Sutterer D W, Serences J T, Vogel E K, and Awh E. Alpha-band oscillations enable spatially and temporally resolved tracking of covert spatial attention. *Psychological science*, 28(7):929–941, 2017.

Fountas Z et al. Spiking neural networks for human-like avatar control in a simulated environment. *Computing Science of Imperial College London*, 2011.

Fries P. A mechanism for cognitive dynamics: neuronal communication through neuronal coherence. *Trends in cognitive sciences*, 9(10):474–480, 2005.

Fries P. Rhythms for cognition: communication through coherence. *Neuron*, 88 (1):220–235, 2015.

Fukushima M, Yamashita O, Knösche T R, and Sato M. MEG source reconstruction based on identification of directed source interactions on whole-brain anatomical networks. *NeuroImage*, 105:408–427, 2015.

Galluzzi S, Marizzoni M, Babiloni C, Albani D, Antelmi L, Bagnoli C, Bartres-Faz D, Cordone S, Didic M, Farotti L, et al. Clinical and biomarker profiling of prodromal alzheimer's disease in workpackage 5 of the innovative medicines initiative pharmacog project: a 'european adni study'. *Journal of internal medicine*, 279(6):576–591, 2016.

Garcés P, López-Sanz D, Maestú F, and Pereda E. Choice of magnetometers and gradiometers after signal space separation. *Sensors*, 17(12):2926, 2017.

Gerstoft P, Xenaki A, and Mecklenbräuker C F. Multiple and single snapshot compressive beamforming. *The Journal of the Acoustical Society of America*, 138 (4):2003–2014, 2015.

Gómez-Ramírez J, Freedman S, Mateos D, Velázquez J L P, and Valiante T A. Exploring the alpha desynchronization hypothesis in resting state networks with intracranial electroencephalography and wiring cost estimates. *Scientific reports*, 7(1):1–11, 2017.

Gorgolewski K, Esteban O, Schaefer G, Wandell B, and Poldrack R. Openneuro—a free online platform for sharing and analysis of neuroimaging data. *Organization for human brain mapping. Vancouver, Canada*, 1677(2), 2017.

Gramfort A, Kowalski M, and Hämäläinen M. Mixed-norm estimates for the m/eeg inverse problem using accelerated gradient methods. *Physics in Medicine & Biology*, 57(7):1937–61, 2012.

Gramfort A, Luessi M, Larson E, Engemann D A, Strohmeier D, Brodbeck C, Goj R, Jas M, Brooks T, Parkkonen L, et al. MEG and EEG data analysis with MNE-Python. *Frontiers in neuroscience*, 7:267, 2013.

Gramfort A, Luessi M, Larson E, Engemann D A, Strohmeier D, Brodbeck C, Parkkonen L, and Hämäläinen M S. MNE software for processing MEG and EEG data. *Neuroimage*, 86:446–460, 2014.

Hadamard J. Sur les problèmes aux dérivées partielles et leur signification physique. *Princeton university bulletin*, pages 49–52, 1902.

Haegens S, Cousijn H, Wallis G, Harrison P J, and Nobre A C. Inter- and intra-individual variability in alpha peak frequency. *Neuroimage*, 92:46–55, 2014.

Hämäläinen M, Hari R, Ilmoniemi R J, Knuutila J, and Lounasmaa O V. Magnetoencephalography—theory, instrumentation, and applications to noninvasive studies of the working human brain. *Reviews of modern Physics*, 65(2):413, 1993.

Hämäläinen M S and Ilmoniemi R J. *Interpreting measured magnetic fields of the brain: estimates of current distributions*. Helsinki University of Technology, Department of Technical Physics, 1984.

Hämäläinen M S and Ilmoniemi R J. Interpreting magnetic fields of the brain: minimum norm estimates. *Medical & biological engineering & computing*, 32 (1):35–42, 1994a.

Hämäläinen M S and Ilmoniemi R J. Interpreting magnetic fields of the brain: minimum norm estimates. *Medical & biological engineering & computing*, 32 (1):35–42, 1994b.

Hanke M and Hansen P C. Regularization methods for large-scale problems. *Surv. Math. Ind*, 3(4):253–315, 1993.

Hansen P C. *Rank-deficient and discrete ill-posed problems: numerical aspects of linear inversion*. SIAM, 1998.

Hansen P C. *Rank-deficient and discrete ill-posed problems: numerical aspects of linear inversion*, volume 4. Siam, 2005.

Haufe S and Ewald A. A simulation framework for benchmarking eeg-based brain connectivity estimation methodologies. *Brain topography*, 32(4):625–642, 2019.

Haufe S, Nikulin V V, Müller K R, and Nolte G. A critical assessment of connectivity measures for eeg data: a simulation study. *Neuroimage*, 64:120–133, 2013.

Hauk O, Stenroos M, and Treder M. EEG/MEG source estimation and spatial filtering: The linear toolkit. *Magnetoencephalography: From Signals to Dynamic Cortical Networks*, pages 1–37, 2019.

He B, Astolfi L, Valdés-Sosa P A, Marinazzo D, Palva S O, Bénar C G, Michel C M, and Koenig T. Electrophysiological brain connectivity: theory and implementation. *IEEE Transactions on Biomedical Engineering*, 66(7):2115–2137, 2019.

Hill R M, Boto E, Holmes N, Hartley C, Seedat Z A, Leggett J, Roberts G, Shah V, Tierney T M, Woolrich M W, et al. A tool for functional brain imaging with lifespan compliance. *Nature communications*, 10(1):1–11, 2019.

Hincapié A S, Kujala J, Mattout J, Daligault S, Delpuech C, Mery D, Cosmelli D, and Jerbi K. MEG connectivity and power detections with minimum norm estimates require different regularization parameters. *Computational Intelligence and Neuroscience*, 2016:19, 2016.

Hincapié A S, Kujala J, Mattout J, Pascarella A, Daligault S, Delpuech C, Mery D, Cosmelli D, and Jerbi K. The impact of MEG source reconstruction method on source-space connectivity estimation: a comparison between minimum-norm solution and beamforming. *Neuroimage*, 156:29–42, 2017.

Horwitz B. The elusive concept of brain connectivity. *Neuroimage*, 19(2):466–470, 2003.

Huettel S A, Song A W, McCarthy G, et al. *Functional magnetic resonance imaging*, volume 1. Sinauer Associates Sunderland, MA, 2004.

Jas M, Engemann D A, Bekhti Y, Raimondo F, and Gramfort A. Autoreject: Automated artifact rejection for MEG and EEG data. *NeuroImage*, 159:417–429, 2017.

Jestrović I, Coyle J, and Sejdić E. The effects of increased fluid viscosity on stationary characteristics of eeg signal in healthy adults. *Brain research*, 1589: 45–53, 2014.

Jirsa V K and McIntosh A R. *Handbook of brain connectivity*, volume 1. Springer, 2007.

Jutten C and Herault J. Blind separation of sources, part i: An adaptive algorithm based on neuromimetic architecture. *Signal processing*, 24(1):1–10, 1991.

Jwo D J, Chang W Y, and Wu I H. Windowing techniques, the welch method for improvement of power spectrum estimation. *CMC-COMPUTERS MATERIALS & CONTINUA*, 2021.

Kiebel S J, Garrido M I, Moran R J, and Friston K J. Dynamic causal modelling for EEG and MEG. *Cognitive neurodynamics*, 2(2):121, 2008.

Klimesch W. Memory processes, brain oscillations and EEG synchronization. *International journal of psychophysiology*, 24(1-2):61–100, 1996.

Klimesch W. EEG alpha and theta oscillations reflect cognitive and memory performance: a review and analysis. *Brain research reviews*, 29(2-3):169–195, 1999.

Klimesch W, Doppelmayr M, Schimke H, and Ripper B. Theta synchronization and alpha desynchronization in a memory task. *Psychophysiology*, 34(2):169–176, 1997.

Klimesch W, Doppelmayr M, Russegger H, Pachinger T, and Schwaiger J. Induced alpha band power changes in the human EEG and attention. *Neuroscience letters*, 244(2):73–76, 1998.

König R, Sielużycki C, and Durka P J. Tiny signals from the human brain: Acquisition and processing of biomagnetic fields in magnetoencephalography. *Journal of Low Temperature Physics*, 146(5):697–718, 2007.

Lachaux J P, Rodriguez E, Martinerie J, and Varela F J. Measuring phase synchrony in brain signals. *Human brain mapping*, 8(4):194–208, 1999.

Lagarias J C, Reeds J A, Wright M H, and Wright P E. Convergence properties of the nelder–mead simplex method in low dimensions. *SIAM Journal on optimization*, 9(1):112–147, 1998.

Lai M, Demuru M, Hillebrand A, and Fraschini M. A comparison between scalp- and source-reconstructed EEG networks. *Scientific reports*, 8(1):1–8, 2018.

Lang E W, Tomé A M, Keck I R, Górriz-Sáez J, and Puntonet C G. Brain connectivity analysis: a short survey. *Computational intelligence and neuroscience*, 2012.

Lemaréchal C. Cauchy and the gradient method. *Doc Math Extra*, 251(254):10, 2012.

Lin F H, Belliveau J W, Dale A M, and Hämäläinen M S. Distributed current estimates using cortical orientation constraints. *Human brain mapping*, 27(1): 1–13, 2006.

Liuzzi L, Quinn A J, O'Neill G C, Woolrich M W, Brookes M J, Hillebrand A, and Tewarie P. How sensitive are conventional meg functional connectivity metrics with sliding windows to detect genuine fluctuations in dynamic functional connectivity? *Frontiers in neuroscience*, 13:797, 2019.

Lloyd S. Least squares quantization in PCM. *IEEE transactions on information theory*, 28(2):129–137, 1982.

Lütkepohl H. *New introduction to multiple time series analysis*. Springer Science & Business Media, 2005.

Mahjoory K, Nikulin V V, Botrel L, Linkenkaer-Hansen K, Fato M M, and Haufe S. Consistency of EEG source localization and connectivity estimates. *Neuroimage*, 152:590–601, 2017.

Mai J K, Majtanik M, and Paxinos G. *Atlas of the human brain*. Academic Press, 2015.

Malmivuo J, Plonsey R, et al. *Bioelectromagnetism: principles and applications of bioelectric and biomagnetic fields*. Oxford University Press, USA, 1995.

Mammone N, De Salvo S, Bonanno L, Ieracitano C, Marino S, Marra A, Bramanti A, and Morabito F C. Brain network analysis of compressive sensed high-density EEG signals in AD and MCI subjects. *IEEE Transactions on Industrial Informatics*, 15(1):527–536, 2018.

Matsuura K and Okabe Y. Selective minimum-norm solution of the biomagnetic inverse problem. *IEEE Transactions on Biomedical Engineering*, 42(6):608–615, 1995.

Morabito F C, Campolo M, Ieracitano C, Ebadi J M, Bonanno L, Bramanti A, Desalvo S, Mammone N, and Bramanti P. Deep convolutional neural networks for classification of mild cognitive impaired and Alzheimer's disease patients from scalp EEG recordings. In *2016 IEEE 2nd International Forum on Research and Technologies for Society and Industry Leveraging a better tomorrow (RTSI)*, pages 1–6. IEEE, 2016.

Moretti D V, Babiloni C, Binetti G, Cassetta E, Dal Forno G, Ferreric F, Ferri R, Lanuzza B, Miniussi C, Nobili F, et al. Individual analysis of EEG frequency and band power in mild Alzheimer's disease. *Clinical Neurophysiology*, 115(2): 299–308, 2004.

Moretti D V, Miniussi C, Frisoni G, Zanetti O, Binetti G, Geroldi C, Galluzzi S, and Rossini P. Vascular damage and EEG markers in subjects with mild cognitive impairment. *Clinical neurophysiology*, 118(8):1866–1876, 2007.

Musaeus C S, Engedal K, Høgh P, Jelic V, Mørup M, Naik M, Oeksengaard A R, Snaedal J, Wahlund L O, Waldemar G, et al. Oscillatory connectivity as a diagnostic marker of dementia due to Alzheimer's disease. *Clinical Neurophysiology*, 130(10):1889–1899, 2019.

Niedermeyer E and da Silva F L. *Electroencephalography: basic principles, clinical applications, and related fields*. Lippincott Williams & Wilkins, 2005.

Nolte G, Bai O, Wheaton L, Mari Z, Vorbach S, and Hallett M. Identifying true brain interaction from EEG data using the imaginary part of coherency. *Clinical neurophysiology*, 115(10):2292–2307, 2004.

Nolte G, Ziehe A, Nikulin V V, Schlögl A, Krämer N, Brismar T, and Müller K R. Robustly estimating the flow direction of information in complex physical systems. *Physical review letters*, 100(23):234101, 2008.

Nolte G, Galindo-Leon E, Li Z, Liu X, and Engel A K. Mathematical relations between measures of brain connectivity estimated from electrophysiological recordings for gaussian distributed data. *bioRxiv*, page 680678, 2019.

North G. Data analysis — time series analysis. In Holton J R, editor, *Encyclopedia of Atmospheric Sciences*, pages 621–624. Academic Press, Oxford, 2003. ISBN 978-0-12-227090-1. doi: https://doi.org/10.1016/B0-12-227090-8/00131-7. URL https://www.sciencedirect.com/science/article/pii/B0122270908001317.

Núñez P, Poza J, Gómez C, Rodríguez-González V, Hillebrand A, Tola-Arribas M A, Cano M, and Hornero R. Characterizing the fluctuations of dynamic resting-state electrophysiological functional connectivity: Reduced neu-

ronal coupling variability in mild cognitive impairment and dementia due to Alzheimer's disease. *Journal of neural engineering*, 16(5):056030, 2019.

Nunez P L, Wingeier B M, and Silberstein R B. Spatial-temporal structures of human alpha rhythms: Theory, microcurrent sources, multiscale measurements, and global binding of local networks. *Human brain mapping*, 13(3):125–164, 2001.

Offner F F. The EEG as potential mapping: the value of the average monopolar reference. *Electroencephalography and clinical neurophysiology*, 2(2):213–214, 1950.

Ossadtchi A, Altukhov D, and Jerbi K. Phase shift invariant imaging of coherent sources (PSIICOS) from MEG data. *NeuroImage*, 183:950–971, 2018.

Palva J M, Wang S H, Palva S, Zhigalov A, Monto S, Brookes M J, Schoffelen J M, and Jerbi K. Ghost interactions in MEG/EEG source space: A note of caution on inter-areal coupling measures. *Neuroimage*, 173:632–643, 2018.

Pascarella A and Sorrentino A. *Statistical approaches to the inverse problem*. InTech, Rijeka, Croatia, 2011.

Pascual-Marqui R D, Lehmann D, Koenig T, Kochi K, Merlo M C, Hell D, and Koukkou M. Low resolution brain electromagnetic tomography (loreta) functional imaging in acute, neuroleptic-naive, first-episode, productive schizophrenia. *Psychiatry Research: Neuroimaging*, 90(3):169–179, 1999.

Pedregosa F, Varoquaux G, Gramfort A, Michel V, Thirion B, Grisel O, Blondel M, Prettenhofer P, Weiss R, Dubourg V, Vanderplas J, Passos A, Cournapeau D, Brucher M, Perrot M, and Duchesnay E. Scikit-learn: Machine learning in Python. *Journal of Machine Learning Research*, 12:2825–2830, 2011.

Pereda E, Quiroga R Q, and Bhattacharya J. Nonlinear multivariate analysis of neurophysiological signals. *Progress in neurobiology*, 77(1):1–37, 2005.

Polyak B T. Introduction to optimization. optimization software. *Inc., Publications Division, New York*, 1, 1987.

Saad J F, Kohn M R, Clarke S, Lagopoulos J, and Hermens D F. Is the theta/beta EEG marker for ADHD inherently flawed? *Journal of attention disorders*, 22 (9):815–826, 2018.

Sakkalis V. Review of advanced techniques for the estimation of brain connectivity measured with EEG/MEG. *Computers in biology and medicine*, 41(12):1110–1117, 2011.

Saxena A, Prasad M, Gupta A, Bharill N, Patel O P, Tiwari A, Er M J, Ding W, and Lin C T. A review of clustering techniques and developments. *Neurocomputing*, 267:664–681, 2017.

Schacter D L. EEG theta waves and psychological phenomena: A review and analysis. *Biological psychology*, 5(1):47–82, 1977.

Schoffelen J M and Gross J. Source connectivity analysis with meg and eeg. *Human brain mapping*, 30(6):1857–1865, 2009.

Schoffelen J M and Gross J. Studying dynamic neural interactions with MEG. *Magnetoencephalography: from signals to dynamic cortical networks*, pages 1–23, 2019a.

Schoffelen J M and Gross J. Studying dynamic neural interactions with meg. *Magnetoencephalography: from signals to dynamic cortical networks*, pages 519–541, 2019b.

Schott G D. Penfield's homunculus: a note on cerebral cartography. *Journal of neurology, neurosurgery, and psychiatry*, 56(4):329, 1993.

Schuster T, Kaltenbacher B, Hofmann B, and Kazimierski K S. *Regularization methods in Banach spaces*. de Gruyter, 2012.

Shen E H, Overly C C, and Jones A R. The allen human brain atlas: comprehensive gene expression mapping of the human brain. *Trends in neurosciences*, 35(12): 711–714, 2012.

Singh Y, Singh J, Sharma R, and Talwar A. FFT transformed quantitative EEG analysis of short term memory load. *Annals of neurosciences*, 22(3):176, 2015.

Sommariva S and Sorrentino A. Sequential monte carlo samplers for semi-linear inverse problems and application to magnetoencephalography. *Inverse Problems*, 30(11):114020, 2014.

Sommariva S, Sorrentino A, Piana M, Pizzella V, and Marzetti L. A comparative study of the robustness of frequency-domain connectivity measures to finite data length. *Brain topography*, 32(4):675–695, 2019.

Sporns O. Network attributes for segregation and integration in the human brain. *Current opinion in neurobiology*, 23(2):162–171, 2013.

Stam C. Use of magnetoencephalography (MEG) to study functional brain networks in neurodegenerative disorders. *Journal of the neurological sciences*, 289 (1-2):128–134, 2010.

Stam C J, Nolte G, and Daffertshofer A. Phase lag index: assessment of functional connectivity from multi channel eeg and meg with diminished bias from common sources. *Human brain mapping*, 28(11):1178–1193, 2007.

Stoica P, Moses R L, et al. Spectral analysis of signals. 2005.

Subramaniyam N P, Tronarp F, Särkkä S, and Parkkonen L. Expectation–maximization algorithm with a nonlinear Kalman smoother for MEG/EEG connectivity estimation. In *EMBEC & NBC 2017*, pages 763–766. Springer, 2017.

Thompson A M, Brown J C, Kay J W, and Titterington D M. A study of methods of choosing the smoothing parameter in image restoration by regularization. *IEEE Transactions on Pattern Analysis & Machine Intelligence*, (4):326–339, 1991.

Thomson D J. Spectrum estimation and harmonic analysis. *Proceedings of the IEEE*, 70(9):1055–1096, 1982.

Thomson D J. Jackknifing multitaper spectrum estimates. *IEEE Signal Processing Magazine*, 24(4):20–30, 2007.

Tikhonov A N, Goncharsky A, Stepanov V, and Yagola A G. *Numerical methods for the solution of ill-posed problems*, volume 328. Springer Science & Business Media, 2013.

Tikhonov A N. On the stability of inverse problems. In *Dokl. Akad. Nauk SSSR*, volume 39, pages 195–198, 1943.

Toga A W, Thompson P M, Mori S, Amunts K, and Zilles K. Towards multimodal atlases of the human brain. *Nature Reviews Neuroscience*, 7(12):952–966, 2006.

Tronarp F, Subramaniyam N P, Särkkä S, and Parkkonen L. Tracking of dynamic functional connectivity from MEG data with Kalman filtering. In *2018 40th Annual International Conference of the IEEE Engineering in Medicine and Biology Society (EMBC)*, pages 1003–1006. IEEE, 2018.

Uutela K, Hämäläinen M, and Somersalo E. Visualization of magnetoencephalographic data using minimum current estimates. *NeuroImage*, 10(2):173–180, 1999.

Vallarino E, Sommariva S, Piana M, and Sorrentino A. On the two-step estimation of the cross-power spectrum for dynamical linear inverse problems. *Inverse Problems*, 36(4):045010, 2020.

Vallarino E, Sommariva S, Arnaldi D, Famà F, Piana M, and Nobili F. Transfreq: a Python package for computing the theta-to-alpha transition frequency from resting state EEG data. *bioRxiv*, 2021a.

Vallarino E, Sorrentino A, Piana M, and Sommariva S. The role of spectral complexity in connectivity estimation. *Axioms*, 10(1):35, 2021b.

Van de Steen F, Faes L, Karahan E, Songsiri J, Valdes-Sosa P A, and Marinazzo D. Critical comments on eeg sensor space dynamical connectivity analysis. *Brain topography*, 32(4):643–654, 2019.

Van Veen B D and Buckley K M. Beamforming: A versatile approach to spatial filtering. *IEEE assp magazine*, 5(2):4–24, 1988.

Vinck M, van Wingerden M, Womelsdorf T, Fries P, and Pennartz C M. The pairwise phase consistency: a bias-free measure of rhythmic neuronal synchronization. *Neuroimage*, 51(1):112–122, 2010.

Virtanen P, Gommers R, Oliphant T E, Haberland M, Reddy T, Cournapeau D, Burovski E, Peterson P, Weckesser W, Bright J, et al. SciPy 1.0: fundamental algorithms for scientific computing in Python. *Nature methods*, 17(3):261–272, 2020.

Vogel C R. *Computational methods for inverse problems*. SIAM, 2002.

Wang S H, Lobier M, Siebenhühner F, Puoliväli T, Palva S, and Palva J M. Hyperedge bundling: A practical solution to spurious interactions in MEG/EEG source connectivity analyses. *NeuroImage*, 173:610–622, 2018.

Welch P. The use of fast fourier transform for the estimation of power spectra: a method based on time averaging over short, modified periodograms. *IEEE Transactions on audio and electroacoustics*, 15(2):70–73, 1967.

Wendling F, Bartolomei F, Bellanger J, and Chauvel P. Epileptic fast activity can be explained by a model of impaired gabaergic dendritic inhibition. *European Journal of Neuroscience*, 15(9):1499–1508, 2002.